AD NUMBER
AD893201
LIMITATION CHANGES

TO:

Approved for public release; distribution is unlimited.

FROM:

Distribution authorized to U.S. Gov't. agencies only; Test and Evaluation; 10 APR 1972. Other requests shall be referred to Air Force Avionics Laboratory, Attn: DOT, Wright-Patterson AFB, OH 45433.

AUTHORITY

AFAL ltr, 11 Apr 1974

AFAL-TR-71-346

STUDIES IN OPTICS

Brian J. Thompson, Principal Investigator
716-275-2314

and members of

The Institute of Optics
The University of Rochester

TECHNICAL REPORT AFAL-TR-71-346

March 1972

Avionics Laboratory. ~~of the Air Force~~

Sponsored By
Advanced Research Project Agency

ARPA Order No. 745
Program Code No. SCD B
Contract No. F33615-70-C-1451
Amount of Contract $142,106
Inclusive Dates of Contract 13 February 1970 - 14 December 1971

Air Force Avionics Laboratory
Air Force Systems Command
Wright-Patterson Air Force Base, Ohio

attn: DOT

NOTICE

When Government drawings, specifications, or other
data are used for any purpose other than in connection
with a definitely related Government procurement operation,
the United States Government thereby incurs no responsi-
bility nor any obligation whatsoever; and the fact that
the government may have formulated, furnished, or in any
way supplied the said drawings, specifications, or other
data, is not to be regarded by implication or otherwise
as in any manner licensing the holder or any other person
or corporation, or conveying any rights or permission to
manufacture, use, or sell any patented invention that may
in any way be related thereto.

Copies of this report should not be returned unless
return is required by security considerations, contractual
obligations, or notice on a specific document.

AFAL-TR-71-346

STUDIES IN OPTICS

Brian J. Thompson
Michael Hercher
James M. Forsyth
David B. Dutton
Douglas C. Sinclair
et al.

TECHNICAL REPORT AFAL-TR-71-346
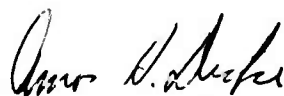
MARCH 1972

attn: DOT

FOREWORD

This study was conducted by members of The Institute
of Optics, The University of Rochester, Rochester, New
York 14627, under the sponsorship of the Advanced Research
Projects Agency, Project No. 745, Contract F 33615-70-C-1451.
The Air Force program monitor was Capt. Robert B. Bell
of the Electro-Optics Device Branch, Electronic Technology
Division, Air Force Avionics Laboratory, Air Force Systems
Command, Wright-Patterson Air Force Base, Ohio 45433.

Portions of the study were performed by Institute of
Optics graduate students Anthony J. Devaney, Leonard
Gruber, Peter Nebolsine, and Chand Roychoudhuri. Their
names appear on the appropriate sections of this report.

Inclusive dates of this portion of the project are
13 February 1970 to 14 December 1971. The report was
approved as of 19 January, 1972.

This technical report has been reviewed and is ap-
proved for publication.

AMOS H. DICKE
Chief, Electro-Optics Device Branch
Electronic Technology Division

ii

ABSTRACT

The "Studies in Optics" described are directed
towards the assessment and improvement of laser output
characteristics and to problems in the use of the coherent
output of a laser in optical systems. The various aspects
of this work are clearly interrelated but for clarity are
grouped into four parts. Section II consists of a study
of techniques for assessing and improving laser beam pro-
pagation characteristics including apodization of coherent
imaging systems and holographic methods of measuring the
amplitude and phase of pulsed laser beams. The design of
efficient solid state lasers is addressed in Section III
with particular reference to methods of enlarging the
TEM_{oo} mode size and the correction of thermally induced
optical distortion in repetitively pumped ruby laser rods.
Section IV is a study of laser beam steering techniques
leading to devices in the multi MHz range using a new
large bore argon-ion laser design with intra-cavity
modulation. The final portion (Section V) is concerned
with procedures for overall lens evaluation using optical
transfer function data exemplified by the specific data
on a 3 inch f/4.5 wide angle lens.

TABLE OF CONTENTS

v

CONTENTS (Continued)

CONTENTS (Continued)

CONTENTS (Continued)

LIST OF ILLUSTRATIONS

SECTION I

INTRODUCTION

This report consists of four parts which represent separate but interrelated research efforts, each under the direction of a separate principal investigator.

The broad area that defines the research is the study and the assessment, improvement, and use of the output characteristics of lasers. Section II is concerned with a study of techniques for assessing and improving laser beam propagation. The most significant results of this part relate to the apodization of coherent systems to control the deleterious effects usually associated with coherent image formation. These studies, of course, assume a fully coherent beam. In pulsed laser systems the beam is often only partially coherent, but even when coherent the output wavefront contains significant amplitude and phase variations. To predict the performance of systems using this type of laser (as an illuminant, for example, in an imaging system) it is necessary to be able to measure the amplitude and phase of the laser output. Hence new holographic methods were developed to enable these measurements to be made.

1

Clearly associated with the problems mentioned above are those questions that relate to the design of efficient solid state laser systems with high energy power and low beam divergence. Section III reports on successful attempts to improve these parameters including techniques for enlarging the TEM_{oo} mode size and the correction of thermally induced optical distortion in repetitively pumped ruby laser rods.

One of the main ultimate uses of lasers is for a wide variety of illumination, imaging and recording devices. For these applications it is important to consider scanning the illuminating beam -- the importance of scanning in a recording device is clear. Hence, one aspect of the present study, reported in Section IV, was a new beam-steering technique that could lead to beam-steering devices in the multi-MHz range. This technique involves the locking of a set of transverse modes having a common longitudinal quantum number. In the successful initial study the experiments were carried out with a specially designed large aperture argon ion laser; electro-optic beam deflection is achieved by intracavity modulators.

Finally, the problem of a peripheral optical device cannot be ignored. Thus Section V is a report of a

2

continuing study of the optical transfer function, its measurement and application, which formed an integral part of the overall program. As an example of the procedure a map of the optical transfer function and the use of the evaluation program in a systematic study of a 3 inch f/4.5 wide-angle lens was completed.

SECTION II

STUDY OF TECHNIQUES FOR ASSESSING AND IMPROVING
LASER BEAM PROPAGATION CHARACTERISTICS

A. SOME DESIGN CONSIDERATIONS IN COHERENT SYSTEMS*

L. Gruber and B.J. Thompson

1. INTRODUCTION

With the emergence of the laser as an optical source,
and with the present demands on resolution and image quality,
the effects upon optical systems caused by the coherence
of the light can no longer be ignored. Although it is
realized that many optical systems are operating in a co-
herent mode, nothing is done to take this fact into account.
For example, it is known that both Critical and Kohler il-
lumination can, under certain circumstances, provide a high
degree of coherence in the object plane of a microscope.
Because of this, the resolution in the image is noticeably
reduced. Microdensitometer readings of bar targets have been
improperly interpreted with regards to the position of the
edges, simply because coherent object illumination had been
used. In optical data processing systems, coherent object
illumination is needed, yet the optical system is designed
without taking this fact into account; the result is very
poor image quality. Indeed, it is recognized that there
is a basic physical difference between   images formed
coherently and incoherently, but most optical systems are
designed as incoherent systems.

In image forming devices, it is usual to strive for
diffraction limited performance. This is laudible if the
system is to be used as an incoherent imaging system. If,
however, the system is to be used with coherent object il-
lumination, then other considerations become important.
Several studies have been made of coherent and partially

---

* This chapter gives in part the work of graduate student
  Leonard Gruber and is contained in his Master's thesis.

coherent image formation of a variety of objects showing edge ringing effects and mensuration problems associated with the nonlinearity of the image formation [1,2]. Many difficulties, such as errors in the measured separation of two relativly well resolved points[3], arise directly from this diffraction limited condition.

Rather than seeking specific apodization functions, a method of coherent apodization will be explored here so that some of the deleterious coherence effects previously mentioned may be either eliminated or reduced. The possibility of achieving this and an understanding of the origin of these effects should be of interest to the optical designer.

a. Concepts of Partially Coherent Light

To properly discuss the process of image formation in optical systems, it becomes necessary to use the theory of partial coherence. However, rather than engaging in a lengthy discussion of this theory, only those terms and concepts which are necessary for understanding the work to follow will be introduced here.

The basic function in the theory of partial coherence is the mutual coherence function $\Gamma_{12}(\tau)$, defined by

$$\Gamma_{12}(\tau) = \Gamma(\overline{x}_1, \overline{x}_2, \tau) = \langle V(\overline{x}_1, t) V(\overline{x}_2, t+\tau)\rangle, \qquad (1)^*$$

where $V(\overline{X}, t)$, is the analytic signal associated with a cartesian component of the electric field vector, τ is a time delay. Note that $\Gamma_{12}(\tau)$, is in general a function of seven variables————six space and one time delay

---

* The brackets indicate time average, i.e.,

$$\langle f^*(\overline{x}_1, t) f(\overline{x}_2, t+\tau)\rangle_{ave} = \lim_{\tau \to \infty} 1/T \int_o^T f^*(\overline{x}_1, t) f(\overline{x}_2, t+\tau) dt$$

6

variable. The normalized form of the mutual coherence function is called the complex degree of coherence $\gamma_{12}(\tau)$ where,

$$\gamma_{12}(\tau) = \Gamma_{12}(\tau) \qquad \Gamma_{11}(0)\Gamma_{22}(0). \tag{2}$$

$\Gamma_{12}(\tau)$ is a measurable quantity. If $\Gamma_{12}(\tau)$, is known in any one plane, its functional dependence can be determined in any other plane. It can be shown that the mutual coherence function obeys two wave equations,

$$\nabla_s^2 {}_{12}(\tau) = 1/c^2 \cdot \frac{\partial^2 \gamma_{12}(\tau)}{\partial \tau^2} \qquad\qquad s = 1,2. \tag{3}$$

where ∇_s^2 is the Laplacian operator in the coordinates of $\bar{x}_s$, and c is the velocity of light.

In most optical systems, it is the mutual intensity function, $\Gamma(\bar{x}_1, \bar{x}_2, 0)$, which is of importance. When all path differences (ΔL), in an experiment satisfy

$$|\Delta L/C = |\tau| \ll 1/\Delta\nu, \tag{4}$$

$\Delta\nu$ being the spectral width, the mutual coherence function can be written as

$$\Gamma(\bar{x}_1, \bar{x}_2, \tau) \cong \Gamma(\bar{x}_1, \bar{x}_2, 0) \exp(-2\pi i \bar{\nu}\tau), \tag{5}$$

If equation 5 is substituted into the wave equation (eq. 3), it follows that the mutual intensity function satisfies the Helmholtz equations

$$\nabla_s^2 \Gamma_{12}(0) + k^2 \Gamma_{12}(0) = 0, \qquad\qquad s = 1,2. \tag{6}$$

where $\Gamma_{12}(0)$ is an abbreviation for $\Gamma(x_1, x_2, 0)$.

b. The Impulse Response of an Optical System

The impulse response of an optical system is defined as the response of the system to a point object input.

From diffraction theory, a relation can be obtained between the object optical field $V_{ob}(\bar{\xi},t)$, and $V_{im}(\bar{x},t)$, the image optical field(refer to figure 1 for the geometry.),

$$V_{im}(\bar{x},t)= \int_{-\infty}^{\infty} V_{ob}(\bar{\xi},t)K(\bar{x}-\bar{\xi})d\bar{\xi}. \qquad (7)$$

$K(\bar{x}-\bar{\xi})$ is called the amplitude impulse response. In writing equation 7 as shown above, we have assumed a stationary optical field. That is, $K(\bar{x}-\bar{\xi})$ does not change in functional form as the object optical field is explored. In practice, imaging systems are seldom stationary over the entire object field, but it is usually possible to divide the object field into small "isoplanatic regions", within which the optical system is approximately stationary.

In an optical system, the aperture plane α^{*} and the image plane $\bar{x}$ are a fourier transform pair, i.e.,

$$K(\bar{x})=\int_{-\infty}^{\infty} A(\bar{\alpha})\exp(-ik\bar{\alpha}\bar{x}/Z_{2})d\bar{\alpha}, \qquad (8)$$

---

* The assumption is made that we are dealing only with thin lenses. This assumption gives us the convenience of having all the pupil planes and aperture planes coincide with the thin lens plane.
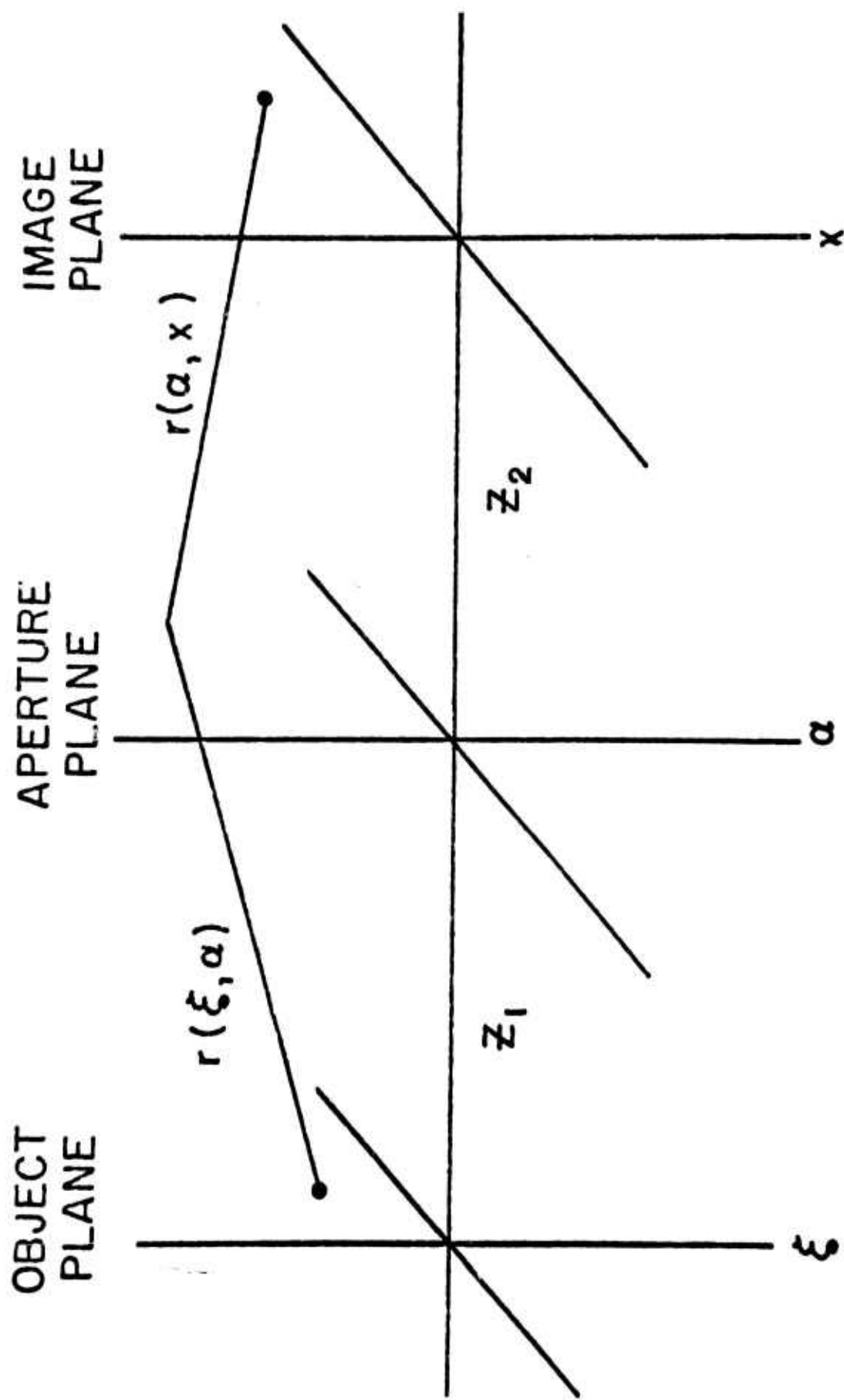
Figure 1. Propagation of the mutual intensity function through a lens.

9

where $k=2\pi/\lambda$,

$$A(\bar{\alpha}) = \int_{-\infty}^{\infty} K(\bar{x}) \exp(ik\bar{\alpha}\bar{x}/z_2)d\bar{x}. \tag{9}$$

$A(\alpha)$ is the aperture function or the exit pupil distribution. It follows from equation 7 that a basic observable quantity, the intensity in the image plane, can be obtained,

$$I_{im}(\bar{x}) = \langle V_{im}(\bar{x},t)V_{im}^{*}(\bar{x},t+\tau)\rangle, \tag{10}$$

which upon substitution of equation 7 into the above becomes

$$I_{im}(\bar{X}) = \int\int_{-\infty}^{\infty} \langle V_{ob}(\bar{\xi},t)V_{ob}^{*}(\bar{\xi},t)\rangle K(\bar{x}-\bar{\xi})K^{*}(\bar{x}-\bar{\xi}')d\bar{\xi}d\bar{\xi}' \tag{11}$$

Equation 11 is quite general and the bracketed term is just the mutual intensity function in the object plane. From equation 11 it is observed that the process of image formation is a function of two basic quantities: the amplitude impulse response $K(\bar{x}-\bar{\xi})$, and the mutual intensity function. If the object illumination is assumed

---

* Since $V_{im}(\bar{x},t)$ is independent of the frequency ν, it should be understood that quasi- monocromatic radiation is being used.

** The assumption is made that the amplitude impulse response is not a function of time.

to be statistically independent of light from another point[*]. The mutual intensity function can be written as,

$$\Gamma_{12}(\overline{\xi}) = I_{ob}(\overline{\xi})\delta(\overline{\xi}-\overline{\xi}') .$$ (12)

And the intensity in the image plane is (from equation 11)

$$I_{im}(\overline{x}) = \int_{-\infty}^{\infty} I_{ob}(\overline{\xi})S(\overline{x}-\overline{\xi})d\overline{\xi} ,$$ (13)

where we define $S(\overline{x}-\overline{\xi})$ as the intensity impulse response,

$$S(\overline{x}-\overline{\xi}) = K(\overline{x}-\overline{\xi})K^{*}(\overline{x}-\overline{\xi}) .$$ (14)

If however, the object illumination is completely correlated, that is, coherent over the object plane, the mutual intensity function then factors as

$$\Gamma_{12}(\overline{\xi}) = U_{ob}(\xi_1)U_{ob}^{*}(\xi_2) ,$$ (15)

and equation 11 becomes,

$$I_{im}(\overline{x}) = \left| \int_{-\infty}^{\infty} U_{ob}(\overline{\xi})K(\overline{x}-\xi)d\xi \right|^{2} .$$ (16)

Both coherent and incoherent object illumination represent two limiting cases of image formation with partially coherent light. In general, image formation is a linear process with respect to the mutual intensity function. It is important to realize that an image can, as shown by equations 13 and 16, be formed under quite different physical processes. Furthermore, since a co-

_____

[*]To be precise, a true incoherent field is a physical impossiblity because of diffraction. However, consistent with the given experiment, an incoherent field can be defined.

[**] Henceforth, we will assume that the optical field is a function of position only, i.e., $V(\xi,t) \longrightarrow U(\xi)$.

herent process is linear in complex amplitude, and an
incoherent process is linear in intensity, we should not
expect   the resultant intensity images of the same
object, formed with coherent and incoherent illumination, to
be identical; indeed,they are not.

2. DESIGN CONSIDERATIONS

a. Coherent Apodization

When bar targets are photographed using coherent
illumination, three anomalies immediately become apparent:

    a.   Speckle

    b.   Edge ringing

and upon close measurement of the image size,

    c.   Mensuration problems and image shift

Equation 16 governs the image forming process when
coherent object illumination is used. Edge ringing and
mensuration problems are caused by the fact that the
image intensity $I_{im}(\overline{x})$, is produced by the square of the
convolution of the complex object distribution $U_{ob}(\overline{\xi})$,
with the amplitude impulse response $K(\overline{x}-\overline{\xi})$. This process
differs from the usual incoherent process in two important
respects :

    a.   The image forming process is nonlinear, and

    b.   The amplitude impulse response, unlike the in-
tensity impulse response, can be negative or complex.
Not much can be done to remove the nonlinearity of the
imaging process, except for using low contrast objects[4].
However, the form of the amplitude impulse response can
be altered by changing the distribution of light across
the aperture plane. Apodization is concerned with the
possibility of determining the amplitude distribution
in the aperture plane in order to achieve some prespecified

distribution in the image plane. Classically, people have studied the theory of apodization but for reasons other than reducing coherence effects in optical systems. Many of the properties and theorems developed by these earlier workers are particularly important in this investigation.

A good summary of the work already carried out in studying apodization problems can be found in Wolf's review article on the diffraction theory of aberrations[5]. Most of the previous work has been directed towards apodizing an incoherent system, thereby changing the intensity impulse response. The usual procedure is to expand the intensity distribution over the aperture plane in a convenient set of functions: Hermite, Legendre, etc. Luneberg[6] tackled the apodization problem on a purely formal basis. He demanded that the Fraunhofer diffraction pattern satisfy certain constraints, and by the use of Lagrange multipliers derived integral equations which the aperture function must satisfy. Using a similar technique, Osterberg[7,8] has coated objectives with absorbing films in such a manner as to reduce the width of the central peak of the Airy pattern and thereby increase the resolution for the system. Barakat[9] and Jacquinot and Roizen-Dossier[10] have written review articles on the general apodization problems, and they have to some extent considered apodizing coherent systems. We should consider here the problem of coherent apodization.

The function $A(\bar{\alpha})$ is the amplitude distribution over the aperture plane. For physical realizable systems, $|A(\bar{\alpha})| = 1$, since the optical system is passive. In any real optical system the aperture is fixed and is of finite extent. Therefore, it is in general impossible to find a pupil function corresponding to a diffraction pattern (or impulse response) chosen arbitrarily. This is an obvious consequence of the fact that the amplitude im-

13

pulse response $K(\bar{x})$, and the aperture function $A(\bar{\alpha})$, are Fourier transform pairs.

It should be noted that the Fourier transform relation places severe limitations upon the possible solutions available to remove the coherence effects mentioned earlier. There are two methods available for finding an $A(\bar{\alpha})$ such that these coherence effects are either eliminated or minimized. First we can try an empirical approach. That is, we can arbitrarily place over the clear aperture various functions and then examine the resulting amplitude impulse response for each of the functions. This approach has been tried, and Jacquinot and Roizen-Dossier[10] have summarized the results. We can also try a formal or more systematic approach, as described earlier in this section. However, this latter method has no advantages, in this case, over the empirical approach, as will be shown later. Further, the main objective here is not to make an exhaustive study of apodization functions, but rather to investigate the merits of using coherent apodization as a technique in reducing coherence effects. Once this has been established, it will naturally be important to find the optimum apodization function which minimizes the coherence effects.

b. A Possible Solution

With the constraints imposed upon $K(\bar{x})$ and $A(\bar{\alpha})$ from the previous section, it remains to find a suitable apodization of the pupil, such that the coherence effects mentioned are no longer present or at least are minimized. Mensuration problems, edge ringing, and image shift are believed to be caused by the fact that the amplitude impulse response can be negative. This means that certain portions of the image field can subtract from other portions. The incoherent process involves a convolution of the intensity impulse response $S(\bar{x})$ which is always positive, thus no

subtraction is possible. It would therefore seem desirable to design a system so that the amplitude impulse response is always positive and real. This is at least one property that should be demanded of $K(\overline{x})$.

A suitable amplitude impulse response that satisfies the real and positive condition, is a gaussian distribution. Furthermore, since a gaussian transforms into a gaussian, a gaussian apodization of the pupil is dictated. However, the exit pupil will always be of finite extent, and hence the gaussian distribution will be truncated. Because of this truncation, the amplitude impulse response will unfortunately have oscillatory behavior. The degree of oscillation will depend upon the extent of truncation. It is important to determine the effect on the amplitude impulse response of this truncation by the pupil. Truncated aperture distributions have been investigated in beam divergence problems in laser propagation. Far field calculations have been made by Kauffman[11], Buck[12], and Bloom[13], and the near field has been studied by Campbell and Deshazer[14]. However, our interests and requirements are different from those of these workers. The effect of the gaussian apodization and truncation upon the image of coherently illuminated objects will be examined in the next section. It will be interesting to see how well the coherence effects are affected by the proposed apodization.

3. EXAMPLES OF IMAGING SHOWING THE EFFECTS OF COHERENT APODIZATION

a. Image of a Two Point Object

Lord Rayleigh, in 1902, was the first to consider the question of two point resolution. His criterion of

stating that the two points are just resolvable when
the maximum of one intensity pattern falls on the first
minima of the intensity pattern of the second point, is
not a basic resolution law. Rayleigh's resolution criterion
is also based on the tacit assumption that the two point
sources are incoherent with respect to each other. A more
definite resolution criterion has been given by Sparrow[15]
and it is used extensively when partially coherent illu-
mination is used.* The Sparrow criterion states that the
two point sources are just resolvable if the second de-
rivative of the resultant image intensity vanishes mid-
way between the respective geometrical image points**.
Barakat[16] has investigated the problem of two point
imaging for both coherent and incoherent illumination.
His results discuss the application of the Sparrow cri-
terion to apodized systems. However, our interest in
apodizing the system is not to increase resolution, but
to remove coherence effects. Also, rather than con-
sidering the two extreme limits for imaging, the theory
of partial coherence can be used to develop a more general
approach. The formulation followed here has been developed
by Grimes and Thompson[3] for non-apodized systems.

The intensity in the image plane is found by pro-
pagating the mutual intensity function in the object space,
to the image space, through the optical system. By rewriting
equation 11 in more general terms, the mutual intensity

---

* The Sparrow criterion was originally defined for incoherent
imaging, but it can easily be applied to the case where
partially coherent illumination is used.

** By geometrical image separation we mean that if b is
the two point separation in object space, the separation of
the intensity maxima in the image is b', where b'=mb, m being
the geometrical lateral magnification of the optical system.

function in the image plane is

$$\Gamma_{im}(\bar{x}_1, \bar{x}_2) = \iint_{ob} \Gamma_{ob}(\bar{\xi}_1, \bar{\xi}_2)\ K(\frac{\bar{x}_1}{q} + \frac{\bar{\xi}_1}{p})\ K*(\frac{\bar{x}_2}{q} + \frac{\bar{\xi}_2}{p}) d\bar{\xi}_1 d\bar{\xi}_2 \qquad (17)$$

where $\bar{x}_s$ is an image coordinate, $\bar{\xi}$ is an object coordinate and p and q are object and image distances respectively from the thin lens plane (see figure 2). To obtain the image intensity, set $\bar{x}_1 = \bar{x}_2 = \bar{x}$, then equation 17 becomes

$$I_{im}(\bar{x}) = \iint_{ob} \Gamma_{ob}(\bar{\xi}_1, \bar{\xi}_2)\ K(\frac{x_1}{q} + \frac{\xi_2}{p}) d\bar{\xi}_1 d\bar{\xi}_2 \qquad (18)$$

The mutual intensity function in the object space is given by

$$\Gamma_{ob}(\bar{\xi}_1, \bar{\xi}_2) = \Gamma_{ob}(\bar{\xi}_1, \bar{\xi}_2) t(\bar{\xi}_1) t(\bar{\xi}_2), \qquad (19)$$

where $t(\bar{\xi}_s)$ is the amplitude transmittance of the object. For two equally bright points, separated by a distance 2b, $t(\bar{\xi}_s)$ is given by

$$t(\bar{\xi}_s) = \delta(\xi_s - b) + \delta(\xi_s + b). \qquad s = 1, 2 \qquad (20)$$

$\Gamma'_{ob}(\xi_1, \xi_2)$ is the mutual intensity function just before the object plane, and can be written as

$$\Gamma'_{ob}(\xi_1, \xi_2) = I_o \gamma(\xi_1, \xi_2), \qquad (21)$$

where I_o is the normalized intensity and $\gamma(\xi_1, \xi_2)$ is the complex degree of coherence between the two points in the object plane. Substituting the right hand side of the equations 20 and 21 into equation 19, the mutual intensity

17
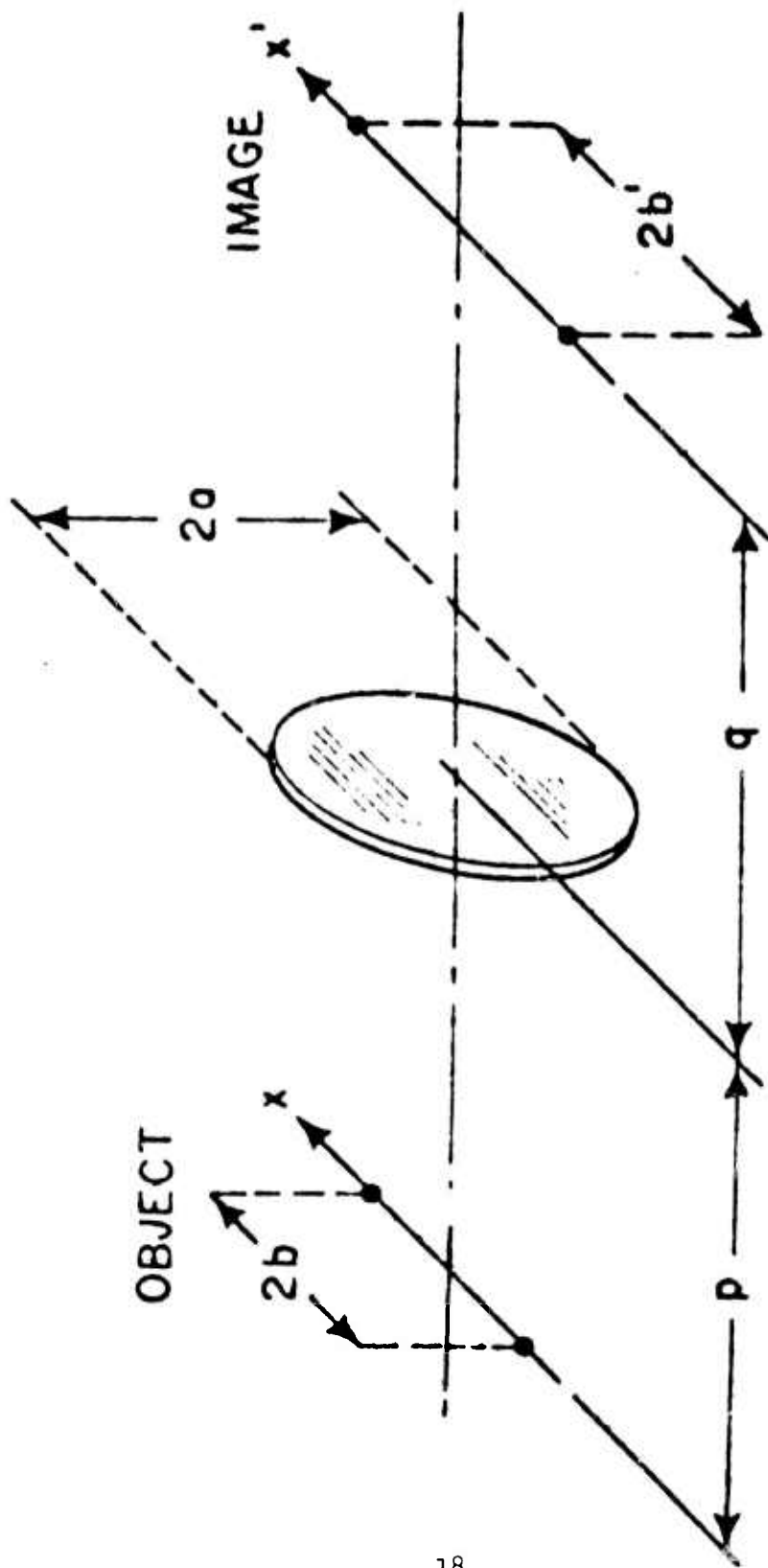
Figure 2. Two point image formation.

function just after the object plane is

$$\Gamma_{ob}(\bar{\xi}_1, \bar{\xi}_2) = I_o \, \gamma(\bar{\xi}_1, \bar{\xi}_2) \left[\delta(\bar{\xi}_1 - b)\delta(\bar{\xi}_2 - b) + \delta(\bar{\xi}_1 + b)\delta(\bar{\xi}_2 + b) + \right.$$
$$\left. \delta(\bar{\xi}_1 + b)\delta(\bar{\xi}_2 - b) + \delta(\bar{\xi}_1 - b)\delta(\bar{\xi}_2 + b) \right] \qquad (22)$$

Substituting the above equation into equation 18, we obtain for the intensity in the image plane

$$I_{im}(\bar{x}) = I_o \left[|K(\bar{x} - b')|^2 + |K(x + b')|^2 + Re \left\{ 2\gamma(b \cdot b) K(x - b') K(x + b')^* \right. \right. \qquad (23)$$

Re denotes the real part. For a two dimensional, lossless, diffraction limited system, the amplitude impulse response is

$$K(\bar{x}) = 2a \left[\frac{2J_1(ka\,\bar{x}/q)}{ka\,\bar{x}/q} \right] \equiv 2a\Lambda(Ka\,\bar{x}/q), \qquad (24)$$

where J_1 is a Bessel function of order one, a is the half width of the clear aperture stop and $k = 2\pi/\lambda$. The square of equation 24 is the familiar Airy pattern. The dotted curve in figure 3 show the intensity distribution for equation 23 assuming that $\gamma(b, -b) = 1$ and $K(\bar{x})$ is given by equation 24. It is clear from the figure that the distance between the maxima of the intensity distributions does not correspond to the geometrical separation 2b'. (The vertical center line in figure 3 indicates where the geometrical separation should be.) The image shift shown in the figure is possible for all values of $\gamma(b, -b)$, even when $\gamma(b, -b) = 0$. However the image shift is more pronounced when $\gamma(b, -b) \neq 0$, since the cross term in equation 23 can then contribute to the resultant image intensity. Because the cross term can have negative values, certain portions of the image field can subtract

19
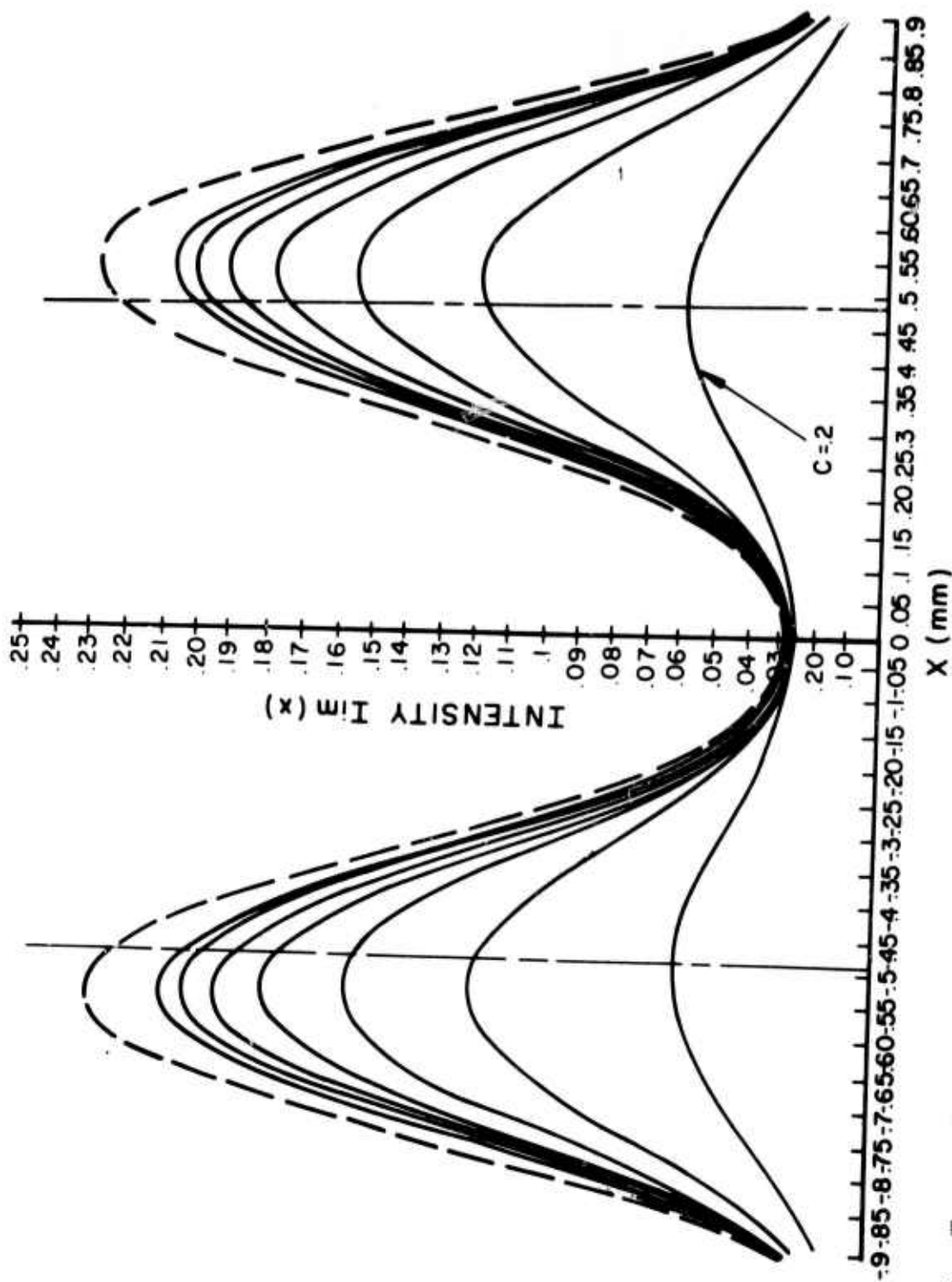
Figure 3. The resultant intensity distribution for a two dimensional coherent image of a two point object. δ = 6.4. The gaussian half width (c) is increased in steps of .1, from an initial value of c = .2. The dotted curve represents the unapodized case.

20

from others, thereby causing a greater degree of image shift. It can be seen from figure 3 that in the coherent case, the image shift can be as great as ten percent of the geometrical separation between the two points.

To remove this image shift when coherent illumination is used, a gaussian filter will be used to apodize the exit pupil of the system. For a two dimensional, circularly symmetric system, the amplitude impulse response is now given by,

$$K(x) = A \int_0^q \exp-(\alpha/C)^2 J_0(\alpha x k/q)\alpha d\alpha, \qquad (25)$$

where A is a constant and c is the half width of the gaussian filter[*]. Equation 23 was evaluated on a computer, using equation 25 as the amplitude impulse response. $\gamma(b,-b)$ was set equal to one, thus coherent illumination has been used. The results for one particular separation of the two points (2b=.298 mm), are shown in figure 3, for various values of c. These results indicate that the position of the intensity maxima is a function of the amount of apodization. If the value of c is .2 mm, the intensity maxima will coincide with the geometrical image separation (2b'=.892 mm). Since figure 3 is a plot of equation 23, it is not possible to see how the amplitude impulse response is affected by the apodization. Figure 4 is a plot of the amplitude impulse response itself. The dotted curve is the unapodized amplitude impulse response, which is, for a circularly symmetric exit pupil, $2a\Lambda(ka\bar{x}/q)$. The solid curve indicate how the amplitude impulse response is altered

---

[*] The half width of the gaussian filter is obtained by setting $\alpha=c$. At this point the amplitude of the gaussian has fallen to e^{-1}.
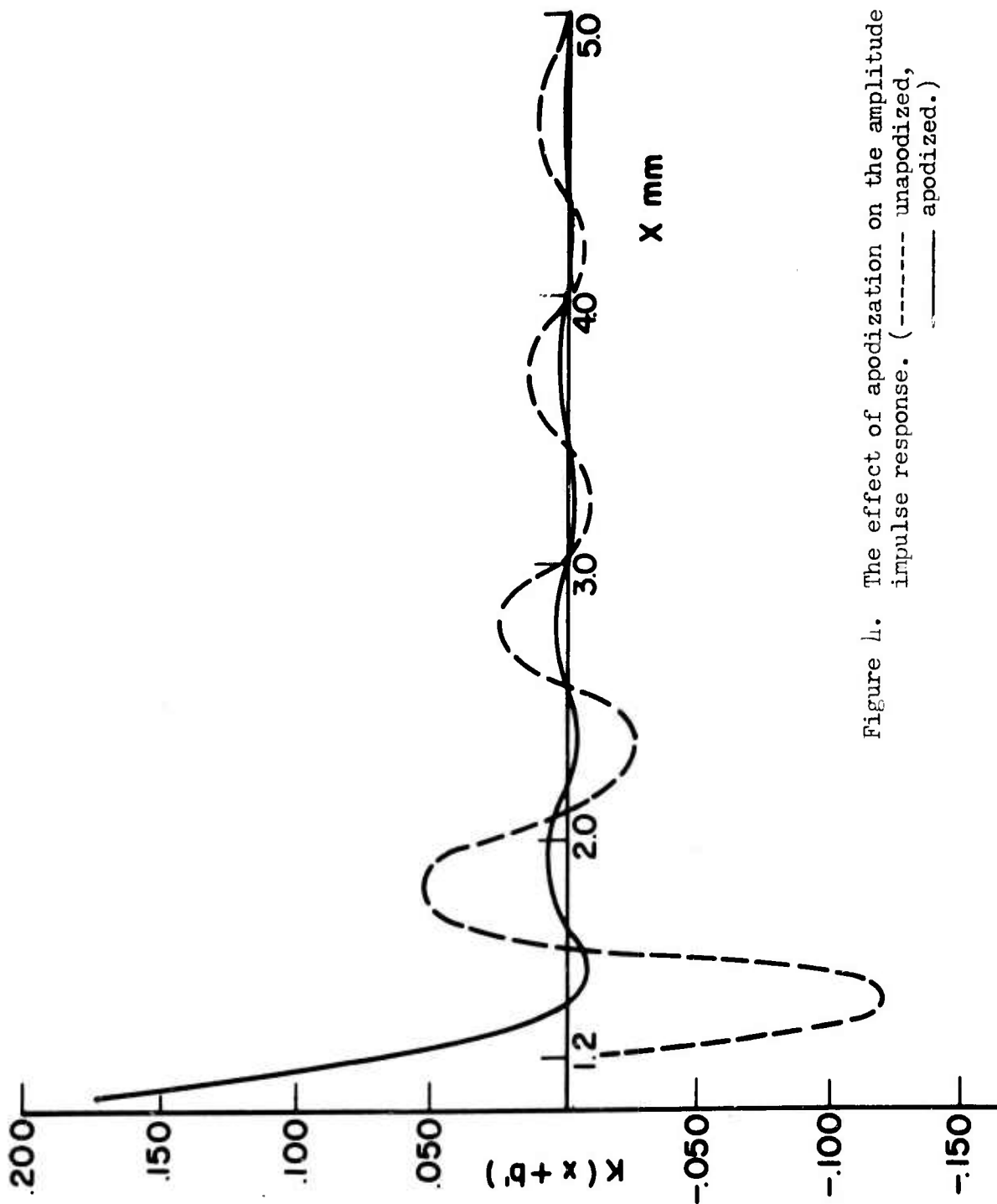
Figure 4. The effect of apodization on the amplitude impulse response. (------ unapodized, ———— apodized.)

22

by the apodization. It is clear that the outer ring structure of the amplitude impulse response is attenuated by the apodization filter. For the particular apodization shown, the half width c of the gaussian filter is .4 mm. In regions where $K(\overline{x}-b')$ or $K(\overline{x}+b')$ are negative, the cross term Re $2\gamma(b,-b)K(\overline{x}-b')K^*(\overline{x}+b')$ in equation 23 will subtract from the other two positive terms. The degree of subtraction is dependent upon the amplitude of the ring structure of $K(\overline{x})$. Therefore, by varying c, it is possible to control the amount of subtraction.

For a particular gaussian filter, it is instructive to examine the intensity in the image plane for a wide range of two point separations, or for varying degrees of truncation of the filter. Let us define a dimension- less quantity $\delta=2b'ka/q$. As δ varies from about four to a value of ten, the separation of the intensity maxima can be measured and compared to the corresponding geo- metrical separation 2b'. Figure 5 is a plot of R, the ratio of the measured separation to the geometrical separa- tion 2b', vs δ. The fact that R for the apodized case is always closer to one than in the unapodized case, strongly indicates that the gaussian apodization will always minimize image shifting for point source inputs, when coherent illumination is used.

It is quite possible that for certain values of δ, there occurs little or no image shifting. Under these circumstances, it would be important to see how the gaussian filter affects the resultant image intensity dis- tributions. For $\delta=10$, the image shift is almost negligi- ble. It is clear from figure 6 that in this case the gaussian filter has almost no effect upon the positions

23
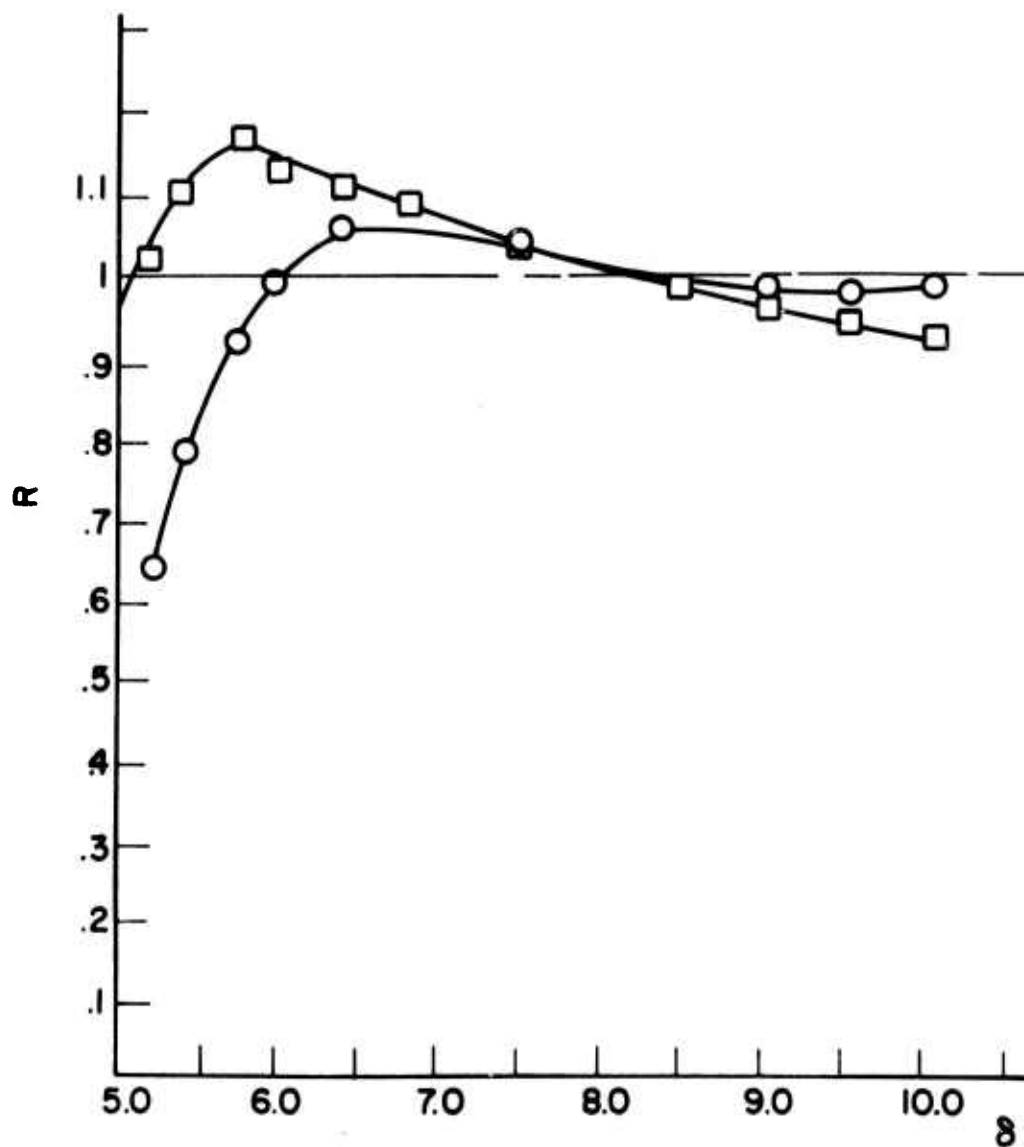
Figure 5. The ratio R of the measured to the gaussian
separation of the two images as a function of
δ (2 b'ka/q) for a gaussian filter of half
width .4 mm. Square symbols represent un-
apodized points and circles represent apodized
points.

24
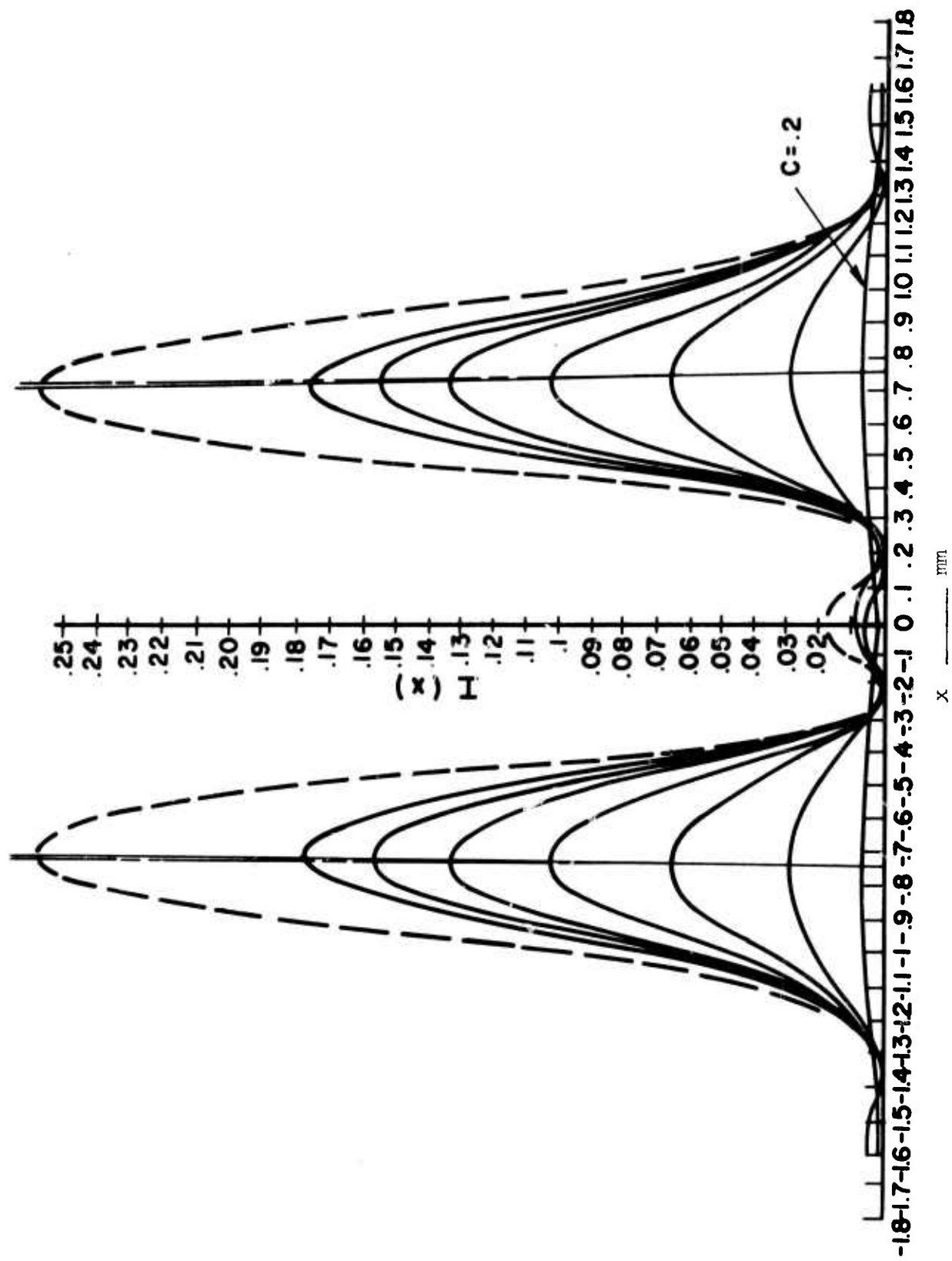
Figure 6. The resultant intensity distribution for a one dimensional, two point object distribution. $\delta(b,-b) = 1. \, \delta = 10.$ The gaussian half width (c) is increased in steps of .1, from an initial value of c = .2. The dotted curve represents the unapodized case.

25

of the intensity maxima. The major effect which the filter has is to reduce the overall intensity in the image plane as the half width of the filter is decreased. This property of the filter should be expected since the gaussian filter is absorbing in nature.

Finally, it should be re-emphasized here that the sole reason for apodizing the system is to remove the specific coherence effects mentioned earlier.

Although the gaussian filter has either eliminated or reduced the image shift, it should be noted that for a given γ, this has been accomplished at the expense of decreasing the systems resolution (see figures 3 and 6), and at a loss of illuminance in the image plane. Therefore, if an image of a coherent object distribution is near the resolution limit, the advantages of apodizing that system to remove the coherence effects will naturally be diminished.

b. Images of Slit and Bar Targets

The analysis of the preceding section, using delta function inputs, has essentially shown how the gaussian apodization affects the amplitude impulse response. It would now be appropriate to see how the apodized optical system images real object distributions. Because of their importance in optics, the images of edge and bar targets will now be considered. Edge objects are used extensively in instruments designed for determining the transfer functions of optical systems based on edge trace analysis. Standard bar targets are often used to establish resolution criteria for photographic systems.

The image of an edge with partially coherent ob-

ject illumination was first examined by H. H. Hopkins[17] in 1951. Other workers, notably Kinzly[1], Skinner[4], and Considine[18], have considered the effects of coherent object illumination on the image of an edge.

Bar targets exhibit the same coherence effects as edge objects. Therefore the discussion in this section will be limited to analyzing the images of slit and bar targets using coherent and incoherent object illumination.

Skinner[4] and Parrent and Thompson[19] have already investigated images of a slit for coherent and incoherent object illumination for a one dimensional, diffraction limited case. If a slit, of width 2b, is illuminated incoherently, an object intensity distribution is defined as

$$I_{ob}(\xi) = \begin{cases} I_o, & |\xi| \leq b \\ 0 & |\xi| > b \end{cases} \tag{26}$$

The image intensity for this object distribution is found by substituting equation 26 into equation 13 thus,

$$I_{im}(x) = \int_{-b}^{b} I_o \left| K\left(\frac{x}{q} + \frac{\xi}{p}\right) \right|^2 d\xi, \tag{27}$$

where q and p have already been defined (see figure 2). For a slit which is illuminated coherently, also of width 2b, the complex amplitude distribution is given (assuming no phase variation across the slit) by

$$U_{ob}(\xi) = \begin{cases} \sqrt{I_o}, & |\xi| \leq b \\ 0, & |\xi| > b, \end{cases} \tag{28}$$

and equation 16 becomes,

$$I_{im}(x) = \left| \int_{-b}^{b} \sqrt{I_o} \, K\left(\frac{x}{q} + \frac{\xi}{p}\right) d\xi \right|^2 \tag{29}$$

The amplitude impulse response, $K(\frac{x}{q} + \frac{\xi}{p})$, for a one dimensional, diffraction limited system can be written as a sinc* function. The integrals, equations 27 and 29, can be evaluated using standard integral formulas. The mathematics is summarized by Thompson[2] and will not be repeated here. If, however, the optical system is apodized, the amplitude impulse response can no longer be written in simple analytical form. The evaluation of the amplitude impulse response now involves calculating finite Fourier transforms. Equations 27 and 29 also involve two explicit integrations : one over ξ the object coordinate, and another over α, the pupil coordinate. To examine the images under the two different modes of object illumination, it becomes necessary to calculate the following types of integrals .

incoherent object illumination

$$I_{im}^{inc}(\overline{x}) = \int_{-\infty}^{\infty} I_{ob}(\xi) \left/ \int_{-\infty}^{\infty} A(\alpha)\exp(-ik\alpha\left\{\frac{x}{q} + \frac{\xi}{p}\right\})d\alpha \right|^2 d\xi . \tag{30}$$

coherent object illumination

$$I_{im}^{coh}(\overline{x}) = \left| \int\!\!\int_{-\infty}^{\infty} \sqrt{I_{ob}(\xi)}. \int_{-\infty}^{\infty} A(\alpha)\exp(-ik\alpha\left\{\frac{x}{q} + \frac{\xi}{p}\right\} d\alpha d\xi \right|^2 \tag{31}$$

where $A(\alpha)$ is any general pupil function. If $A(\alpha)$ is a gaussian filter, equations 30 and 31 become

$$I_{im}^{inc}(\overline{x}) = \int_{-b}^{b} I_o \left/ \int_{o}^{q} \exp(-\alpha/c)^2 \cos\left\{K\alpha(\frac{x}{q} + \frac{\xi}{p})\right\} d\alpha \right|^2 d\xi , \tag{32}$$

$$I_{im}^{coh}(\overline{x}) = \left| \int\!\!\int_{-b}^{b} \sqrt{I_o} \int_{o}^{q} \exp-(\alpha/c)^2 \cos\left\{K\alpha(\frac{x}{q} + \frac{\xi}{p})\right\} d\alpha d\xi \right|^2 , \tag{33}$$

---

* sinc $= \sin(x)/x$

28

where the slit function is defined by equations 26 and 28, 2a is the diameter of the exit pupil and c is the half width of the gaussian filter. The parameters p,q, k,b, and a, which determine the optical system, are not all completely arbitrary. These parameters have been chosen so that the size of the image is approximately ten times the width of the central maximum of the amplitude impulse response. The calculations of equations 32 and 33 were performed on a computer. In determining the effects of the apodization on the resultant image, the half width c of the filter and the pupil diameter (2a) were the only parameters allowed to vary for each run on the computer. A few typical results of the computer data have been plotted in figures seven through seventeen. Some of the important observations to be made from examining these figures are summarized here:

   i.   Since the gaussian filter is an amplitude filter, the intensities in the incoherent cases are severely reduced (figures 7, 9, 12, 15).

   ii.   If the amount of apodization is too great, $c \ll a$, the gaussian filter can act as the limiting aperture stop, thus destroying the ability to clearly recognize the image as being an image of a slit object (see figure 9).

   iii.   The ringing associated with the coherent image has almost been eliminated by the gaussian apodization (figures 8, 10, 13, 16).

   iv.   The edge shift associated with the coherent image cannot be removed (figures 11, 14, 17). In fact it appears that the gaussian apodization has no effect whatsoever upon the position of the edges of the slit. Careful examination of the slit edge in the coherent
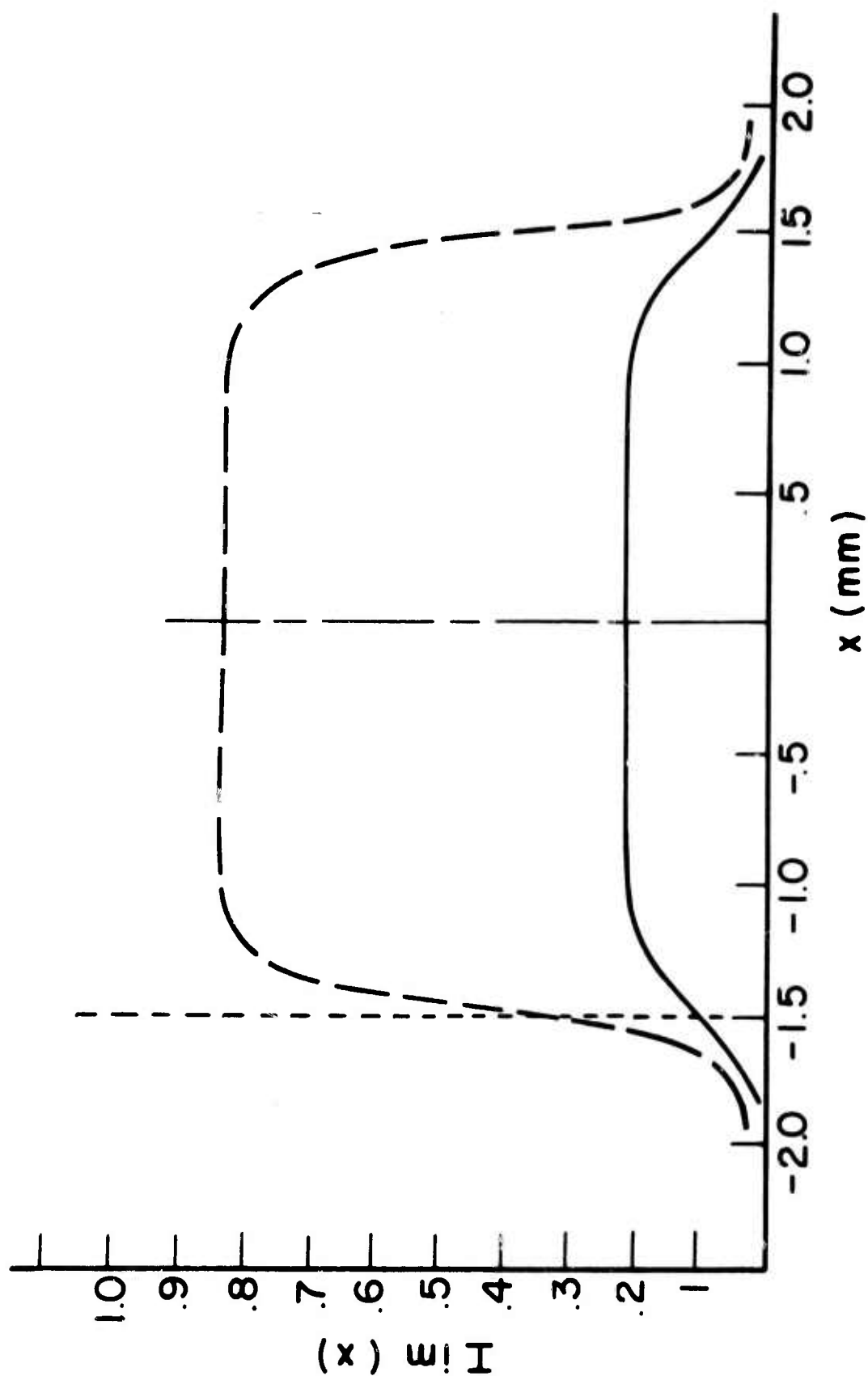
Figure 7. The intensity distribution for a slit of width 2b' = 3.0 mm. Incoherent object illumination was used. c = .4 mm, a = 1.0 mm. The vertical dotted line represents the gaussian position of the edge. (------ unapodized, ——— apodized.)
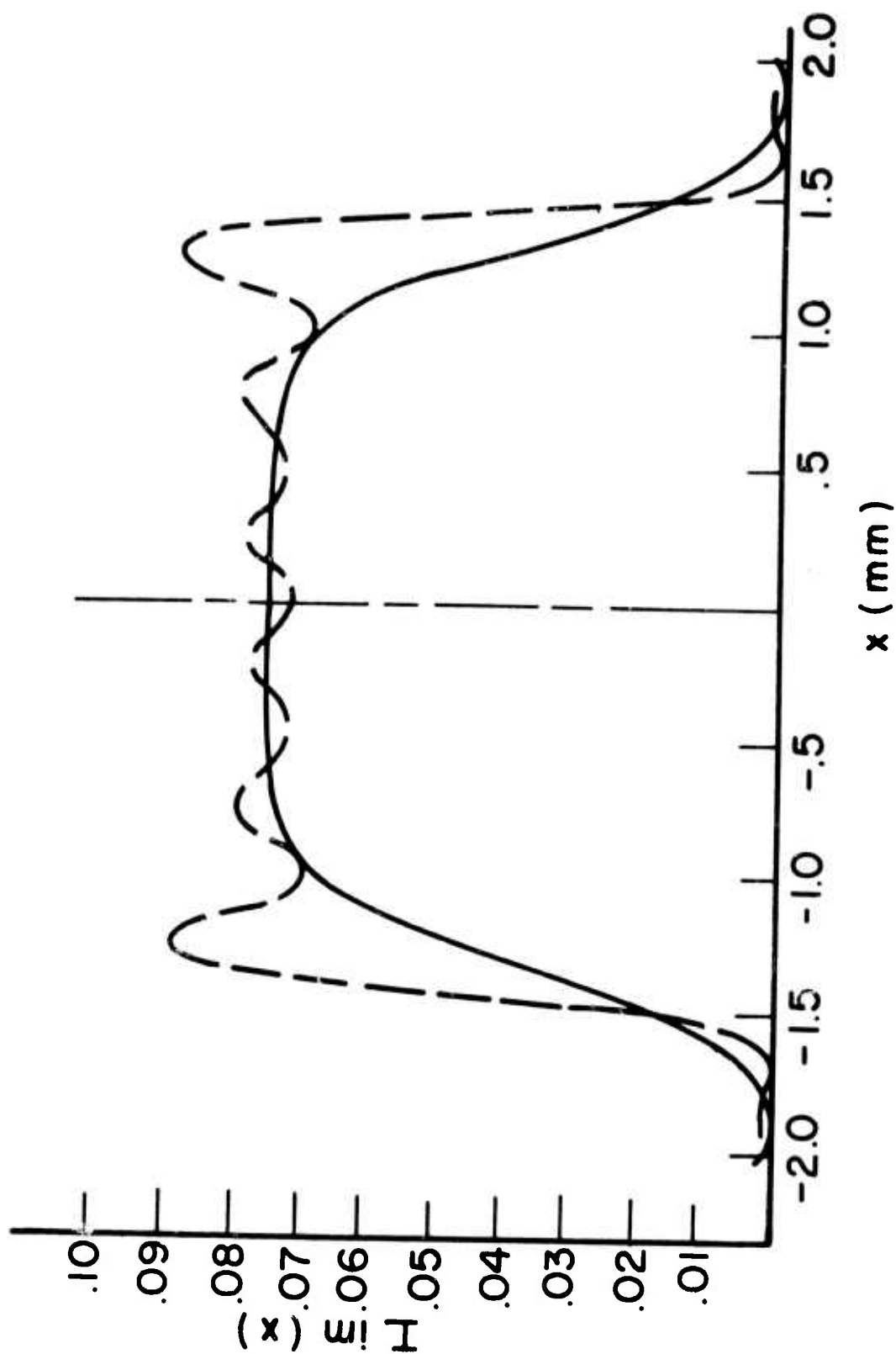
Figure 8. The intensity distribution for a slit of width 2b' = 3.0 mm. Coherent object illumination was used. c = .4 mm, a = 1.0 mm. (------ unapodized, ———— apodized.)

31

FIG. 9   The image illuminance, $I^{inc}(x)$, for a slit of width
         2b'=3.0mm. Incoherent object illumination has been
         used. c=.72mm, a=1.0mm (-------unapodized, _____
         apodized).

FIG. 10   The image illuminance, $I^{coh}(x)$, for a slit having
         the identical parameters as given in FIG. 9
         however, coherent object illumination has been
         used. (------unapodized, _____apodized).

FIG. 11   The normalized image illuminance for the case where
         the optical system has been apodized with the gaussian
         filter used in FIGS. 9 & 10   ($\cdot$-----$I^{inc}(x)$,
         _____$I^{coh}(x)$). The dotted vertical line represents
         the geometrical position of the edge.
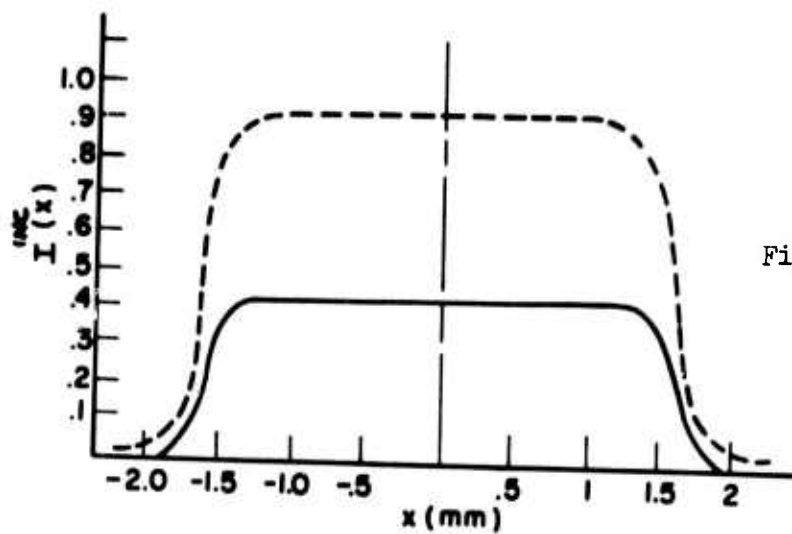
Figure 9
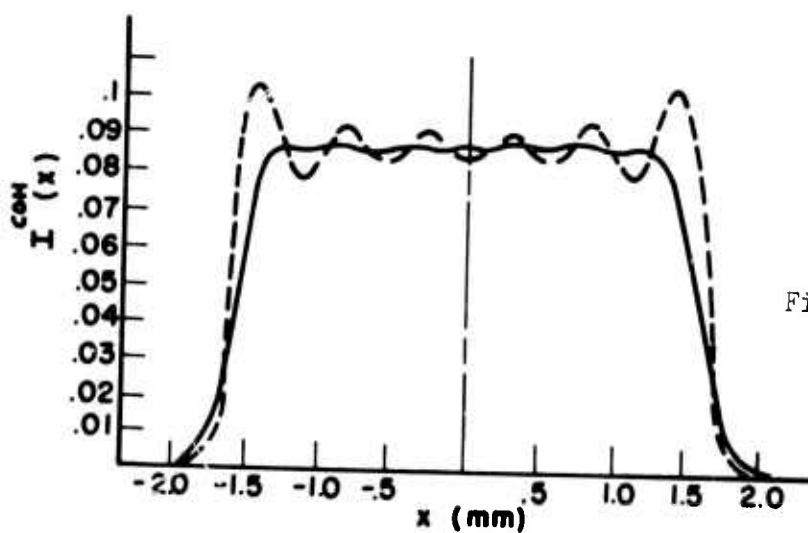
Figure 10

Figure 11

33
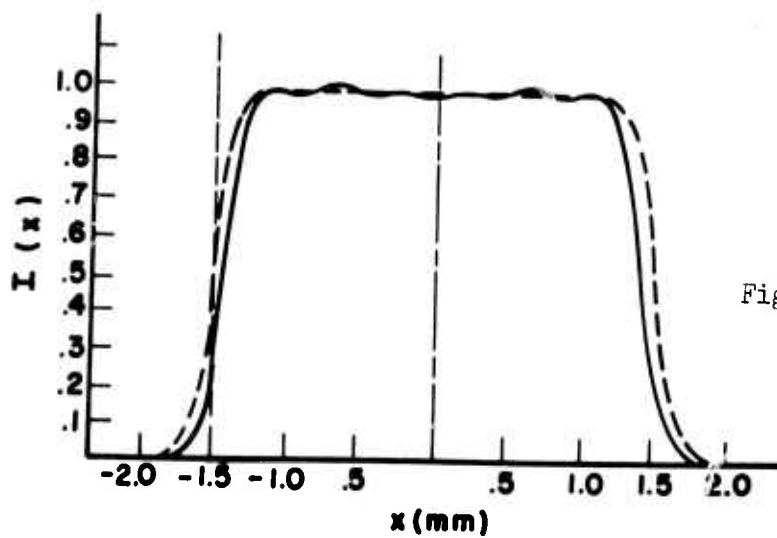
FIG. 12   The image illuminance, $I^{inc}(x)$, for a slit of width
2b'=3.0mm.   Incoherent object illumination has been
used.   c=.8mm, a=1.0mm.   (------unapodized, _____
apodized).

FIG. 13   The image illuminance, $I^{coh}(x)$, for a slit having the
identical parameters as given in FIG. 12.   However,
coherent object illumination has been used. (-----
unapodized, _____apodized).

FIG. 14   The normalized image illuminance for the case where
the optical system has been apodized with the gaussian
filter used in FIGS. 13 & 14.   (------$I^{inc}(x)$, _____
$I^{coh}(x)$).   The dotted vertical line represents the
geometrical position of the edge.

Figure 12

Figure 13

Figure 14

35
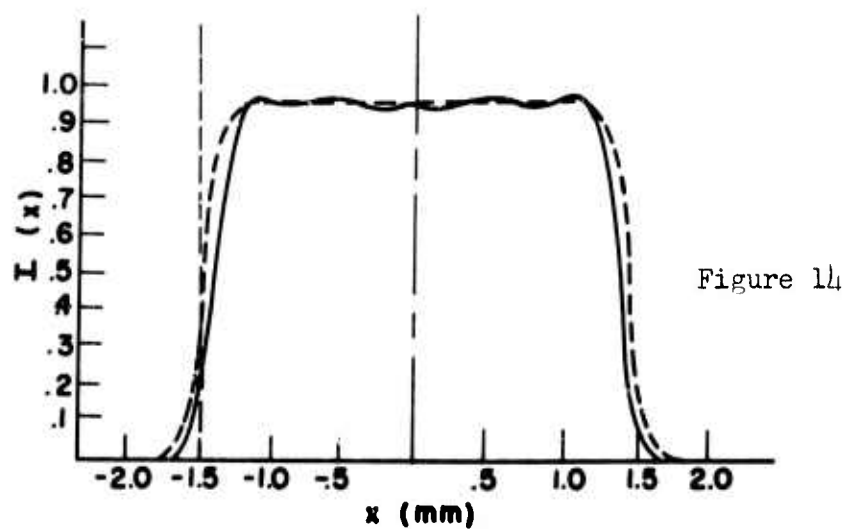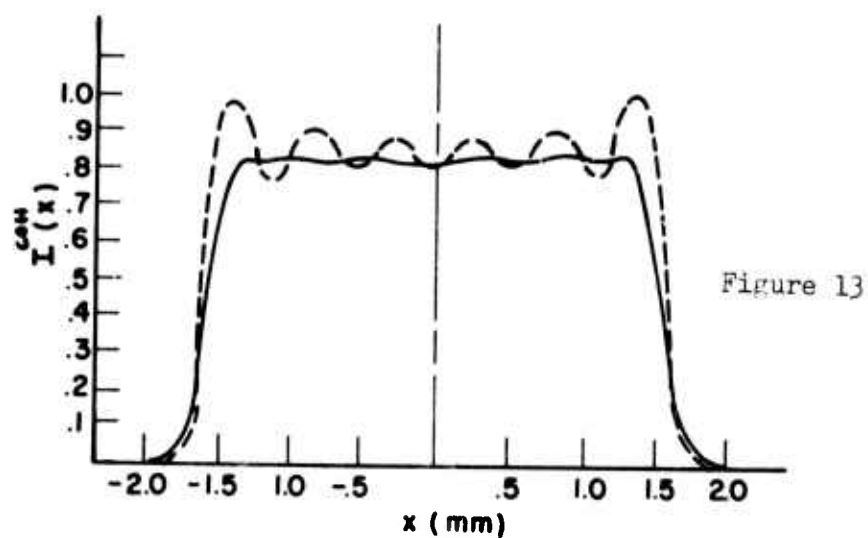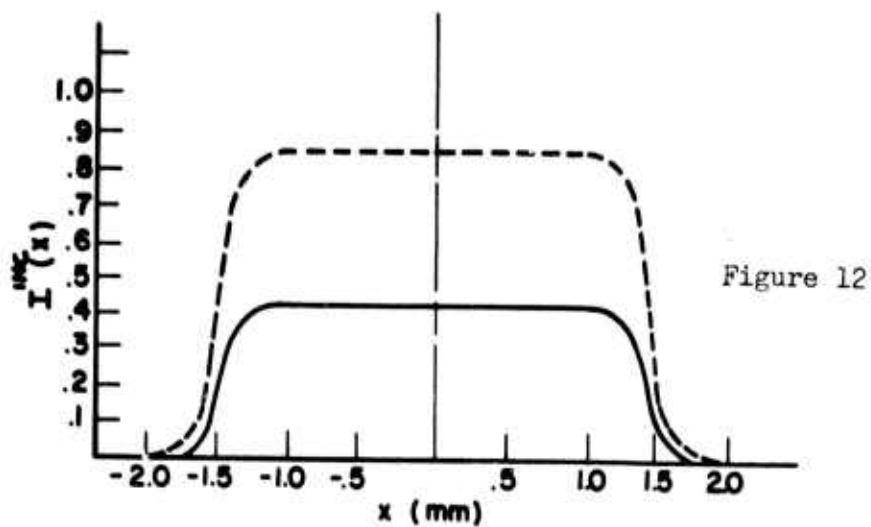
FIG. 15   The image illuminance, $I^{inc}(x)$, for a slit of width
           2b'=3.0mm. Incoherent object illumination has been
           used. c=1.0mm, a=2.0mm. (------unapodized, _____
           apodized).

FIC. 16   The image illuminance, $I^{coh}(x)$, for a slit having the
           identical parameters as given in FIG. 15.   However,
           coherent object illumination has been used. (-----
           unapodized, _____apodized).

FIG. 17   The normalized image illuminance for the case where
           the optical system has been apodized with the gaussian
           filter used in FIGS. 15 & 16   (------$I^{inc}(x)$, _____
           $I^{coh}(x)$). The dotted vertical line represents the
           geometrical position of the edge.
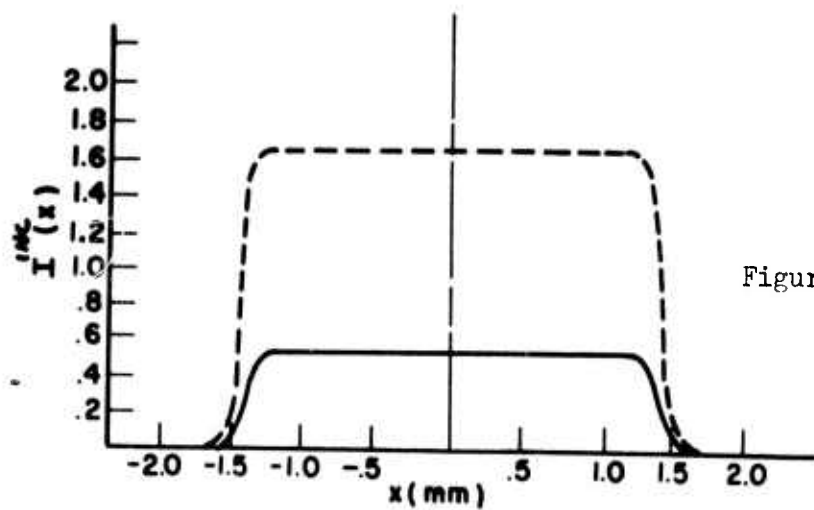
Figure 15
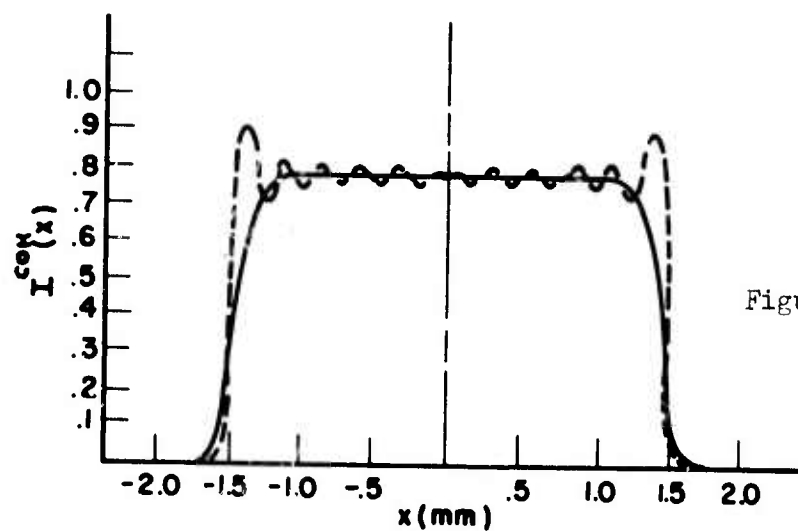
Figure 16
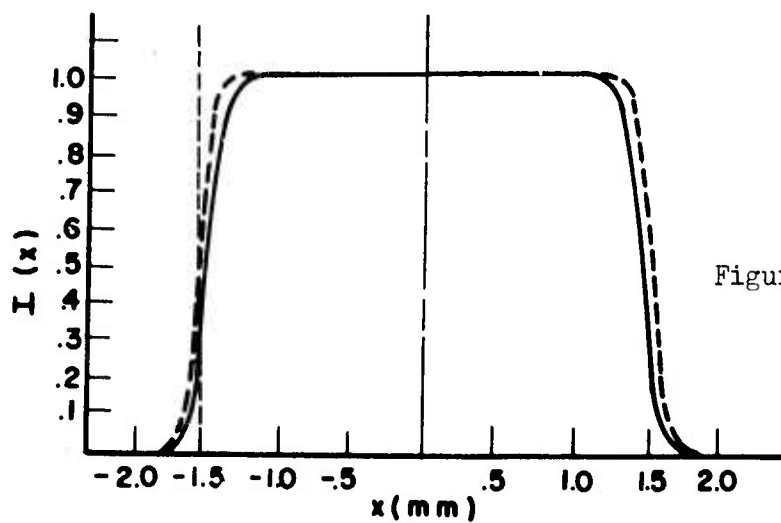
Figure 17

37

cases reveal that independent of the value of c, the relative intensity at the geometrical position of the edge is always .25.

4. CONCLUSIONS AND SUMMARY

The results have established that coherent apodization can be a useful technique in reducing coherence effects. It was shown that it was possible to reduce image shifting, for $\gamma = 1$, by using the gaussian apodization. With this same apodization, edge ringing for slit objects was also reduced but the mensuration problems associated with the edge of the slit remained unaffected. These results indicate that perhaps some coherence effects are caused by factors other than the shape of the amplitude impulse response.

Until now attention has been focused upon changing the form of the amplitude impulse response. However, the nonlinearity of the coherent process has not been considered. It now appears that the nonlinearity, rather than the structure of the amplitude impulse response, is responsible for these mensuration problems. As an illustration of this point, consider figure 18. As shown, a rectangle function* has been used as an approximation for the intensity and amplitude impulse response. Figures 18a, b, and c, illustrate the formation of an image $I_{im}^{inc}(x)$, for the incoherent process. With $I_{ob}(\xi)$ also being a rectangle function, the convolution of this function with $S(x-\xi)$ (figure 18 b), results in the image shown in figure 18c. Note that the sloped regions are linear and that at the geometrical position of the edge (indicated by the dotted line), the intensity value is .5 units. The corresponding coherent process is shown in figures 18d, 18e, 18f, and 18g. Each

---

* rectangle function $= \operatorname{rect}(x) = \begin{array}{ll} 1 & |x| \leq 1/2 \\ 0 & |x| > 1/2 \end{array}$

39
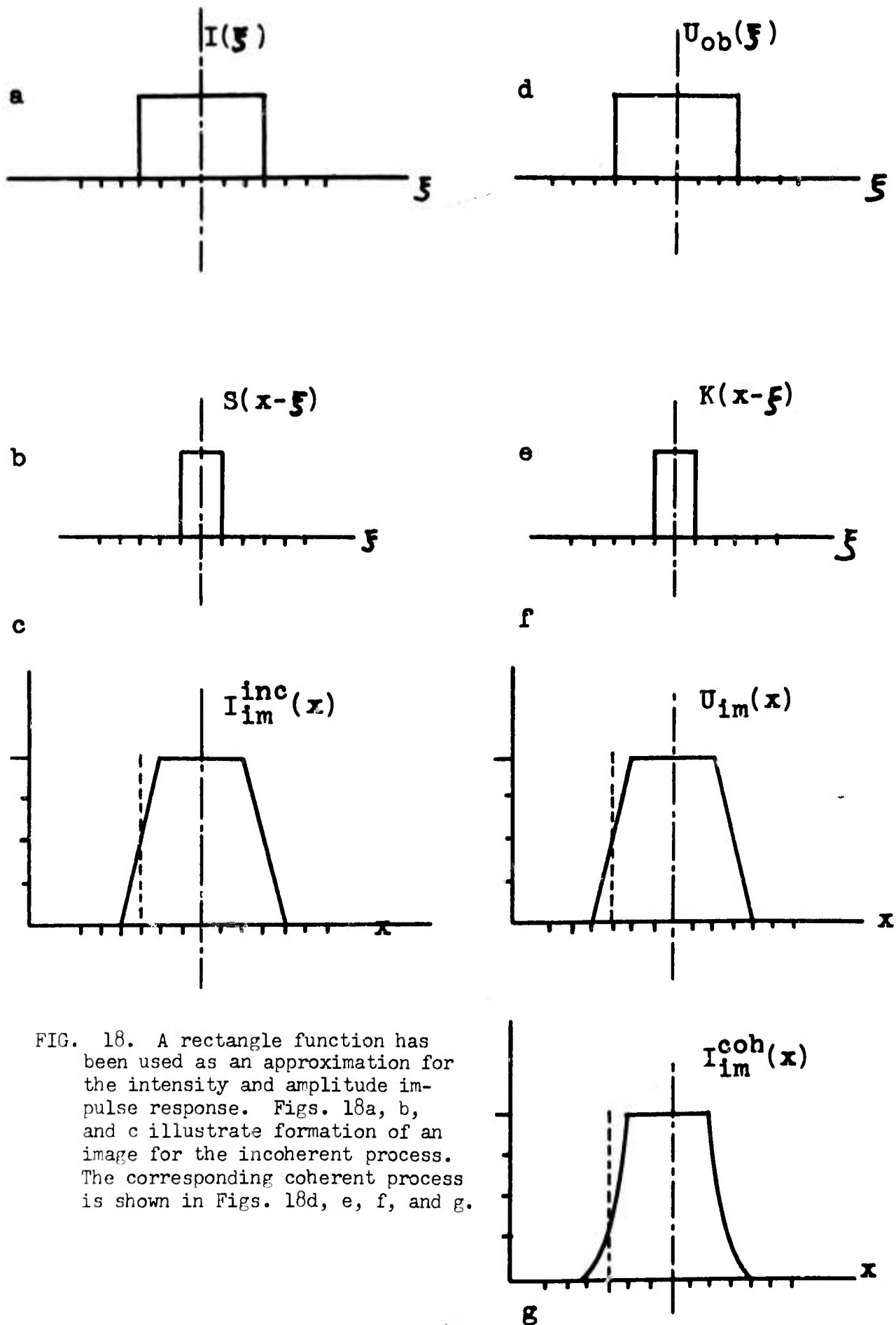
FIG. 18. A rectangle function has been used as an approximation for the intensity and amplitude impulse response. Figs. 18a, b, and c illustrate formation of an image for the incoherent process. The corresponding coherent process is shown in Figs. 18d, e, f, and g.

step in the coherent process is similar to that in the incoherent process, but the indicated operations are performed in amplitude rather than intensity. The final step in the coherent process, figure 18g, is to square $U_{im}(x)$ to obtain the measurable quantity, $I_{im}^{coh}(x)$. The important observation is that the sloped region is no longer linear. The squaring operation has caused the intensity value at the geometrical position of the edge to be .25 units. In fact each intensity value in the sloped region of figure 18g, is now less than the corresponding intensity value of figure 18c. Thus the edge of the slit appears to have shifted inwards, as compared to the incoherent process. It should now be apparent that mensuration problems which arise in coherent imaging processes are caused by the nonlinear process, rather than by the structure of the amplitude impulse response.

It has clearly been shown that the degradation of an image in a coherent optical system is not an immutable consequence of using coherent illumination. In apodizing the exit pupil with a gaussian filter, image shift for two coherent point objects was considerably reduced. By extending this technique to slit objects, two important facts were determined. First, edge ringing could also be reduced with the same apodization. Secondly, mensuration problems were found to be caused by the nonlinearity inherent in the coherent process, rather than the structure of the amplitude impulse response.

Although a general technique of coherent apodization has been outlined here, there remain areas in which this work may be extended. Certainly one should consider how this apodization affects the image of objects which have

phase as well as amplitude variations associated with them. It would also be interesting to examine the possibility of having phase variations associated with the filter function $A(\alpha)$. In fact, now that it has been shown that coherent apodization can improve image quality in coherent optical systems, these techniques should be rigorously applied in finding the optimum filter function $A(\alpha)$.

REFERENCES

1. R.E. Kinzly, "Investigations of the Influence of the Degree of Coherence upon Images of Edge Objects," JOSA 55, 1002, (1965).

2. B.J. Thompson, "Image Formation with Partially Coherent Light," Progress in Optics Vol. VII, 171, (ed. E. Wolf), North Holland Publishing Co., (1969).

3. D.N. Grimes and B.J. Thompson, "Two point Resolution with Partially Coherent Light," JOSA 57, 530, (1967).

4. T.J. Skinner, Ph.D. Thesis, Boston University, ch. 8.3, (1964).

5. E. Wolf, "The Diffraction Theory of Aberrations," Repts. Progr. Phys., 14, 95, (1951).

6. R.K. Luneberg, Mathematical Theory of Optics, Brown University Press, Providence, (1944).

7. H. Osterberg and J.E. Wilkens, "The Resolving Power of a Coated Objective," JOSA 39, 553, (1949).

8. H. Osterberg and F. Wissler, "The Resolution of Two Particles in a Bright Field by Coated Microscope Objectives," JOSA 39, 558, (1949).

9. R. Barakat, "The Intensity Distribution and Total Illumination of Aberration-Free Diffraction Images," Progress in Optics Vol. I, 67, (ed. E. Wolf), North Holland Publishing Co., (1969).

10. P. Jacquinot and B. Roizen-Dossier, "Apodization," Progress in Optics Vol. III, 29, (ed. E. Wolf), North Holland Publishing Co., (1969).

11. J.T. Kauffman, "The Calculated Radiation Patterns of a Truncated Gaussian Aperture Distribution," IEEE Trans. Applied Physics, AP-13, 473, (1965).

12. A.L. Buck, "The Radiation Pattern of a Truncated Gaussian Aperture Distribution," Proc. IEEE 55, 448, (1967).

13. A.L. Bloom, Gas Lasers, John Wiley and Sons, Inc., 114, (1968). A.L. Bloom and D.J. Innes, Spectra-Physics Laser Technical Bulletin No. 5, Spectra-Physics Corp. Pub., Mountain View, California.

14. J. Campbell and L. Deshazer, "Near Fields of Truncated-Gaussian Apertures," JOSA 59, 1427, (1969).

15. C.M. Sparrow, "On Spectroscopic Resolving Power," Astrophysical J, 44, 76, (1916).

16. R. Barakat, "Application of Apodization to Increase Two-Point Resolution by the Sparrow Criterion I. Coherent Illumination," JOSA 52, 276, (1962).

17. H.H. Hopkins,"The Concept of Partial Coherence", Proc. Roy Soc. London A 208, 263, (1951).

18. P.S. Considine, "Effects of Coherence on Imaging Systems," JOSA 56, 1001, (1966).

19. G.B. Parrent and B.J. Thompson, J. Soc. Photo-Opt. Inst. Engr. 5, 206, (1967).

B. DEVELOPING METHODS TO STUDY BEAM PARAMETERS OF A PULSE LASER

C. Roychoudhuri and B.J. Thompson

1. INTRODUCTION

In many applications of laser beam technology like coherent optical processing, coherent light ranging, laser beam scanning, etc., a knowledge of the complex amplitude distribution over the output wavefront is often essential. In precision shop techniques like micro etching and welding, or in initiating controlled fusion by high energy laser beams, the knowledge of the spot size and the energy distribution of the focused laser beam is extremely important. These parameters can be determined very easily from the knowledge of the near field complex amplitude distribution. For certain optical techniques the information about the far field distribution may be the more relevant quantity; this can also be determined from the knowledge of the near field distribution, using the diffraction integral if the beam is incoherent or the mutual intensity propagation integral if the beam is partially coherent. The objective of this study is to develop a method by which the complex amplitude distribution (and ultimately the mutual intensity function) of a laser beam near field can be determined.

45

2. POSSIBLE METHODS

In principle the determination of the intensity distribution across a wavefront is straightforward since an optical detector responds to the light intensity. But the problem of recording the phase distribution of an unknown wavefront is of fundamental nature, especially if the wavefront is not a very simple one.

One may apply the Fourier transform technique: record the square modulus of the Fourier transform of the unknown wavefront and then the inverse Fourier transform may be used to find out a partial knowledge of the original wavefront. The problem of complete phase retrieval[1] is still there, as we can gather a knowledge only of the modulus of the Fourier transform instead of the complex Fourier transform.

Interferometry offers a better method of recording the complex amplitude. since interference gives rise to modulation in the resultant intensity. The modulation is directly affected by the degree of coherence and the amplitude of the interfering beams. In applying this technique to study laser beam wavefronts, especially if they are pulsed, the required reference beam will have to be generated from the very wavefront to be studied.

The simplest application of the interference technique

46

is to record a shearing interferogram[2] of the wavefront. But the interpretation of the interferogram may not be the simplest one, especially for complicated wavefronts. The reason is that both of the interfering wavefronts are unknown. A simple and elegant solution to this problem is to generate a known local reference beam (l.r.b.) by splitting off a part of the wavefront to be studied and focusing it onto a small pinhole aperture generating an approximately spherical wavefront, or a plane wavefront with the help of an auxiliary lens as shown in fig. 19.

Now for a complete knowledge of the relative phase and the amplitude distribution of a wavefront, we also need to know the intensity distribution of the two wavefronts. For pulsed laser systems it may be very difficult to get a simultaneous record of the intensity pattern of the two interfering beams along with the interferogram. An obvious solution to this problem is to record the wavefront holographically and to study the reconstructed beam at leisure using a steady continuous laser for reconstruction.

Here it is worth recognizing that the interferogram of fig. 19 is already a hologram but only of less usefulness as it is an "on-axis" hologram and in the reconstruction the wanted wavefront will be mixed up with unwanted wavefronts traveling in the same direction. The solution is already known: Leith and Upatniek's[3] off-axis hologram arrangement.

47
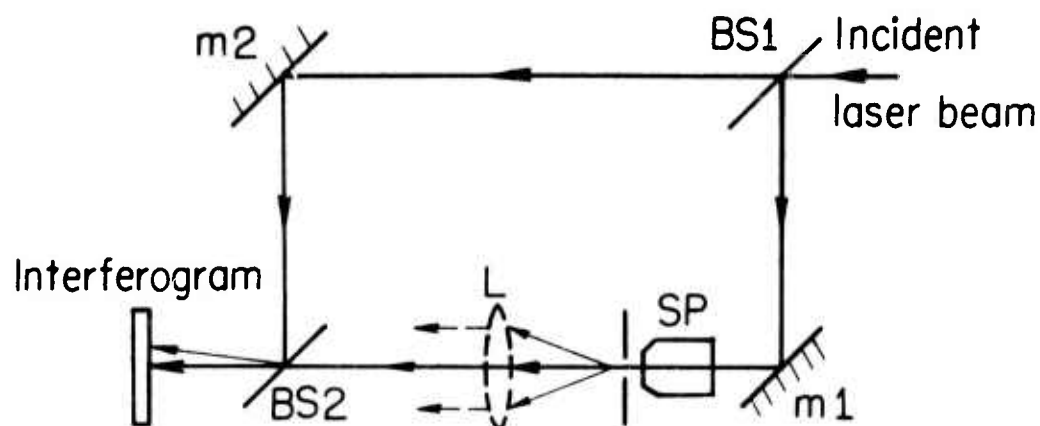
Fig.19 LOCAL REFERENCE BEAM INTERFEROMETRY.

SP - Spatial filter, L - Collimating Lens, BS1 &
BS2 - Beamsplitters, m_1 & m_2 - mirrors.
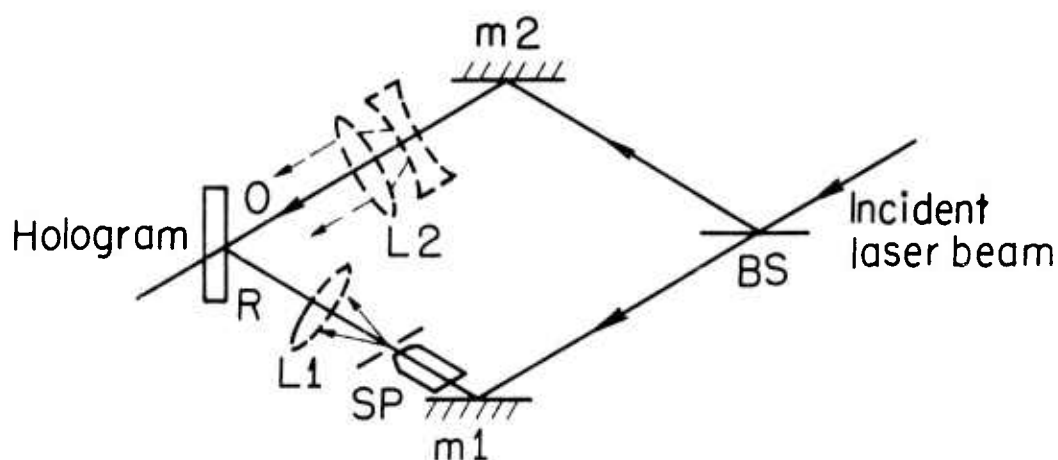
Fig 20 LOCAL REFERENCE BEAM HOLOGRAPHY.

R - local reference beam; O -'object' beam;

SP - spatial filter; L1 - collimating lens;

L_2 - optional beam expander;

BS - beam splitter; m_1 & m_2 - mirrors.

48

We propose the holographic arrangement as shown in fig. 20.
If necessary, the "object" beam could be expanded using a
suitable lens system.

There is one important point to be emphasized here
regarding the l.r.b. It will have to be a uniform and
clean wavefront both in phase and amplitude in order to
insure a faithful reconstruction. A suitable spatial
filter (a pinhole of suitable size with a matching micro-
scope objective) serves this purpose very well generating a
uniform, clean, and approximately spherical wavefront.

We now state our method of determining both the phase
and the amplitude distribution of a pulse multimode laser
wavefront. We are exploiting both l.r.b. holography and
interferometry, but in two independent steps. The first step
is to record a hologram of the pulse wavefront by l.r.b.
holography with an arrangement shown in simplified form in
fig. 20. Then the wavefront is reconstructed using a continuous
TEM_{00} mode laser beam, and the reconstructed wavefront is
interfered with a uniform plane wavefront. The coherent
plane wavefront can be easily derived from a part of the same
laser beam used to generate the reconstruction wavefront, as
shown in fig. 21. The interferogram gives complete information
about the phase and amplitude distribution of the multimode
laser wavefront. Our method offers a powerful flexible
method to study a pulse multimode laser wavefront, since the

49
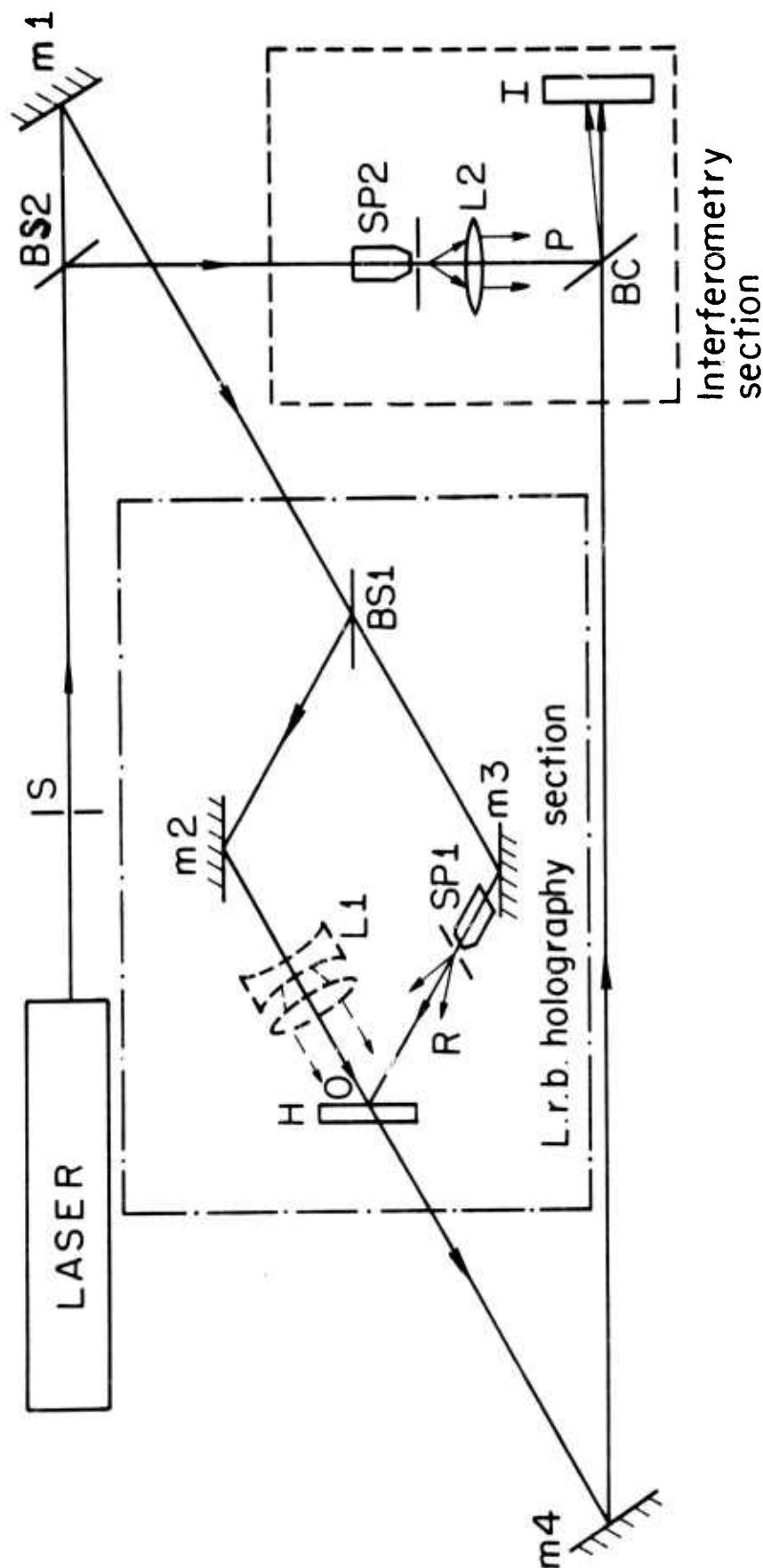
Figure 21. L.r.b. holography to record a pulse laser wavefront and its subsequent study through interferometry. H, hologram plane; I, interferogram plane; O, "object" beam; P, plane wavefront for interferometry; SP1 and SP2, spatial filters; BS1 and BS2, beam splitters; L1, optional beam expander; L2, collimating mirrors; S, shutter.

pulse laser wavefront can be regenerated as a stationary

one. Its parameters can be studied by a variety of methods.

3. EARLY L.R.B. TECHNIQUES

a. Interferometric Techniques

While working with this local reference beam method, we

came to realize that our ideas were not entirely unique. A

related method was first suggested by Korobkin and Leontovich[4]

in early 1963. They studied the degree of spatial coherence

of a ruby laser by interfering waves from separate sections

of the wavefront. Their experiments indicated a high degree

of spatial coherence between the different parts of the wave-

front, but did not (and can not) give structure of the phase

front as a whole.

Bondarenko et al.[5] carried out another experiment in

late 1963 in which the output of a ruby laser was interfered

with a spherical wavefront generated by scattering a small

central part of the main beam through a transparent dielectric

nonuniformity. Essentially the same kind of study was also

done by Davis[6] in 1967. He used an appropriately

coated plano-concave lens to produce the axially symmetric

primary "object" beam reflected from the plane surface and

the spherical local reference beam reflected from the

concave surface.

Both the above methods can give rise to reliable determination of the phase structure only for a completely coherent wavefront. For a partially coherent wavefront the above methods might even be very misleading in interpreting the phase information structure from the fringe structure; and as such they are not suitable for studying multimode pulse laser wavefronts.

For more convenient and quantitative mapping of a complicated phase structure, the reference wavefront should preferably be a plane and uniform one. Miyamoto and Yasuura[7] nearly demonstrated such an experiment. They were also measuring the phase and amplitude distribution of a laser wavefront, only their laser was a continuous He-Ne type running in a single transverse and single longitudinal mode. Their reference wave was produced by splitting off a part of the laser beam; it was then expanded and collimated by a pair of positive lenses. Like the methods of Bondarenko et al. and Davis, this is also an unsatisfactory method for studying multimode laser wavefronts.

A versatile local reference beam should be produced by using the entire cross-section of the laser beam and sending it through a spatial filter.

b. Holographic Techniques

It appears from patent literatures that Cathey[8] was the first to invent the idea of generating a local reference

52

beam (l.r.b.) for holography. Instead of using a separate external reference beam, he passed a part of the object beam through a lens and pinhole assembly to the hologram. Since Cathey's idea occurred in the patent literature the idea was not well known to the scientific community.

In early 1967, Rosen and Clark[9] experimented with holography without any external reference beam; but their idea was not as versatile as that of Cathey's. Their object was very close to the hologram plane and interference between the different parts of the object gave rise to the hologram; reconstruction of one part of the object was carried out by illuminating the hologram by the appropriate part of the object beam.

In late 1967, Caulfield et al.[10,11] apparently reinvented Cathey's idea of generating an easily reproducible local reference beam. Their original goal was to avoid the problem of path matching between the object beam from an unknown distance and the external reference beam in the conventional Leith-Upatniek type of off-axis holography. Caulfield[12] then realized that this idea of l.r.b. holography could be extended further to make holograms of any object of any extent and distance, and suggested the construction of a holographic camera with a laser as the "flash."

All the above mentioned works are very much confined to the realm of pictorial holography. Then in early 1970, we

started our work to develop a method of measuring the
parameters of a pulse laser beam running in unidentifiable
multimode; and we too reinvented Cathey's result but with
more versatility. As mentioned in the previous section, we
started with the idea of recording the pulse laser wavefront
by l.r.b. holography and then studying all the beam parameters
at leisure by using a continuous TEM_{OO} laser beam for recon-
struction. To test the resolution capabilities both in
amplitude and phase of the method, we ran three sets of
experiments with a TEM_{OO} He-Ne laser and simulated the non-
uniform wavefront by using suitable masks in the laser beam.
These experiments are described in the following sections.

Before concluding this section we should mention some
of the publications which have some relationship to our work.
Lurie[13], Murata et al.[14,15], Ross[16] ,and Aleksoff[17]
have done some work on holographic measurement of coherence.
Aleksoff's recent note[18] on "Holographic Analysis and
Display of Laser Modes" is also worth mentioning here. In
our future work on the measurement of the mutual intensity
function of a pulse laser wavefront, we shall discuss the
limitations and shortcomings of some of the relevant papers
mentioned here.

4. TEST EXPERIMENTS

a. L.R.B. Holography to Reconstruct Intensity Distribution

In this preliminary series of experiments we have successfully demonstrated that l.r.b. holography can reconstruct quite rapidly varying intensity distributions. This establishes two fundamental requirements of any local reference beam for holography. That there is a reconstruction at all, establishes the essential requirement that the local reference beam is a clean and uniform beam. The faithfulness of the reconstruction demonstrates the reproducibility criterion of the l.r.b. This is an important point for us as we are going to make holograms of a pulse laser wavefront with l.r.b. from the same pulse and then reconstruct it by regenerating the reference beam from a different laser.

Since the test experiment was peiformed with a continuous He-Ne laser running in the TEM_{oo} mode, the rapidly varying intensity distribution was simulated by inserting known masks in the beam. The experimental arrangement is shown in fig. 22 The He-Ne laser beam is diffracted by the known mask M, and the diffracted beam is divided into two parts with the help of the beam splitter BS. The part which goes through straight is used to generate the l.r.b. with the help of the spatial filter SP. The reflected part constitutes the simulated rapidly varying amplitude variation of a "multimode" pulse
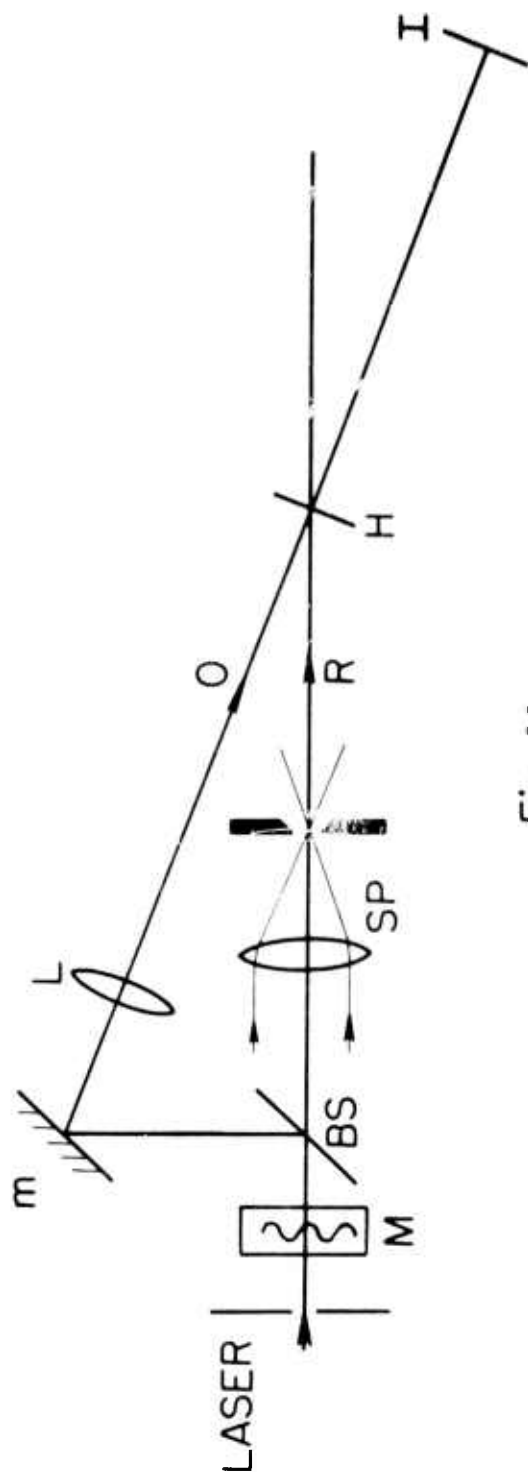
Fig. 22

M – mask; L – lens; SP–spatial filter; O – 'object' beam;

R – spherical local reference beam; H– hologram plane;

I – direct or reconstructed 'object' beam recording plane;

BS – beam splitter; m – mirror

Test experiment on l.r.b. holographic technique with simulated multimode laser.

56

laser; this is our object beam. Choosing different focal
lengths for the lens L we can control two different properties
(although intimately related) of the object beam: first, the
frequency of amplitude variation at the intensity recording
plane I and the relation between the mask M and diffracted
beam received by the hologram.

Two sets of records were taken using two different masks:
an amplitude Ronchi ruling and a phase Ronchi ruling. In
each case we recorded holograms under three different condi-
tions using lenses of appropriate focal lengths for L such
that the hologram appeared to be successively in the (i)
Fraunhofer plane, (ii) Fresnel plane and (iii) image plane
with respect to the diffracting mask M. The reason for record-
ing three different plane-holograms is to test the precise
reproducibility of the reconstructing l.r.b. For example, it
is established[19] that the quality of the reconstructed
image from an image plane hologram is least sensitive to
deviations in the reconstructing beam from that of the
original reference beam; it is a little more sensitive for a
Fresnel plane hologram. The highest sensitivity is for the
Fraunhofer plane hologram. This is because the amplitude
corresponding to the frequency spectrum of an object is
spatially dispersed over the Fraunhofer plane; consequently
any distortion in any part of the reconstructing beam would
lead to a distortion all over the object corresponding to
that spatial frequency content of the object. Whereas for

57

image plane holograms, a local distortion in the reconstructing beam will produce, at best, a corresponding local distortion in the object; this is nearly true for Fresnel plane holograms too.

The recorded results shown in figure 23 and 24 are arranged in an identical sequence, the only difference is that fig. 23 corresponds to the amplitude Ronchi ruling mask and fig. 24 corresponds to the phase Ronchi mask. In both the diagrams the three successive columns correspond to (i) Fraunhofer plane, (ii) Fresnel plane and (iii) image plane holographic arrangements as mentioned earlier. The pictures in the first row are the direct record of the object beam. The second row corresponds to the reconstruction by the original l.r.b. and the third row represents records of the reconstruction by a l.r.b. generated from a "different" laser beam.

It can be noted, from a careful comparison of the last two rows of each column of both figures 23 and 24 that the reconstructions by the original l.r.b. and by a l.r.b. generated from a different laser are remarkably similar. It may also be noted that all three columns show almost equal faithfulness in reconstruction. Apparently, the different plane holograms do not show different resolution capability. This establishes very strongly that the l.r.b. generated from a different laser very closely resembles the original l.r.b. It is worth

58

FRAUNHOFER PLANE   FRESNEL PLANE   IMAGE PLANE
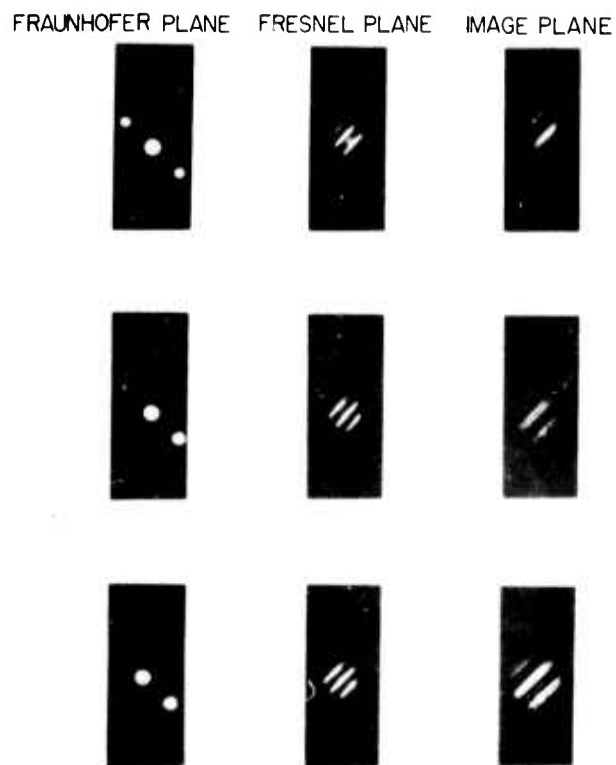
THE NOISY LASER WAVE FRONT WAS
SIMULATED BY AN AMPLITUDE RONCHI MASK
FIRST ROW DIRECT RECORD, SECOND ROW
RECONSTRUCTION WITH THE ORIGINAL LASER,
THIRD ROW RECONSTRUCTION WITH A
"DIFFERENT" LASER

Fig. 23

First set of results of the test experiment
referred to in Figure 22. Accuracy in the
reconstruction of the intensity distribution
is demonstrated.

FRAUNHOFER PLANE   FRESNEL PLANE   IMAGE PLANE
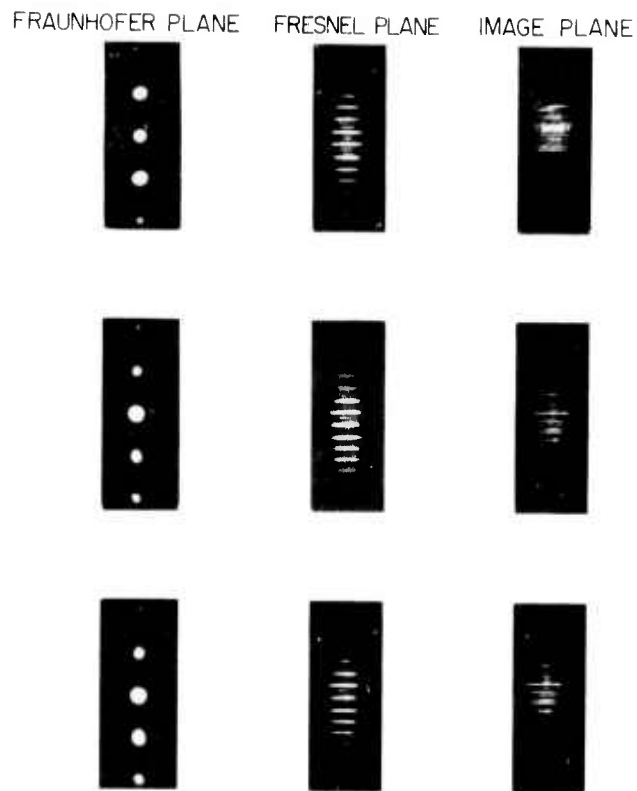
THE NOISY LASER WAVE FRONT WAS
SIMULATED BY A PHASE RONCHI MASK.
FIRST ROW: DIRECT RECORD, SECOND ROW:
RECONSTRUCTION WITH THE ORIGINAL LASER,
THIRD ROW: RECONSTRUCTION WITH A
"DIFFERENT" LASER.

Fig. 24

Second set of results of the test experiment
referred to in Figure 22. Accuracy in the
reconstruction of the intensity distribution
is demonstrated.

mentioning that our reconstructed images(second and third rows) show a slight deviation from the directly recorded images (first row). This is a defect of the very holographic process. The amplitude variation of the "object" beam was apparently beyond the linear region of "transmittance vs. exposure" curve for the hologram. This can be taken care of by choosing a suitable beam balance ratio and a mean exposure level. The other defect is due to the "hostile" environment we are working in. The entire building vibrates in a wide spectrum of frequency of appreciable amplitude. The spring-mounted massive table top on which we are working now, still vibrates with some high frequency, although of very low amplitude. This obviously deteriorates the hologram records.

b. L.R.B. Holography to Reconstruct Phase
   Structure and Subsequent Interferometry
   to Study Phase and Amplitude of a Wavefront

As in the previous experiment the phase and amplitude variation on the laser wavefront was simulated by inserting a suitable phase mask in the beam. The experimental arrangement shown in figure 25 is essentially the same as that shown in figure 21. The lens L1 images the phase mask on to the interferogram plane I where it interferes with a uniform plane wavefront generated from a part of the original laser beam with the help of the spatial filter SP2 and the collimating lens L2.
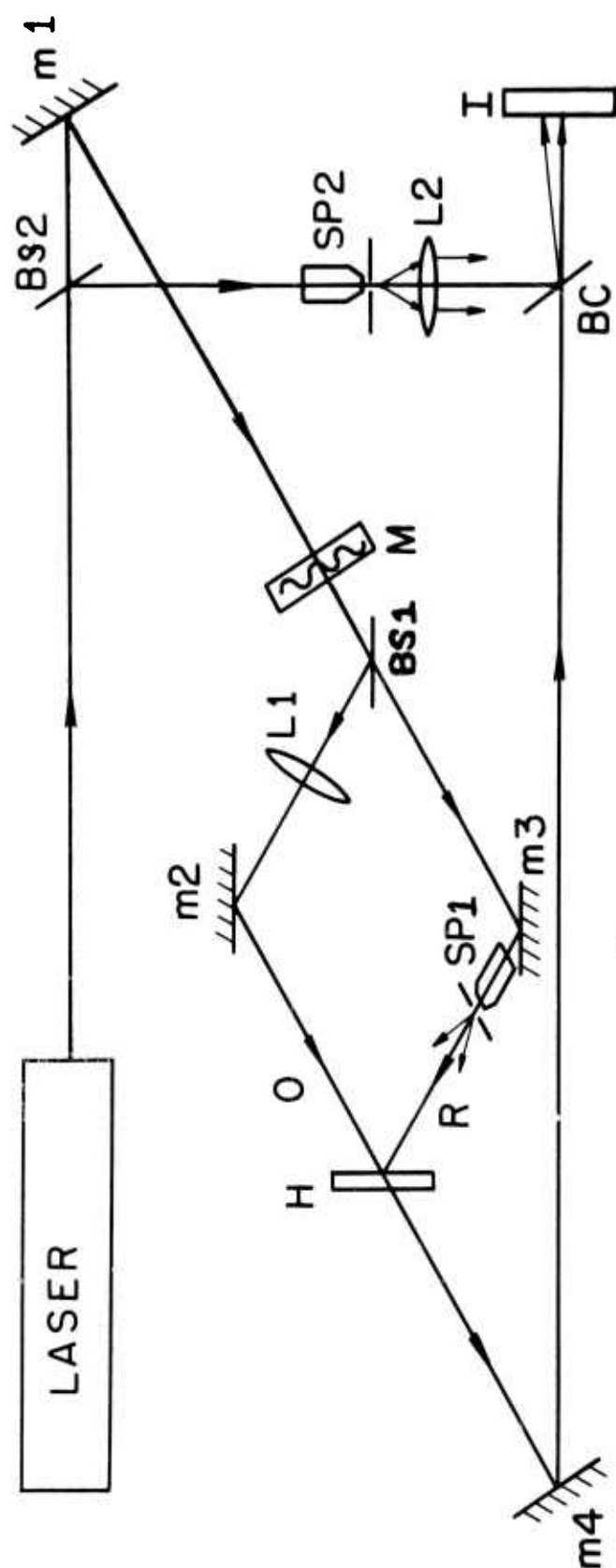
Fig. 25

H – hologram plane; I – interferogram plane; R – local reference beam;

O – 'object' beam; P – plane wave front for interferometry. M – mask;

SP1 & SP2 – spatial filters; BS1 & BS2 – beam splitters; BC – beam combiner;

L1– imaging lens; L2 – collimating lens; m_1, m_2, m_3 & m_4 – mirrors.

Test experiment on l.r.b. holography to record simulated multimode laser wavefront and its subsequent study through interferometry.

The first experiment was done with a Ronchi phase mask.
Figure 26 shows the interferograms of the phase wavefront
recorded directly and from the holographic reconstructions
with l.r.b. generated under different conditions. Interfero-
gram (a) was recorded from the direct object beam and (b)
was recorded from the reconstructed object beam, the recon-
struction being carried out with the help of the original
l.r.b. The interferograms (c) and (d) correspond to recon-
struction of the hologram carried out by l.r.b.'s generated
from different laser beams. For (c) the l.r.b. was generated
from the laser beam which was passed through the mask M and
an ordinary cellophane paper before the spatial filter SP1.
For (d) the l.r.b. was generated from the clean laser wave-
front without any mask in the beam.

Like the previous experiment, the detail similarities
in the fringe contour and relative visibility of (b) with respect to
those of (a) establish   the faithfulness of the holographic
process, and the similarities of (c) and (d) to (b) demonstrate
the reproducibility of the l.r.b. from different laser wave-
fronts. The idea behind recording the interferogram (c) with
a cellophane mask in front of the l.r.b. generating spatial
filter was to check the reproducibility of the l.r.b. even
when the frequency of the phase variation of the laser beam
is very high and irregular.
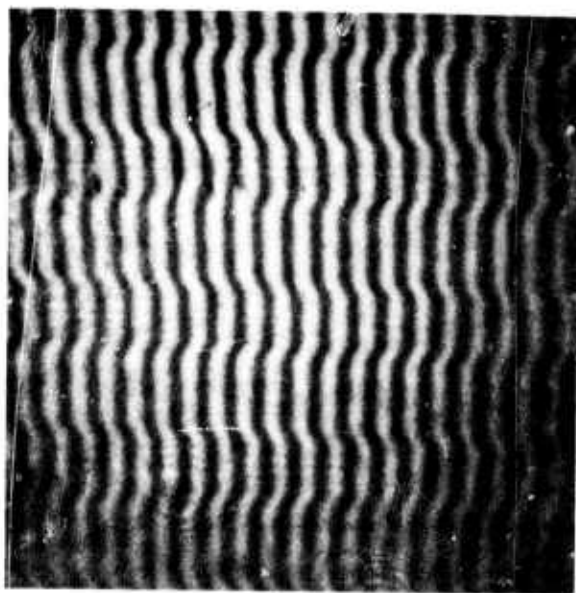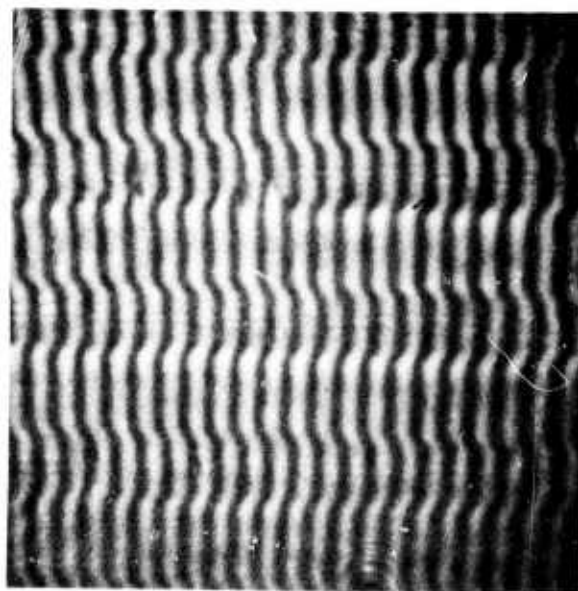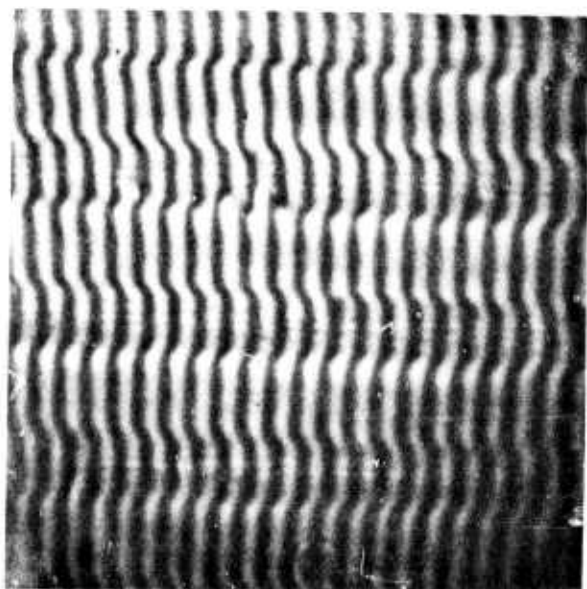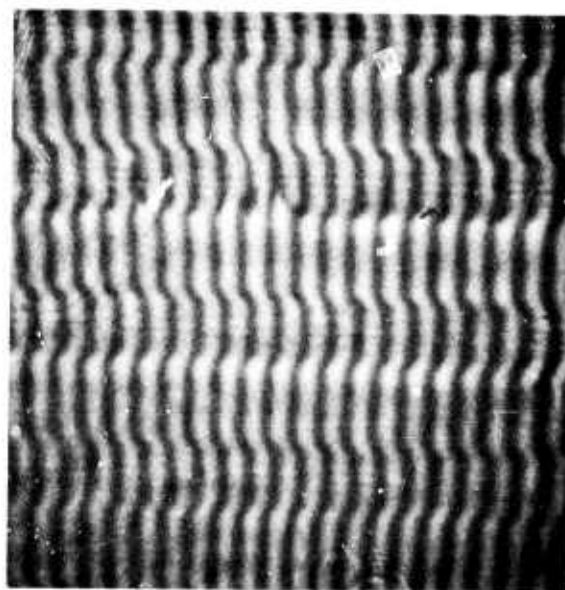
Figure 26. First set of results of the test experiment referred to in Figure 25. Accuracy in the reconstruction of a fixed frequency phase distribution is demonstrated.

The second experiment was performed with a standard resolution testing phase bar-target. This mask introduces changes in amplitude and phase of varying frequency over the wavefront. The interferograms are shown in figure 27.

As in the previous set of experiments the comparison of (c) and (d) with (a) and (b) in figure 27 establishes the faithfulness of the holographic process and the reproducibility of the l.r.b. from different laser wavefronts. We have established an additional point here. Since high frequency bar sets have been reconstructed as well as low frequency ones, we can apply our l.r.b. techniques to record even a very noisy laser wavefront like "filamentary" output from a pulsed solid state laser.

The analysis of the interferograms of the above experiments offers the obvious possibility of studying both phase and amplitude of the reconstructed wavefronts from the contour and visibility of the fringes since the reference beam for interferometry is completely known.

5. CONCLUSIONS

In this present report we have demonstrated through some simulated experiments the possibility of studying the beam parameters of a pulsed laser wavefront with the help of l.r.b.

(a) (b)
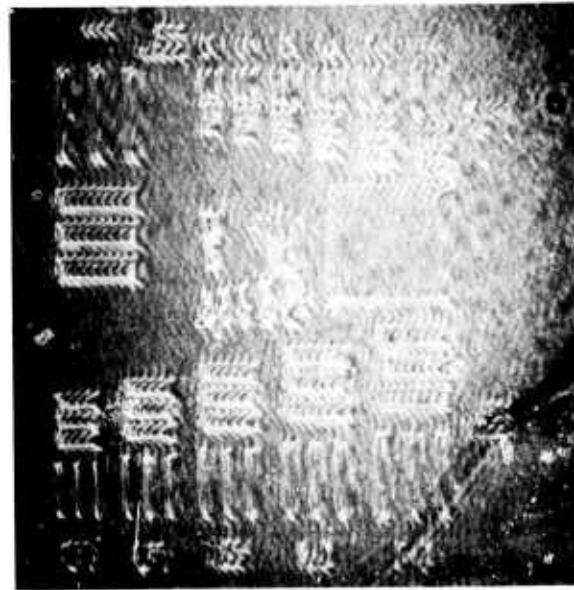
(c) (d)

Figure 27. Second set of results of the test experiment referred to in Figure 25. Accuracy in the reconstruction of a variable frequency "bar-target" phase distribution is demonstrated.

holography in conjunction with subsequent interferometry.

As is evident from the experimental results, our method

stands out as a very promising one.   In our future work we

shall fully exploit the tremendous flexibility and versatility

of our method to study some actual pulse laser beam parameters

including the mutual intensity function.

REFERENCES

1. Mehta, C.L., "Determination of Spectral Profiles from Correlation Measurements", Nuovo Cimento, 36, 202-205 (1965).

2. Hariharan, P., & Sen, D., "Effects of Partial Coherence in Two-Beam Interference", JOSA 51, 1307 (1961).

3. Leith, E.N. and Upatnieks, J., "Reconstructed Wavefronts and Communication Theory", JOSA 52, 1123 (1962).

4. Korobkin, V.V., and Leontovich, A.J., "Coherence and Time Scanning of the Emission Spectrum of a Ruby Laser", Sov. Phys. JETP 17, 1242-45 (1963).

5. Bondarenko, N.G., Eremina, I.V., and Talanov, V.I., "The Phase Structure of the Output Beam of a Ruby Laser", JETP 19, 1016 (1964).

6. Davis, L.W., "Interferometric Investigation of the Wavefront of Laser Beams", Appl. Phys. Letts., 10, 301 (1967).

7. Miyamoto, T., and Yasuura, K., "Measurement of the Beam Parameters of a Laser Beam and Its Diffraction Field, Using a Hologram", Appl. Opt. 10, 161 (1971).

8. Cathey, W.T., Holography: State of the Art Review 1969, p. 96, Optosonic Press. "Local Reference Beam Generation for Holography", Patent application Dec. 8, 1965; Patent granted Dec. 10, 1968.

9. Rosen, L., and Clark, W., "Film Plane Holograms Without External Source Reference Beam", Appl. Phys. Letts. 10, 140 (1967).

10. Caulfield, H.J., Harris, J.L., and Hemstreet, H.W. Jr., "Local Reference Beam Generation in Holography", Proc. IEEE 55, 1758 (1967).

11. Caulfield, H.J., "Information Retrieval from Local Reference Beam Holograms", Phys. Letts. 27A, 319 (1968).

12. Caulfield, H.J., "Local Reference Beam Holography", Laser Focus, p. 21, November 1967.

13. Lurie, M., "Fourier Transform Holograms with Partially Coherent Light: Holographic Measurement of Spatial Coherence", JOSA <u>58</u>, 614 (1968).

14. Murata, K., Asakura, T., and Fujiwara, H., "Effects of Spatial Coherence on Holography", Optica Acta <u>17</u>, 5 (1970) (First presented at the Symposium on Application of Coherent Light, Florence, 1968).

15. Fujiwara, H., Asakura, T., Murata, K., "Some Effects of Spatial and Temporal Coherence in Holography", Optica Acta <u>17</u>, 823 (1970).

16. Ross, I.N., "Holographic Measurement of Coherence" paper 2-4, "Application of Holography": Proceedings of the Internatnl. Symposium of Holography 1970 , Besançon, France; eds. Vienot, Bulabois; Pasteur.

17. Aleksoff, C.C., "Holographic Determination of Spatial Coherence", Paper presented at the 1970 Spring Meeting of the Optical Society of America, JOSA <u>60</u>, 74 (1970).

18. Aleksoff, C.C., "Holographic Analysis and Display of Laser Modes", JOSA <u>61</u>, 1426 (1971).

19. Brandt, G.B., "Image Plane Holography", Appl. Opt. <u>8</u>, 1421 (1969).

C. TWO SCALAR REPRESENTATIONS USEFUL IN LASER COHERENCE STUDIES*

Anthony J. Devaney

1. Representation of the Electromagnetic Field in Terms of Two Scalar Fields

The problem of determining the coherence properties
of the light field radiated by a laser is ultimately
a problem of electromagnetism. In particular, taking
the output mirror of the laser to lie in the plane $z = 0$
with the propagation being into the half-space $z > 0$,
we must solve the homogeneous Maxwell equations

$$(34a) \quad \nabla \cdot \underline{E}(r,t) = 0 \,,$$

$$(34b) \quad \nabla \cdot \underline{B}(r,t) = 0 \,,$$

$$(34c) \quad \nabla \times \underline{E}(r,t) + \frac{1}{c}\frac{\partial}{\partial t}\underline{B}(r,t) = 0 \,,$$

$$(34d) \quad \nabla \times \underline{B}(r,t) - \frac{1}{c}\frac{\partial}{\partial t}\underline{E}(r,t) = 0 \,,$$

subject to the boundary condition that the electric
and magnetic fields $\underline{E}(r,t)$ and $\underline{B}(r,t)$ be outgoing as
$r \to \infty$ (i.e., the electromagnetic field should obey
Sommerfeld's radiation condition at infinity), and
reduce to specified values on the boundary plane $z = 0$.

The description of the optical field in terms of the
Maxwell equations is inconvenient because of the vector

---

* The work reported in this section is based in part
  on a portion of the doctoral thesis of A.J. Devaney.

character of the electromagnetic field amplitudes
$\underline{E}(r,t)$ and $\underline{B}(r,t)$. For this reason, a great deal
of effort has been expended, in the past, to transform
the electromagnetic field problem into a problem in-
volving scalar fields. The most notable successes
in this direction are due to Whittaker (1903) and to
Debye (1909). (See also Green and Wolf (1953) and
(1959)). Whittaker showed that the electromagnetic
field can be represented in terms of two scalar poten-
tials $\alpha_1(r,t)$ and $\alpha_2(r,t)$ (called "Whittaker potentials")
in the following manner:

(35a) $\underline{E}(r,t) = \nabla \times \left[\nabla \times \hat{\underline{z}} \, \alpha_1(r,t) \right] - \frac{1}{c} \nabla \times \hat{\underline{z}} \frac{\partial}{\partial t} \alpha_2(r,t)$,

(35b) $\underline{B}(r,t) = \frac{1}{c} \nabla \times \hat{\underline{z}} \frac{\partial}{\partial t} \alpha_1(r,t) + \nabla \times \left[\nabla \times \hat{\underline{z}} \, \alpha_2(r,t) \right]$,

where $\hat{\underline{z}}$ is a constant unit vector in the z direction,
and where the potentials satisfy homogeneous wave
equations in regions free of charge and current. Writing
(35a) and (35b) in Cartesian component form we find that

$$E_x(r,t) = \frac{\partial^2}{\partial x \partial z} \alpha_1(r,t) - \frac{1}{c} \frac{\partial^2}{\partial t \partial y} \alpha_2(r,t)$$

(36a) $\qquad E_y(r,t) = \frac{\partial^2}{\partial y \partial z} \alpha_1(r,t) + \frac{1}{c} \frac{\partial^2}{\partial t \partial x} \alpha_2(r,t)$

$$E_z(r,t) = -\left(\frac{\partial^2}{\partial x^2} + \frac{\partial^2}{\partial y^2} \right) \alpha_2(r,t)$$,

$$B_x(r,t) = \frac{1}{c} \frac{\partial^2}{\partial t \partial y} \alpha_1(r,t) + \frac{\partial^2}{\partial x \partial z} \alpha_2(r,t)$$

(36b)
$$B_y(r,t) = -\frac{1}{c} \frac{\partial^2}{\partial t \partial x} \alpha_1(r,t) + \frac{\partial^2}{\partial y \partial z} \alpha_2(r,t)$$

$$B_z(r,t) = -\left(\frac{\partial^2}{\partial x^2} + \frac{\partial^2}{\partial y^2} \right) \alpha_2(r,t)$$

where A_ξ stands for the component of the vector $\underline{A}$ in the ξ direction.

A very similar representation to the above Whittaker representation was first used by Debye (1909) in his studies on the radiation pressure exerted by electromagnetic fields on spheres of arbitrary material. Debye found that he could represent the field scattered by the spheres in terms of two scalar potentials $\Pi_1(r,t)$ and $\Pi_2(r,t)$ (called the Debye potentials) in the following manner:

(37a)
$$\underline{E}(r,t) = \nabla \times \left[\nabla \times r\, \Pi_1(r,t) \right] - \frac{1}{c} \nabla \times r \frac{\partial}{\partial t} \Pi_2(r,t)$$

(37b)
$$\underline{B}(r,t) = \frac{1}{c} \nabla \times r \frac{\partial}{\partial t} \Pi_1(r,t) + \nabla \times \left[\nabla \times r\, \Pi_2(r,t) \right]$$

where r is the radial vector in a spherical coordinate system, and where the potentials satisfy homogeneous wave equations. The components of the fields in a

spherical coordinate system are found to be

73

$$E_r(r,t) = -\frac{1}{r\sin\theta}\left[\frac{\partial}{\partial\theta}\left(\sin\theta\frac{\partial}{\partial\theta}\right) + \frac{1}{\sin\theta}\frac{\partial^2}{\partial\phi^2}\right]\Pi_1(r,t)$$

(38a)
$$E_\theta(r,t) = \frac{1}{r}\frac{\partial^2}{\partial\theta\partial r}r\Pi_1(r,t) - \frac{1}{\sin\theta}\frac{\partial^2}{\partial ct\partial\phi}\Pi_2(r,t)$$

$$E_\phi(r,t) = \frac{1}{r\sin\theta}\frac{\partial^2}{\partial\phi\partial r}r\Pi_1(r,t) + \frac{\partial^2}{\partial ct\partial\theta}\Pi_2(r,t)$$

$$B_r(r,t) = -\frac{1}{r\sin\theta}\left[\frac{\partial}{\partial\theta}\left(\sin\theta\frac{\partial}{\partial\theta}\right) + \frac{1}{\sin\theta}\frac{\partial^2}{\partial\phi^2}\right]\Pi_2(r,t)$$

(38b)
$$B_\theta(r,t) = \frac{1}{\sin\theta}\frac{\partial^2}{\partial ct\partial\phi}\Pi_1(r,t) + \frac{1}{r}\frac{\partial^2}{\partial\theta\partial r}r\Pi_2(r,t)$$

$$B_\phi(r,t) = -\frac{\partial^2}{\partial ct\partial\theta}\Pi_1(r,t) + \frac{1}{r\sin\theta}\frac{\partial^3}{\partial r\partial\phi}r\Pi_2(r,t) \quad .$$

The question arises as to whether the use of either, or perhaps both, of the above representations might be useful in the solution of the laser propagation problem. Consider first the Whittaker representation given in (35a) and(35b) . It is reasonable to approximate the field on the output mirror of the laser to be plane polarized and, consequently, one finds that

(39a)
$$\underline{E}(r,t) = -\frac{1}{c}\nabla\times\hat{\underline{z}}\frac{\partial}{\partial t}\alpha_2(r,t) \quad ,$$

(39b)
$$\underline{B}(r,t) = \nabla\times\left[\nabla\times\hat{\underline{z}}\,\alpha_2(r,t)\right] \quad .$$

Thus, we see that for the case of a plane polarized laser field,the field is completely described in terms of the single Whittaker potential $\alpha_2(r,t)$.

The Debye representation, on the other hand, although not simplifying to a single scalar represen-

tation for the case of plane polarized fields, has certain advantages over the Whittaker representation. In particular, if atmospheric effects are appreciable this representation can possibly be used to approximately determine the field which results after passing through the atmosphere. (c.f. Born and Wolf (1965) par. 13.5.1).

The Debye representation, in the form of a multipole expansion, also has the advantage of including all the statistics of the laser field in the multipole moments, which are <u>scalar random variables</u> for a statistical radiation field.

The above mentioned advantages of describing the electromagnetic field in terms of the Whittaker or Debye potentials indicates that such representations might be of immense value in the study of optical fields. This possibility is investigated in the following section where it is shown that by making use of these potential functions a great simplification in the description of the optical field results.

2.   Representation of the Field Coherence Tensors in Terms of a Potential Coherence Matrix

For the case of scalar fields (e.g. acoustic fields) one requires only a single scalar coherence function to describe most phenomena of physical interest. In the case of the electromagnetic field, however, one requires a number of coherence functions. For example,

75

to determine the averaged Poynting vector, i.e.,

$$(40) \quad <\underline{S}> = < \underline{E}^*(r,t) \times \underline{B}(r,t) >,$$

requires knowledge (except in certain special cases), of such quantities as $<E_y^*(r,t)\underline{B}_z(r,t)>$ etc. Another example is given by the field energy density

$$(41) \quad <\mathcal{H}> = < |\underline{E}(r,t)|^2 + |\underline{B}(r,t)|^2 >,$$

which requires knowledge of such quantities as $<E_x^*(r,t)E_x(r,t)>$.

Thus we see that one scalar coherence function is, in general, not sufficient to specify many quantities of interest in electromagnetic theory, and consequently in optics. For this reason one is led to use the "so called" <u>coherence tensors</u> of the electromagnetic field. (See for example Mehta and Wolf, 1963). These tensors are defined as follows:

ELECTRIC COHERENCE TENSOR

$$\Gamma^{\mathcal{E}}_{x_i x_j}(r_1, r_2, t_1, t_2) = < E^*_{x_i}(r_1, t_1) E_{x_j}(r_2, t_2) >,$$

MAGNETIC COHERENCE TENSOR

$$\Gamma^{\mathcal{B}}_{x_i x_j}(r_1, r_2, t_1, t_2) = < B^*_{x_i}(r_1, t_1) B_{x_j}(r_2, t_2) >,$$

CROSS COHERENCE TENSOR

$$\Gamma^{\mathcal{E}\mathcal{B}}_{x_i x_j}(r_1, r_2, t_1, t_2) = < E^*_{x_i}(r_1, t_1) B_{x_j}(r_2, t_2) >,$$

where $X_i = X$ if $i = 1$, y if $i = 2$ and z if $i = 3$, and where the bracket $< >$ is taken to mean an ensemble average.

In general there are six independent components each to the electric and magnetic coherence tensors and nine components to the cross coherence tensor. Thus one must (in general) deal with 21 coherence functions when working with the optical field!

Fortunately, by making use of the Whittaker or Debye representation of the electromagnetic field it is possible to express all 21 components of the field coherence tensors in terms of, what we shall refer to as a potential coherence matrix. There are two potential coherence matrices, one being derived from the Whittaker representation and the other from the Debye representation. In particular, we define the Whittaker coherence matrix as being

$$(42a) \quad \alpha_{ij}(r_1, r_2, t_1, t_2) = < \alpha_i^*(r_1, t_1) \alpha_j(r_2, t_2) > ,$$

and the Debye coherence matrix as

$$(42b) \quad \Pi_{ij}(r_1, r_2, t_1, t_2) = < \Pi_i^*(r_1, t_1) \Pi_j(r_2, t_2) > ,$$

where $i, j = (1, 2)$.

It is clear that the above matrices have only three independent elements. Furthermore, since, as already shown, the electromagnetic field amplitudes can be represented in terms of the Whittaker or Debye potentials, it follows

77

that the electromagnetic field coherence tensors can be completely represented in terms of either the Whittaker or Debye coherence matrix. In other words, knowledge of the three independent components of either of the potential coherence matrices is completely equivalent to knowing all 21 components of the field coherence tensors.

The determination of the components of the electromagnetic field tensors in terms of the potential coherence matrices is straightforward, but algebraically quite tedious. Figure 28 shows the various field coherence tensors in terms of the Whittaker coherence matrix for the case of a plane polarized laser field. Note that for this case $\alpha_{ij}(\underline{r}_1, \underline{r}_2, t_1, t_2)$ vanishes identically unless $i = j = 2$, and consequently all components of the coherence tensor are represented in terms of the single scalar coherence function $\alpha_{22}(\underline{r}_1, \underline{r}_2, t_1, t_2) = \Gamma_{12}(t_1, t_2)$.

3. Determination of the Whittaker Coherence Matrix from the Electromagnetic Field Tensors

It has been shown (see Fig. 28) that the field produced by a plane polarized laser is completely described by the scalar coherence function $\Gamma_{12}(t_1, t_2) = \alpha_{22}(\underline{r}_1, \underline{r}_2, t_1, t_2)$.[*] In this section we shall show how to calculate this coherence function from knowledge of certain elements of the electromagnetic coherence tensors on the output mirror

---

[*] When we say "completely describe" we mean that from $\Gamma_{12}(t_1, t_2)$ we can correctly predict the outcome of any "classical optical experiment" (eg, interference experiments). More general measurements, such as photon counting experiments, require knowledge of higher order coherence functions (c.f. Glauber, 1963).

ELECTRIC COHERENCE TENSOR

	X	Y	Z
X	$\dfrac{1}{c^2}\dfrac{\partial^2}{\partial y_1 \partial t_1}\dfrac{\partial^2}{\partial y_2 \partial t_2}\Gamma_{12}$	$-\dfrac{1}{c^2}\dfrac{\partial^2}{\partial y_1 \partial t_1}\dfrac{\partial^2}{\partial x_2 \partial t_2}\Gamma_{12}$	$\bigcirc$
Y	$-\dfrac{1}{c^2}\dfrac{\partial^2}{\partial x_1 \partial t_1}\dfrac{\partial^2}{\partial y_2 \partial t_2}\Gamma_{12}$	$\dfrac{1}{c^2}\dfrac{\partial^2}{\partial x_1 \partial t_1}\dfrac{\partial^2}{\partial x_2 \partial t_2}\Gamma_{12}$	$\bigcirc$
Z	$\bigcirc$	$\bigcirc$	$\bigcirc$

MAGNETIC COHERENCE TENSOR

	X	Y	Z
X	$\dfrac{\partial^2}{\partial x_1 \partial z_1}\dfrac{\partial^2}{\partial x_2 \partial z_2}\Gamma_{12}$	$\dfrac{\partial^2}{\partial x_1 \partial z_1}\dfrac{\partial^2}{\partial y_2 \partial z_2}\Gamma_{12}$	$-\dfrac{\partial^2}{\partial x_1 \partial z_1}\left(\dfrac{\partial^2}{\partial x_2^2}+\dfrac{\partial^2}{\partial y_2^2}\right)\Gamma_{12}$
Y	$\dfrac{\partial^2}{\partial y_1 \partial z_1}\dfrac{\partial^2}{\partial x_2 \partial z_2}\Gamma_{12}$	$\dfrac{\partial^2}{\partial y_1 \partial z_1}\dfrac{\partial^2}{\partial y_2 \partial z_2}\Gamma_{12}$	$-\dfrac{\partial^2}{\partial y_1 \partial z_1}\left(\dfrac{\partial^2}{\partial x_2^2}+\dfrac{\partial^2}{\partial y_2^2}\right)\Gamma_{12}$
Z	$-\left(\dfrac{\partial^2}{\partial x_1^2}+\dfrac{\partial^2}{\partial y_1^2}\right)\dfrac{\partial^2}{\partial x_2 \partial z_2}\Gamma_{12}$	$-\left(\dfrac{\partial^2}{\partial x_1^2}+\dfrac{\partial^2}{\partial y_1^2}\right)\dfrac{\partial^2}{\partial y_2 \partial z_2}\Gamma_{12}$	$\left(\dfrac{\partial^2}{\partial x_1^2}+\dfrac{\partial^2}{\partial y_1^2}\right)\left(\dfrac{\partial^2}{\partial x_2^2}+\dfrac{\partial^2}{\partial y_2^2}\right)\Gamma_{12}$

CROSS COHERENCE TENSOR

	X	Y	Z
X	$-\dfrac{1}{c}\dfrac{\partial^2}{\partial y_1 \partial t_1}\dfrac{\partial^2}{\partial x_2 \partial z_2}\Gamma_{12}$	$-\dfrac{1}{c}\dfrac{\partial^2}{\partial y_1 \partial t_1}\dfrac{\partial^2}{\partial y_2 \partial z_2}\Gamma_{12}$	$\dfrac{1}{c}\dfrac{\partial^2}{\partial y_1 \partial t_1}\left(\dfrac{\partial^2}{\partial x_2^2}+\dfrac{\partial^2}{\partial y_2^2}\right)\Gamma_{12}$
Y	$\dfrac{1}{c}\dfrac{\partial^2}{\partial x_1 \partial t_1}\dfrac{\partial^2}{\partial x_2 \partial z_2}\Gamma_{12}$	$\dfrac{1}{c}\dfrac{\partial^2}{\partial x_1 \partial t_1}\dfrac{\partial^2}{\partial y_2 \partial z_2}\Gamma_{12}$	$-\dfrac{1}{c}\dfrac{\partial^2}{\partial x_1 \partial t_1}\left(\dfrac{\partial^2}{\partial x_2^2}+\dfrac{\partial^2}{\partial y_2^2}\right)\Gamma_{12}$
Z	$\bigcirc$	$\bigcirc$	$\bigcirc$

Figure 28

Electromagnetic coherence tensors for a plane polarized
field in terms of the Whittaker Coherence Matrix.

79

In Figure 28, $\Gamma_{12} = \Gamma(r_1, r_2, t_1, t_2) = \langle \alpha_2^*(r_1,t_1) \alpha_2(r_2,t_2) \rangle$.
The entries are such that the rows correspond to the
first subscript and to the r_1, t_1 coordinate, while
the columns correspond to the second subscript and to
the r_2, t_2 coordinate. For example, the electric
coherence tensor is displayed as follows:

	X	Y	Z
X	$\Gamma_{xx}^{\mathcal{E}}(r_1,r_2,t_1,t_2)$	$\Gamma_{xy}^{\mathcal{E}}(r_1,r_2,t_1,t_2)$	$\Gamma_{xz}^{\mathcal{E}}(r_1,r_2,t_1,t_2)$
Y	$\Gamma_{yx}^{\mathcal{E}}(r_1,r_2,t_1,t_2)$	$\Gamma_{yy}^{\mathcal{E}}(r_1,r_2,t_1,t_2)$	$\Gamma_{yz}^{\mathcal{E}}(r_1,r_2,t_1,t_2)$
Z	$\Gamma_{zx}^{\mathcal{E}}(r_1,r_2,t_1,t_2)$	$\Gamma_{zy}^{\mathcal{E}}(r_1,r_2,t_1,t_2)$	$\Gamma_{zz}^{\mathcal{E}}(r_1,r_2,t_1,t_2)$

of the laser. We shall also give the procedure which must be used to determine the Whittaker coherence matrix from knowledge of the coherence tensors of an arbitrary field on the plane $z = 0$.

Consider first a general electromagnetic field which satisfies the Maxwell equations (1a)-(1d) and Sommerfeld's radiation condition at infinity. (e.g., the field produced by a laser radiating into the half-space $z > 0$). It is not difficult to show (c.f. Borgiotti, 1962) that the field (for $z \geq 0$) can be expressed in the form of an <u>angular spectrum expansion</u> as follows:

(43a) $\quad \underline{E}(r,t) = \frac{1}{(2\pi)^3} \int_0^\infty d\omega \int_{-\infty}^\infty dk_1 dk_2 \; \underset{\sim}{\underline{E}}(k_1, k_2, \omega) \, e^{i(\underline{k}_0 \cdot \underline{r} - \omega t)}$

(43b) $\quad \underline{B}(r,t) = \frac{1}{(2\pi)^3} \int_0^\infty d\omega \int_{-\infty}^\infty dk_1 dk_2 \; \underset{\sim}{\underline{B}}(k_1, k_2, \omega) \, e^{i(\underline{k}_0 \cdot \underline{r} - \omega t)}$

where

(43') $\quad \underline{k}_0 = k_1 \hat{x} + k_2 \hat{y} + \sqrt{(\omega/c)^2 - k_1^2 - k_2^2} \; \hat{z}$

and where $\underset{\sim}{\underline{E}}(k_1, k_2, \omega)$ and $\underset{\sim}{\underline{B}}(k_1, k_2, \omega)$ are the three-fold Fourier transforms of the electric and magnetic fields on the boundary plane $z = 0$. i.e.,

(44a) $\quad \underset{\sim}{\underline{E}}(k_1, k_2, \omega) = \int_{-\infty}^\infty dt\, dx\, dy \; \underline{E}(x, y, z=0, t)\, e^{-i(k_1 x + k_2 y - \omega t)}$

(44b) $\quad \underset{\sim}{\underline{B}}(k_1, k_2, \omega) = \int_{-\infty}^\infty dt\, dx\, dy \; \underline{B}(x, y, z=0, t)\, e^{-i(k_1 x + k_2 y - \omega t)}$.

81

Since (34a) and (34b) require the divergence of (43a) and (43b) to be zero, we conclude that

$$(45) \quad \underline{k}_0 \cdot \underset{\sim}{\underline{E}}(k_1, k_2, \omega) \equiv \underline{k}_0 \cdot \underset{\sim}{\underline{B}}(k_1, k_2, \omega) \equiv 0 \, ,$$

which allows us to decompose these vector fields as follows (c.f. Devaney, 1971, p.8):

$$(46a) \quad \underset{\sim}{\underline{E}}(k_1, k_2, \omega) = -\underline{k}_0 \times (\underline{k}_0 \times \hat{\underline{z}}) \underset{\sim}{\alpha}_1(k_1, k_2, \omega) - \frac{\omega}{c} \underline{k}_0 \times \hat{\underline{z}} \underset{\sim}{\alpha}_2(k_1, k_2, \omega) \, ,$$

$$(46b) \quad \underset{\sim}{\underline{B}}(k_1, k_2, \omega) = \frac{\omega}{c} \underline{k}_0 \times \hat{\underline{z}} \underset{\sim}{\alpha}_1(k_1, k_2, \omega) - \underline{k}_0 \times (\underline{k}_0 \times \hat{\underline{z}}) \underset{\sim}{\alpha}_2(k_1, k_2, \omega) \, .$$

$\underset{\sim}{\alpha}_1(k_1, k_2, \omega)$ and $\underset{\sim}{\alpha}_2(k_1, k_2, \omega)$ are recognized as being proportional to the projections of $\underset{\sim}{\underline{E}}(k_1, k_2, \omega)$ onto the orthogonal vectors $-\underline{k}_0 \times (\underline{k}_0 \times \hat{\underline{z}})$ and $-\frac{\omega}{c} \underline{k}_0 \times \hat{\underline{z}}$ respectively. In particular, we find from (46a) that

$$(47a) \quad \underset{\sim}{\alpha}_1(k_1, k_2, \omega) = \frac{\hat{\underline{z}} \cdot \underset{\sim}{\underline{E}}(k_1, k_2, \omega)}{k_1^2 + k_2^2} \, ,$$

$$(47b) \quad \underset{\sim}{\alpha}_2(k_1, k_2, \omega) = -\frac{(\underline{k}_0 \times \hat{\underline{z}}) \cdot \underset{\sim}{\underline{E}}(k_1, k_2, \omega)}{(\frac{\omega}{c})^2 (k_1^2 + k_2^2)} \, .$$

If we use (46a) and (46b) in (43a) and (43b) respectively, we obtain the Whittaker representation as given in (35a) and (35b). In particular, we find that

82

(48a) $\underline{E}(\underline{r},t) = \nabla \times \left[\nabla \times \hat{\underline{z}} \frac{1}{(2\pi)^3} \int_0^\infty d\omega \int_{-\infty}^\infty dk_1 dk_2 \, \overset{\vee}{\alpha}_1(k_1,k_2,\omega) e^{i(\underline{k}_0 \cdot \underline{r} - \omega t)} \right] +$

$\qquad - \frac{1}{c} \nabla \times \hat{\underline{z}} \frac{d}{dt} \left[\frac{1}{(2\pi)^3} \int_0^\infty d\omega \int_{-\infty}^\infty dk_1 dk_2 \, \overset{\vee}{\alpha}_2(k_1,k_2,\omega) e^{i(\underline{k}_0 \cdot \underline{r} - \omega t)} \right],$

(48b) $\underline{B}(\underline{r},t) = \frac{1}{c} \nabla \times \hat{\underline{z}} \frac{d}{dt} \left[\frac{1}{(2\pi)^3} \int_0^\infty d\omega \int_{-\infty}^\infty dk_1 dk_2 \, \overset{\vee}{\alpha}_1(k_1,k_2,\omega) e^{i(\underline{k}_0 \cdot \underline{r} - \omega t)} \right] +$

$\qquad + \nabla \times \left[\nabla \times \hat{\underline{z}} \frac{1}{(2\pi)^3} \int_0^\infty d\omega \int_{-\infty}^\infty dk_1 dk_2 \, \overset{\vee}{\alpha}_2(k_1,k_2,\omega) e^{i(\underline{k}_0 \cdot \underline{r} - \omega t)} \right].$

From (48a) and (48b) we see that the Whittaker potentials are given, for all $z \geq 0$, by

(49a) $\alpha_1(\underline{r},t) = \frac{1}{(2\pi)^3} \int_0^\infty d\omega \int_{-\infty}^\infty dk_1 dk_2 \, \overset{\vee}{\alpha}_1(k_1,k_2,\omega) e^{i(\underline{k}_0 \cdot \underline{r} - \omega t)},$

(49b) $\alpha_2(\underline{r},t) = \frac{1}{(2\pi)^3} \int_0^\infty d\omega \int_{-\infty}^\infty dk_1 dk_2 \, \overset{\vee}{\alpha}_2(k_1,k_2,\omega) e^{i(\underline{k}_0 \cdot \underline{r} - \omega t)}.$

The Whittaker coherence matrix $\alpha_{ij}(\underline{r}_1,\underline{r}_2,t_1,t_2)$ is consequently given by (for z_1 and $z_2 \geq 0$),

(50a) $\alpha_{ij}(\underline{r}_1,\underline{r}_2,t_1,t_2) = \frac{1}{(2\pi)^6} \int_0^\infty d\omega \int_{-\infty}^\infty dk_1 dk_2 \int_0^\infty d\omega' \int_{-\infty}^\infty dk_1' dk_2' \, \overset{\sim}{\alpha}_{ij}(k_1,k_2,\omega,k_1',k_2',\omega').$

$\qquad \cdot e^{i(\underline{k}_0' \cdot \underline{r}_2 - \underline{k}_0^* \cdot \underline{r}_1 - \omega' t_2 + \omega t_1)},$

where

(50b) $\underline{k}_0 = k_1 \hat{x} + k_2 \hat{y} + \sqrt{(\omega/c)^2 - k_1^2 - k_2^2} \,\hat{\underline{z}},$

$\qquad \underline{k}_0' = k_1' \hat{x} + k_2' \hat{y} + \sqrt{(\omega/c)^2 - k_1'^2 - k_2'^2} \,\hat{\underline{z}},$

83

and where

(51) $\tilde{\alpha}_{ij}(k_1, k_2, \omega, k_1', k_2', \omega') = \langle \alpha_i^*(k_1, k_2, \omega) \alpha_j(k_1', k_2', \omega') \rangle$.

We thus see that, just as $\alpha_1(r, t)$ and $\alpha_2(r, t)$ are completely specified by knowing $\tilde{\alpha}_1(k_1, k_2, \omega)$ and $\tilde{\alpha}_2(k_1, k_2, \omega)$, the Whittaker coherence matrix is completely specified by $\tilde{\alpha}_{ij}(k_1, k_2, \omega, k_1', k_2', \omega')$. Furthermore, it is clear from (50) that $\tilde{\alpha}_{ij}$ is given by

(52) $\tilde{\alpha}_{ij}(k_1, k_2, \omega, k_1', k_2', \omega') = \int_{-\infty}^{\infty} dt_1 dx_1 dy_1 \int_{-\infty}^{\infty} dt_2 dx_2 dy_2 \, \alpha_{ij}(r_1, r_2, t_1, t_2) \Big|_{z_1 = z_2 = 0} \cdot$

$\cdot e^{-i(k_1' x_2 + k_2' y_2 - \omega' t_2 - k_1 x_1 - k_2 y_1 + \omega t_1)}$,

or, in other words, $\underline{\tilde{\alpha}_{ij}(k_1, k_2, \omega, k_1', k_2', \omega')}$ is simply the six-fold Fourier transform of the Whittaker coherence matrix on the plane $z_1 = z_2 = 0$. Since, for a general field the field coherence tensors $\Gamma_{x_i x_j}^{\mathcal{E}}$, $\Gamma_{x_i x_j}^{\mathcal{B}}$ and $\Gamma_{x_i x_j}^{\mathcal{E}\mathcal{B}}$ can always be expressed in terms of the Whittaker coherence matrix in a linear manner, we conclude that by use of (52) we can determine $\tilde{\alpha}_{ij}$ and, consequently, $\alpha_{ij}(r_1, r_2, t_1, t_2)$ (for $z_1, z_2 \geq 0$) by knowing any of the field coherence tensors on the plane $z_1 = z_2 = 0$.

As an example, we shall determine $\alpha_{22}(r_1, r_2, t_1, t_2)$ for the case of a plane polarized optical field. For such a field all elements of the Whittaker coherence matrix vanish except $\alpha_{22}(r_1, r_2, t_1, t_2) = \Gamma_{11}(t_1 t_2)$. The various components of the field coherence tensors for this case

84

are given in Figure 28 in terms of Γ_{12} . From this figure we see that

$$(53) \quad \frac{1}{c} \frac{\partial^2}{\partial y_1 \partial t_1} \left(\frac{\partial^2}{\partial x_2^2} + \frac{\partial^2}{\partial y_2^2} \right) \Gamma_{12}(t_1, t_2) = \Gamma_{xz}^{EB}(r_1, r_2, t_1, t_2) =$$

$$= \left\langle E_x^*(r_1, t_1) B_z(r_2, t_2) \right\rangle .$$

We now perform a six-fold Fourier transform (on the plane $z_1 = z_2 = 0$) to both sides of (45) to obtain:

$$(54) \quad -\frac{\omega}{c} k_1 \left(k_1'^2 + k_2'^2 \right) \tilde{\alpha}_{22}(k_1, k_2, \omega, k_1', k_2', \omega') = \tilde{\Gamma}_{xz}^{EB}(k_1, k_2, \omega, k_1', k_2', \omega'),$$

where

$$(54') \quad \tilde{\Gamma}_{xz}^{EB}(k_1, k_2, \omega, k_1', k_2', \omega') = \int_{-\infty}^{\infty} dt_1 dx_1 dy_1 \int_{-\infty}^{\infty} dt_2 dx_2 dy_2 \, \Gamma_{xz}^{EB}(r_1, r_2, t_1, t_2) \Big|_{z_1 = z_2 = 0} e^{-i(k_1' x_2 + k_2' y_2 - \omega' t_2 - k_1 x_1 - k_2 y_1 + \omega t_1)}$$

(54) is immediately solved for $\tilde{\alpha}_{22}$ to give

$$(55) \quad \tilde{\alpha}_{22}(k_1, k_2, \omega, k_1', k_2', \omega') = - \frac{\tilde{\Gamma}_{xz}^{EB}(k_1, k_2, \omega, k_1', k_2', \omega')}{(\omega/c) k_1 \left(k_1'^2 + k_2'^2 \right)},$$

which when substituted into (50) gives

$$(56) \quad \Gamma_{12}(t_1, t_2) = -\frac{1}{(2\pi)^6} \int_0^\infty d\omega \int_{-\infty}^\infty dk_1 dk_2 \int_0^\infty d\omega' \int_{-\infty}^\infty dk_1' dk_2' \, \frac{\tilde{\Gamma}_{xz}^{EB}(k_1, k_2, \omega, k_1', k_2', \omega')}{(\omega/c) k_1 (k_1'^2 + k_2'^2)}.$$

$$\cdot \, e^{i(k_0' \cdot r_2 - k_0^* \cdot r_1 - \omega' t_2 + \omega t_1)}$$

85

From $\Gamma_{12}(t_1, t_2)$ as given in (56) we can calculate all the electromagnetic coherence tensors. For example, from Figure 28 we find that $\Gamma_{xx}^{B}(r_1, r_2, t_1, t_2)$ is given by

(57) $\quad \Gamma_{xx}^{B}(r_1, r_2, t_1, t_2) = \dfrac{\partial^2}{\partial x_1 \partial z_1} \dfrac{\partial^2}{\partial x_2 \partial z_2} \Gamma_{12}(t_1, t_2) = \dfrac{1}{(2\pi)^6} \int\limits_0^\infty d\omega \int\limits_{-\infty}^\infty dk_1 dk_2 \cdot$

$\cdot \int\limits_0^\infty d\omega' \int\limits_{-\infty}^\infty dk_1' dk_2' \left[\dfrac{k_1' k_3' k_3^*}{\omega/c \, (k_1'^2 + k_2'^2)} \right] \widetilde{\Gamma}_{xz}^{EB}(k_1, k_2, \omega, k_1', k_2', \omega') e^{i(k_3' r_2 - k_3^* r_1 - \omega' t_2 + \omega t_1)}$

where

(57') $\qquad k_3 = \sqrt{(\omega/c)^2 - k_1^2 - k_2^2}$,

$\qquad\qquad k_3' = \sqrt{(\omega'/c)^2 - k_1'^2 - k_2'^2}$.

The advantages of using the Whittaker coherence matrix rather than working directly with the electro-magnetic field tensors is dramatically displayed above. In particular, only one measurement is needed to determine $\Gamma_{12}(t_1, t_2)$ (e.g., the measurement of $\Gamma_{xz}^{EB}(r_1, r_2, t_1, t_2)$ on the plane $z_1 = z_2 = 0$) which, in turn, completely specifies all of the electromagnetic field tensors and consequently is sufficient to completely predict the outcome of any classical optical experiment.

4. Summary and Conclusions

We have, in the previous pages, developed a theory

86

of coherence for general (stationary or non-stationary) optical fields which uses only three scalar coherence functions. These three coherence functions can be taken to be the three independent elements of either the Whittaker or Debye coherence matrices. From them, all of the electromagnetic coherence tensors can be calculated and, consequently, they are sufficient to completely predict the outcome of any classical experiment in optics.

We have also described a procedure which can be used to determine the Whittaker coherence matrix from knowledge of certain elements of the electromagnetic coherence tensors on the plane $z = 0$ (e.g., the output mirror of the laser). For the special case of a plane polarized light field we have shown that all elements of the Whittaker coherence matrix vanish except for $\alpha_{22}(r_1, r_2, t_1, t_2) = \Gamma_{12}(t_1, t_2)$, and that this function can be completely determined <u>from any element of any of the electromagnetic coherence tensors on the plane $z_1 = z_2 = 0$.</u> Consequently, for such a field only one coherence function is completely sufficient to predict the outcome of any classical experiment in optics.

From the previous pages it is clear that the use of the Whittaker coherence matrix offers a great deal of simplification for describing the coherence properties of laser fields. However, the Debye coherence matrix might also be of immense value in describing such fields. Unfortunately, the Debye potentials and, consequently, the Debye coherence matrix can not be determined from the electromagnetic field amplitudes in a manner as straightforward as that used to determine the Whittaker potentials (c.f. Devaney, 1971, Chap. IV). Consequently, further work of an analytical nature will be required

87

to fully exploit the Debye coherence matrix.

REFERENCES

1   Whittaker, E.T., "On an Expression of the Electro-
magnetic Field due to Electrons by Means of two Scalar
Potential Functions", Proc. London Math. Soc., <u>1</u>
(1903).

2.   Debye, P.,"Der Lichtdruck auf Kugeln von beliebigem Material",
Ann. d. Physik (4), <u>30</u>, 57, (1909).

3.   Borgiotti, G., "A General Way of Representing the
Electromagnetic Field", Alta Frequenza, <u>31</u>, n.5
(1962).

4.   Born, M. and Wolf, E., <u>Principles of Optics</u>,
Pergamon Press, third edition (1965).

5.   Devaney, A.J., " A New Theory of the Debye Repre-
sentation of Classical and Quantized Electromagnetic
Fields", Ph.D. thesis, The Institute of Optics,
Univ. of Roch. (1971).

6.   Glauber, R.J., "The Quantum Theory of Optical Coherence",
Phys. Rev. <u>130</u> (1963).

7.   Mehta, C.L., and Wolf, E., "Coherence Properties
of Blackbody Radiation. I. Correlation Tensors of
the Classical Field", Phys. Rev., <u>134</u> (1964).

8.   Green, H.S., and Wolf E., "A Scalar Representation
of Electromagnetic Fields", Proc. Phys. Soc.,
LXVI (1953).

9.   Green, H.S. and Wolf, E., " A Scalar Representation
of Electromagnetic Fields: II", Proc. Phys. Soc.,
LXXIV (1959).

THE DESIGN OF EFFICIENT SOLID STATE LASER SYSTEMS WITH HIGH ENERGY POWER AND LOW BEAM DIVERGENCE

M. Hercher

A. ENLARGING THE TEM$_{OO}$ MODE SIZE OF A SOLID LASER

1. INTRODUCTION

A wide variety of applications call for the output of a solid laser system to be in the form of the lowest order transverse mode (TEM$_{OO}$). A number of workers have successfully obtained this mode selection using various techniques. In almost all cases the spot size ($2w_o$) of the TEM$_{OO}$ mode (defined at the $1/e^2$ points of the Gaussian intensity distribution) has been on the order of 1 to 1.5 mm within the laser rod. Often a carefully placed aperture of this diameter within the laser resonator is sufficient to eliminate the unwanted modes. We describe here a simple technique for enlarging the spot size of the TEM$_{OO}$ mode in a solid laser system, thereby increasing the TEM$_{OO}$ power available from typical laser rods. We also show that the spot size can be made independent of small changes in the optical power of the laser rod.

2. REVIEW OF THE GEOMETRICAL MODEL FOR MODE PROPAGATION

P. Laures[1] has shown that a simple geometrical construction can be used to design and analyze optical resonators in terms of their TEM$_{OO}$ modes. This geometrical construction is entirely equivalent to the mode propagation equations of Boyd and Kogelnik[2], but has the advantage of allowing an immediate visualization of the mode propagation. The geometrical construction thus has distinct advantages in designing complex resonators. Following is a brief but fairly complete summary of the technique -- stated without proof, for which the

reader is referred to reference 1.

Consider an optical resonator comprised of mirrors M_1 and M_2 with centers at O_1 and O_2 (fig. 29). Circles C_1 and C_2 are drawn on diameters $M_1 O_1$ and $M_2 O_2$ respectively. The resonator is stable only if circles C_1 and C_2 intersect. Assuming a stable resonator, let the circles intersect at two points F. The distance b between the two points F is the length of the equivalent confocal resonator for the cavity in question, and the line FF intersects the axis at the beam waist of the resonator. The location of the confocal foci F completely determines the propagation of the TEM_{oo} mode both inside and outside the resonator. The angle θ at which the circles C_1 and C_2 intersect can be shown to be equal to 2ϕ, where ϕ is the angle which appears in the expression for the resonant frequencies of the resonator:

$$\text{Resonant frequency } \nu_{mnq} = \frac{c}{2L}[q + \frac{1}{\pi}(1 + m + n)\phi]$$

$$\text{where } \phi = \cos^{-1}[(1 - \frac{L}{R_1})(1 - \frac{L}{R_2})]^{1/2}.$$

In this expression m and n are the transverse mode numbers, q is the axial mode number, R_1 and R_2 are the radii of curvature of M_1 and M_2 respectively, and L is the separation between M_1 and M_2.

Given the points F, referred to as the confocal foci of the resonator, the spot size and center of curvature of the TEM_{oo} mode at any point P along the resonator axis can be found as follows (fig. 30).

(1) Draw a circle C_3 through one point F and tangent to the axis at P. The diameter D(P) of this circle is related to the spot size at P, w(P) by:

$$w(P) = [\lambda d/\pi]^{1/2}$$

92
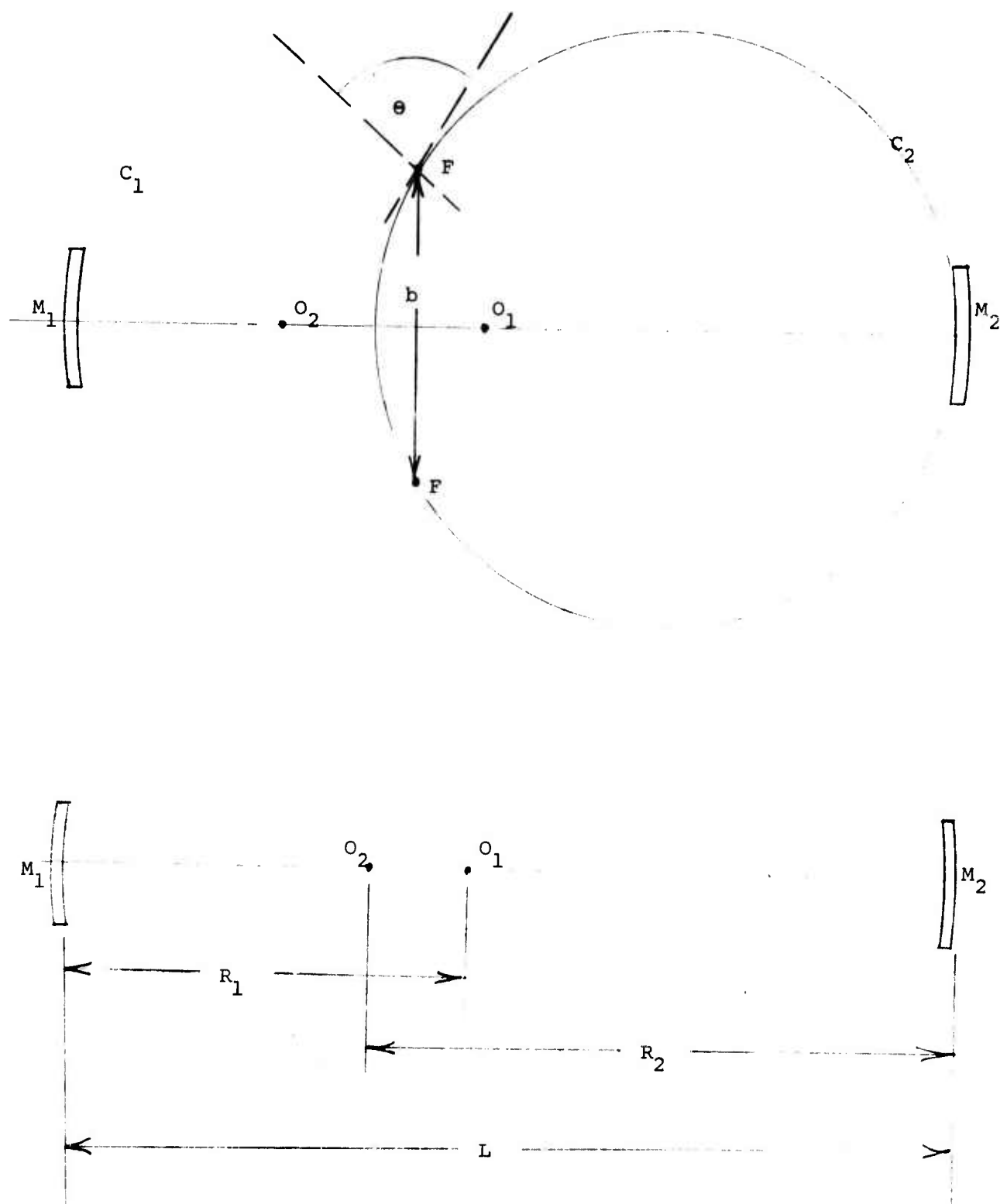
Figure 29

Geometrical construction for resonator analysis.

93

$$D(P) = \frac{\pi w^2(P)}{\lambda}$$

O(P)

Center of curvature
of wavefront at P

P

• F
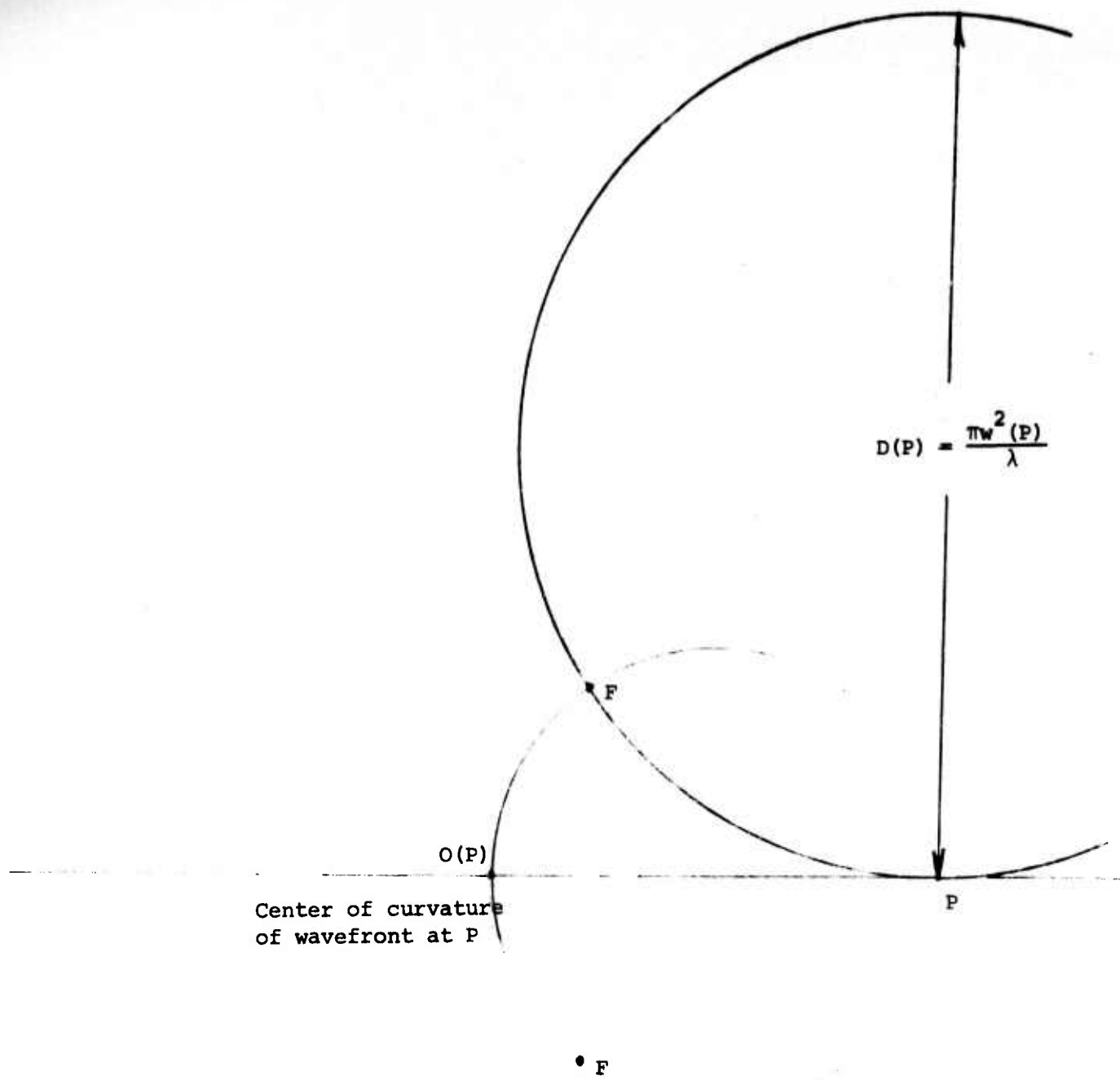
Figure 30

Geometrical construction for spot size determination.

(2) Draw a circle C_4 through both points F and P. This
circle intersects the axis at O(P), the center of
curvature of the TEM$_{00}$ wavefront at P.

If a lens of focal length f is located at an axial point
P (fig. 31), it will transform the center of curvature of the
wavefront from O to O' according to the usual simple lens
law [$1/f = (1/s) + (1/s')$]. If a circle C_5 is now drawn on
a diameter O'P, it will intersect the circle C_3 (which is
the construction circle for determining the spot size at P--
which has the same value on both sides of the lens) at a point
F', which is one of the pair of new confocal foci for construc-
ting the propagation of the TEM$_{00}$ mode to the right of the lens
at P. From another point of view, the lens at P can be thought
of as being the element which mode-matches resonators whose
confocal foci are at F and F' respectively.

3. DESIGN OF A SOLID LASER RESONATOR FOR A GIVEN SPOT SIZE

We will pose the problem of designing a resonator for
use with a solid laser which has a given spot size 2w at the
laser rod, and which is highly stable and relatively compact.
For the sake of simplicity we will assume that one of the
resonator mirrors, M_1, is plane and that the laser rod is
immediately adjacent to this mirror. Since M_1 is plane,
the confocal foci F lie in the plane of the mirror (fig. 32).
The given spot size, 2w, defines the diameter D of the construc-
tion circle C_3:

$$D = \pi w^2 / \lambda.$$

Now, as will be apparent shortly, in order to obtain a large
spot size at M_1 with a reasonably short resonator, the laser
rod should act as a lens (or a lens should be put into the

95
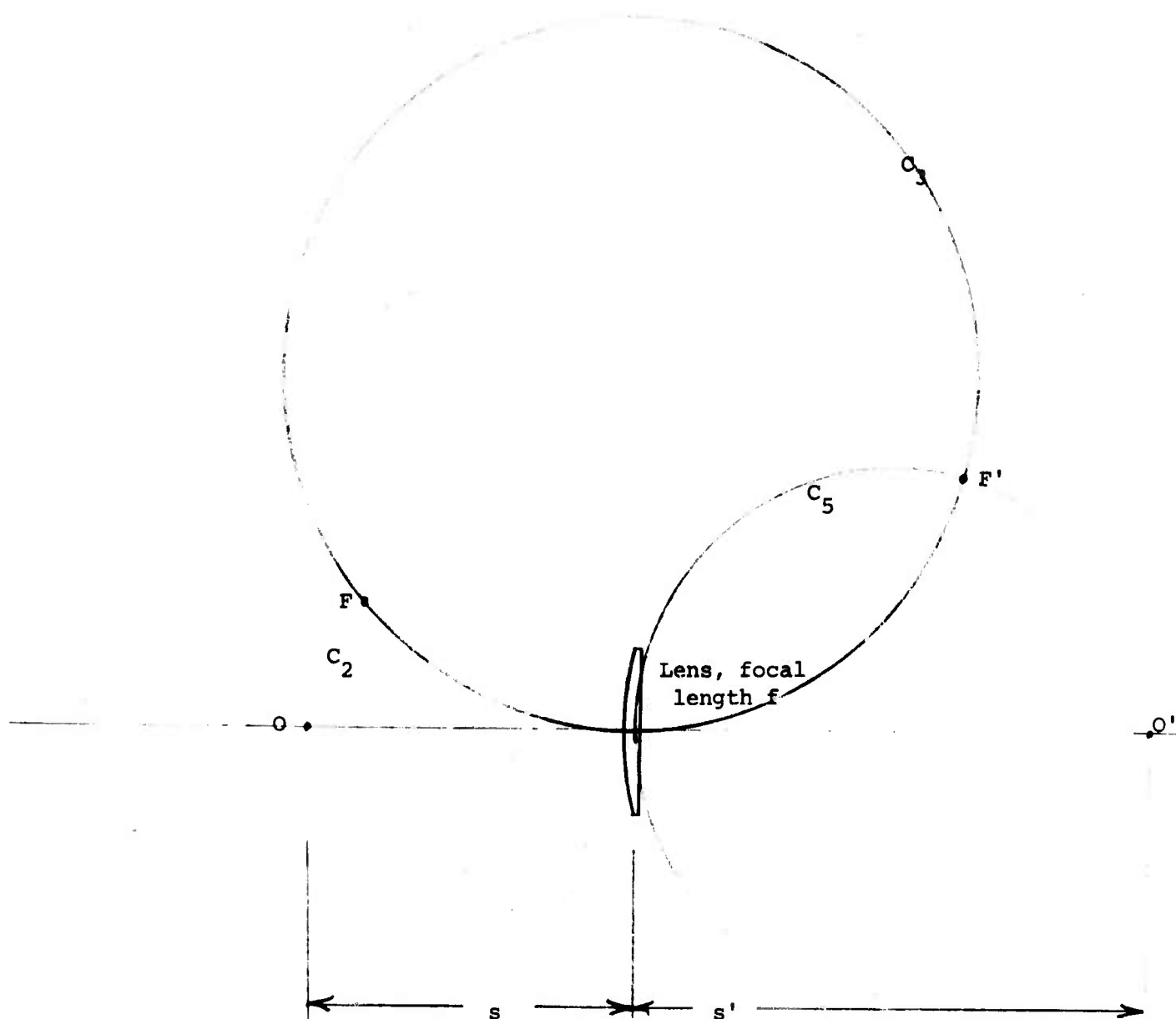
Figure 31

Transformation of confocal foci by a lens.
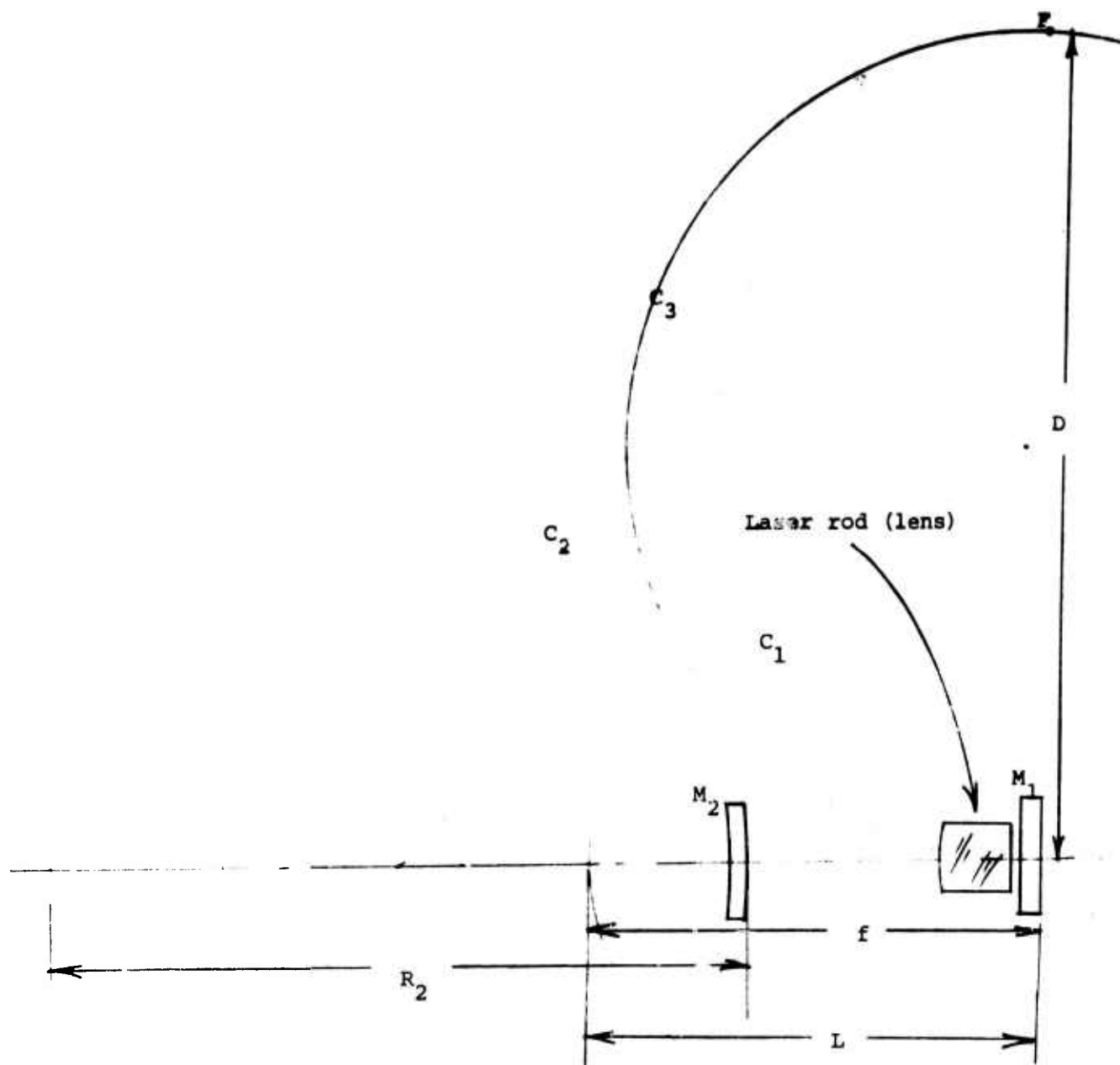
Figure 32

Design of a solid laser resonator for a given spot size.

resonator). Considering the relative scale of the resonator and laser rod, the latter can safely be treated as a thin lens immediately adjacent to the mirror M_1. Because M_1 is plane, the radius of curvature of the TEM_{00} wavefront just to the right of the lens is infinite. Thus the radius of curvature of the wavefront just to the left of the lens is equal to the focal length of the lens, f. We can now draw a circle C_1 with diameter f, as shown in fig. 32. This circle will intersect C_3 in two points F', which are the confocal foci for the resonator on the left of the lens. The final resonator component is the second mirror, M_2. Its construction circle, C_2, having a diameter R_2 equal to the radius of curvature of M_2, must intersect C_1 at F' in order for the resonator to define the desired spot size at M_1. To keep the resonator as short as possible it is clear that M_2 should be a convex mirror.

It should be clear from figure 32 that the relative stability of the resonator (qualitatively defined as the relative insensitivity of its mode structure to small changes in the positions of the mirrors) can be related to the angle θ at which the circles C_1 and C_2 intersect (see fig. 31). When θ approaches 0 or π the resonator becomes relatively unstable and difficult to align, and when θ is close to $\pi/2$, the resonator is highly stable.

An optimum design would thus ensure that C_1 and C_2 intersected at right angles and defined the desired spot size. It is easy to show that these conditions are satisfied (for given $D = \pi w^2/\lambda$ and f) when the radius of curvature of M_2 is given by:

$$R_2 = \frac{2\,D\,f^2}{D^2 - f^2} \quad .$$

The length of the resonator, L (assuming M_2 to be convex) is then given by:

$$L = \frac{R_2}{2} \left[\frac{D - f}{f}\right] .$$

This type of resonator automatically ensures that the spot size at M_1 will be, to first order, insensitive to small changes in the focal length of the laser rod. (This can be seen by referring to fig. 32 and noting that a change in the diameter of circle C_1 will cause F' to move in such a way that it continues to define the same circle C_3, which determines the spot size at M_1.) This feature is particularly useful in the case of glass or crystal lasers, which tend to become weak positive lenses due to thermal effects during optical pumping.

We have found that a Nd:glass laser rod which is 5 to 10 cm long typically acquires an optical power of +0.2 diopters when it is optically pumped to obtain laser emission; i.e. it becomes a weak positive lens with a focal length of 5 meters (ruby lasers behave in much the same way). If we calculate the TEM_{oo} spot size for a Nd:glass laser assuming that the laser rod has a 5 meter focal length and that the resonator is comprised of two plane mirrors 50 cm apart, we find that the spot size, 2w, is 1.4 mm. This number is approximately proportional to the fourth root of the focal length of the laser rod and the mirror separation, and is in good agreement with experimental results. By properly designing a resonator, as outlined above, the spot size in the laser rod can be substantially increased. In the example given below, a resonator is designed for a TEM_{oo} spot size of 3 mm. This would increase the TEM_{oo} mode volume and power by a factor of 4.6 over that obtained from a typical plane mirror resonator.

a. Example: Design of a Resonator to Give a 3mm Spot Size
with a Nd:glass Laser

To illustrate the design procedure outlined above, we
describe here a resonator which gives a 3 mm spot size (2w)
with a laser operating at a wavelength of 1 micron. The
diameter of circle C_3 (fig.32) is

$$D = \pi w^2 / \lambda = [(3.14) (0.15)^2 / (10^{-4})]cm = 7 \text{ meters}.$$

Clearly, if f and R_2 are much smaller than D (see fig.32).
then the spot size at M_1 will be unduly sensitive to the
exact locations of M_1 and M_2. On the other hand a 3 or 4
meter long resonator is an inconvenience in most laboratories.
A reasonable compromise is to set f at 2 meters, in which
case R_2 should be 1.24 meters, and the separation between M_1
and M_2 should be 1.56 meters. This resonator is drawn to
scale in fig. 33. In use it would, of course, require a
3 or 4 mm aperture at M_1 to restrict the output to a clean
TEM_{oo} mode. Note that a plane mirror at Q (fig.33) would
define the same TEM_{oo} mode but would be less stable and would
cause the spot size at M_1 to change with small changes in
the focal length of the laser rod.

A resonator of this type has been built and has produced
the enlarged TEM_{oo} spot size for which it was designed. These
experimental results will be presented in detail at a later
date.
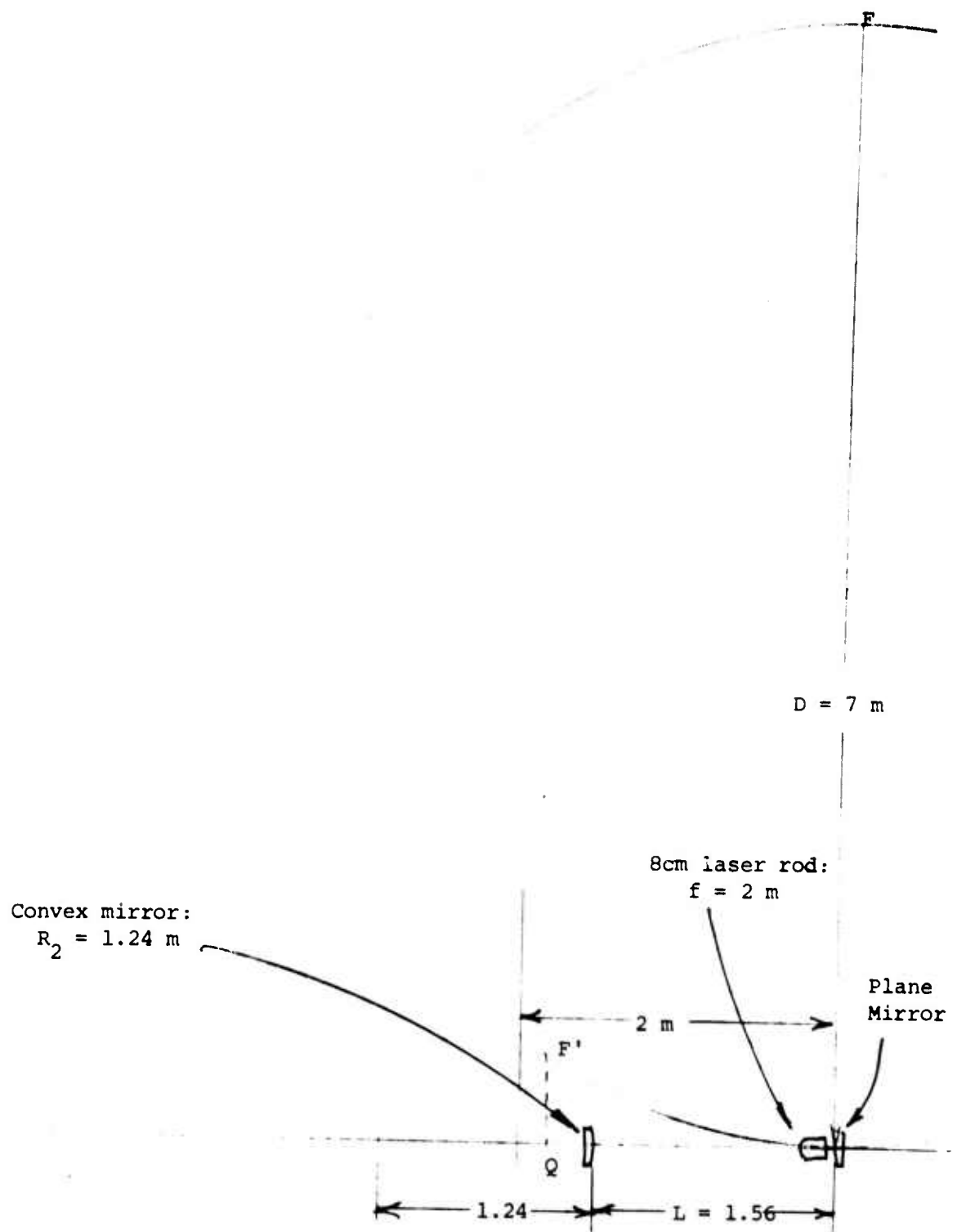
Figure 33

Nd:glass laser resonator designed for TEM_{oo} spot size $(2w_o)$ of 3mm.

REFERENCES

1. P. Laures, "Geometrical Approach to Gaussian Beam Propagation", Appl. Optics $\underline{6}$, 747 (1967).

2. G. D. Boyd and H. Kogelnik, "Generalized Confocal Resonator Theory", Bell Syst. Tech. J. $\underline{41}$, 1347 (1962).

B. CORRECTION OF THERMALLY INDUCED OPTICAL DISTORTION IN REPETITIVELY PUMPED RUBY LASER RODS

It is well-known that solid laser rods generally become optically distorted following a high energy pulse of optical excitation. This distortion is primarily due to the non-uniform cooling of the laser rod following excitation. This non-uniform cooling produces a temperature gradient which, in turn, produces localized variations in thermal expansion and thermal variation of refractive index. In the case of ruby, both of these effects are in the same direction and combine in such a way that an incident plane wave is distorted into an aberrated spherical wave after being transmitted by the laser rod.

There were three stages in our study of techniques to correct for this type of distortion in repetitively-pumped ruby laser rods:

(i) make a general study of the optical distortion in optically pumped ruby laser rods;

(ii) design and test a convenient technique for making a quantitative measure of such optical distortion; and

(iii) design and test techniques for optically correcting specific distortions.

The first two steps have been completed and we are currently working on the third. In addition, we have been working on a technique for modifying the cavity configuration of a laser oscillator so as to enlarge the TEM_{oo} mode volume and make the TEM_{oo} phase and amplitude distribution independent of small spherical distortions of the laser rod.

1. GENERAL STUDY OF OPTICAL DISTORTION IN OPTICALLY
   PUMPED LASER RODS

The problem at hand is to (1) determine the optical distortion which exists in a repetitively fired ruby laser rod at the time of firing, and (2) to correct for this distortion, and thereby improve the overall efficiency of the laser system, and considerably increase the degree of collimation of the output beam. We can very briefly summarize our current understanding of the problem as follows: Consider a 1 hertz repetition rate for the firing of a ruby laser system. After about 10 seconds, the system reaches a steady state in which the dynamics of the system repeat themselves each cycle. In examining a single cycle we will start just prior to the firing of the flashlamp(s). The laser rod begins to absorb energy more or less uniformly throughout its volume (the degree of uniformity depending on the pumping geometry: pumping systems involving diffuse reflectance of flashlamp light tend to produce more uniform pumping). This energy provides the gain of the laser, but a certain fraction of the energy inevitably is dissipated in the form of heat within the laser crystal. If the distribution of this energy is uniform throughout the volume of the laser, then the major thermal effect will be a thermal expansion which will certainly cause changes in the optical path length of the laser rod, but should produce no distortion.[1,2] Some distortion will occur between the onset of the flashlamp pulse and the firing of the laser

(an interval of approximately 0.5 - 1 msec), reflecting
non-uniformities in the distribution of the absorbed
flashlamp radiation, but this is small compared to other
sources of distortion and can be neglected in all but
the most sophisticated systems. It is immediately fol-
lowing the flashlamp pulse that most of the distortion
is produced. Lasers rods in systems of the type being
considered are typically cooled by the flow of water
over their cylinder surface. Thus the laser rod, whose
temperature may increase by tens of degrees Kelvin during
a single flashlamp pulse, is cooled in such a way as to
set up a strong radial temperature gradient. This produces
radial variations in the optical length of the laser rod
due both to thermal expansion and to thermal variations
in the refractive index of the laser rod. Moreover, the
radial temperature gradient causes a stress field which
in turn causes stress-induced birefringence. Fortunately,
this is not a serious problem in naturally birefringent
crystals since the stress-optic effects are resolved into
components lying along the natural crystal axes and thus
cause no depolarization of the laser light (this is not
the case in YAG, which is a cubic crystal).

In view of our understanding of the mechanism by
which thermal distortion is produced in ruby laser rods,
the distortion which we wish to correct for is very nearly
that which exists just prior to the firing of the flash-
lamp. We have considered a number of techniques for
measuring the distortion at various points in the cycle.
The interferometric technique, described in detail in

section 2, was judged most suitable for obtaining data from which optical correction plates could be made. A simpler but somewhat cruder method for measuring dynamic distortion is described below.

Fig. 34(a) shows a simple arrangement for measuring the attenuation of a collimated beam from a He-Ne laser, transmitted by the sample laser rod within a specified cone angle. This cone angle is determined by the pinhole size and the focal length of the lens L . The transmission of the beam within this cone angle can be monitored as a function of time following a single flash or during repetitive flashlamp pumping. Fig. 35 shows a typical oscillogram obtained in this way, and is annotated to indicate our interpretation of the data. Note that the thermal distortion of the laser rod persists for at least 10 sec, and is thus markedly more pronounced with repetitive pumping at 1 pulse/sec. Steady state distortion is reached after 10 to 15 seconds. The pumping geometries which we are examining are single and double elliptical cylinders with one and two flashlamps respectively. We are pumping at a level which provides a small signal gain of 15%/cm to 20%/cm. This measurement technique is being used mainly to provide preliminary data in preparation for more extensive measurements.

Fig. 34(b) shows a very simple arrangement which allows us to measure quantitatively the optical distortion of a laser rod at any point in the repetitive pumping cycle. The lens+pinhole combination acts as a filter which transmits wavefronts whose centers of curvature lie within

106

Figure 34. a) Measurement of beam transmission in a sample laser rod within a specified cone angle.
b) Measurement of the optical distortion of a laser rod.

107
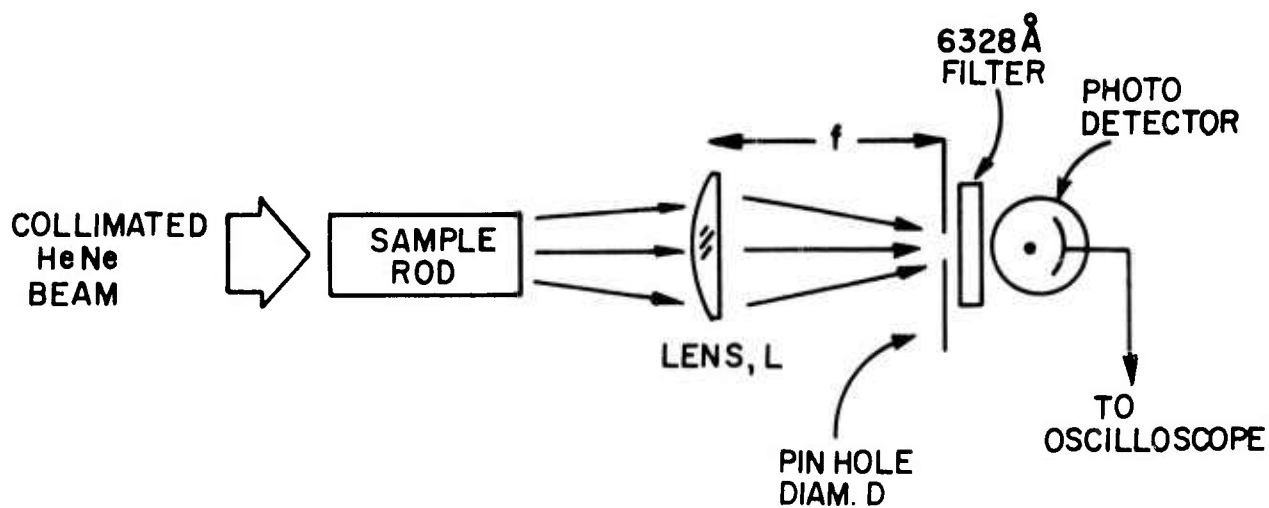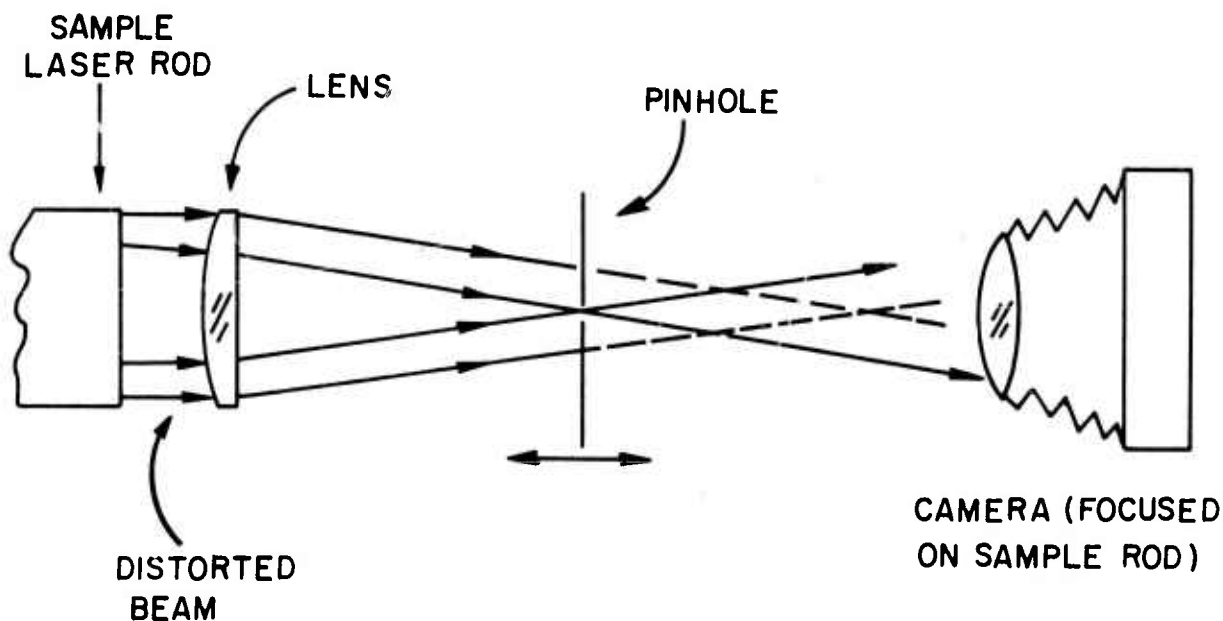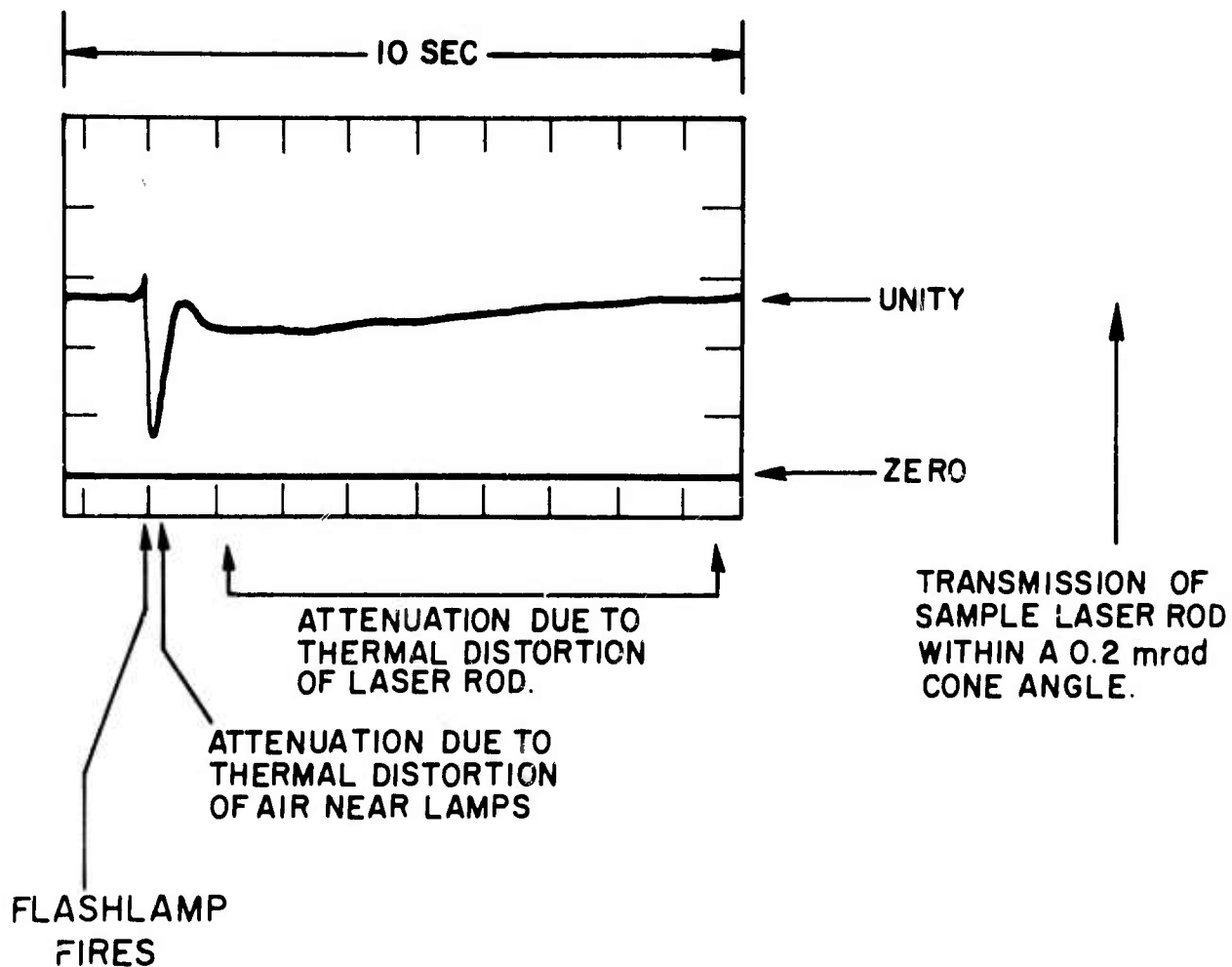
FIG. 35. TYPICAL DATA OBTAINED WITH THE ARRANGEMENT IN
FIGURE 34a .

108

the image of the pinhole which is formed by the lens. By
photographing the laser rod through such a filter it is
a simple matter to determine the type of distortion intro-
duced by the various zones in the aperture of the sample
laser rod. Using the data collected with the pinhole in
different positions, an aspheric correction plate can be
completely specified.

2. PROTOTYPE SYSTEM USED TO MEASURE OPTICAL DISTORTION
   IN RUBY LASER RODS

In order to evaluate the exact shape of an incident
plane wave transmitted by the ruby laser rod, the entire
laser head was placed in one arm of a Mach-Zehnder inter-
ferometer. A diagram of the interferometer as it was
set up in the laboratory is shown in fig. 36. The inter-
ferometer is a single pass

109
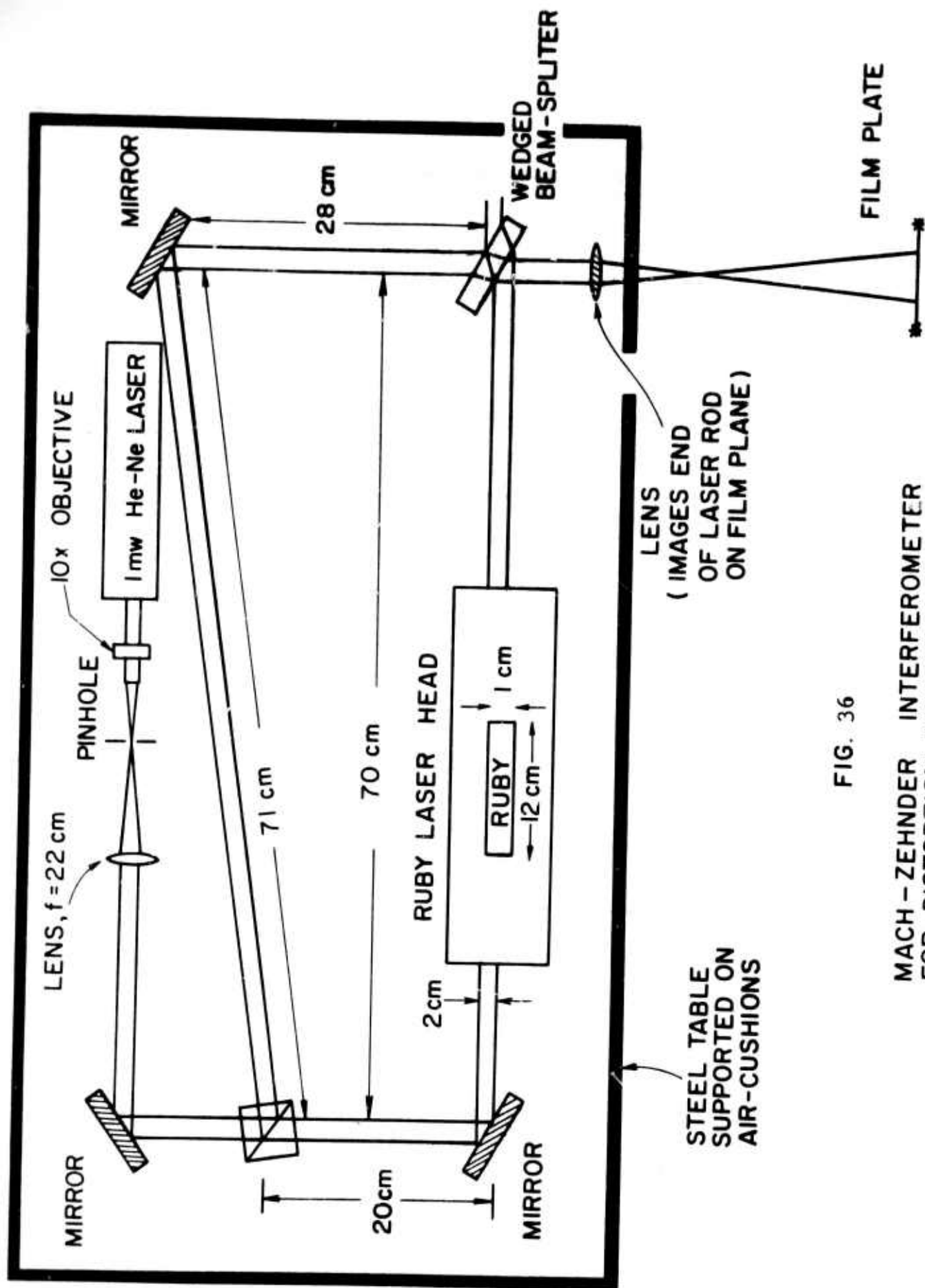
FIG. 36

MACH – ZEHNDER INTERFEROMETER
FOR DISTORTION MEASURMENT

110

instrument, so that fringes were formed for $(n-1)L = m\lambda$, m an integer (n is the refractive index of the laser rod and L is its length). The ruby itself did not act as a laser since the laser head was placed in the interferometer without the mirrors necessary for laser emission.

The entire steel baseplate rested on inner-tube-type air cushions, and was essentially equivalent to a 24" x 48" standard Gaertner optical table (without rails). This vibration isolation was essential since our laboratory suffers from severe floor vibrations. Even in a more quiet environment it would probably be desirable to use this type of vibration isolation since the laser support equipment itself (e.g. water pump(s), capacitor bank, inductances, heavy relays, etc.) is a source of significant vibrations. The air-cushioned table worked well and improved fringe stability very markedly. However, even with this degree of vibration isolation there were still some problems to solve. Since the laser head was rigidly fixed to the base plate, small oscillations -- arising from the water-cooling system and the firing of the flashlamp-- were transmitted to the table via the laser head. By using a buffer tank in the water flow system, and by mounting the interferometer components more securely, these residual vibrations could be suppressed.

Air currents in the room caused some wavering of the fringes and the light path in the interferometer was long enough for small temperature fluctuations to have some effect on the interferograms. This was not particularly serious (particularly since we would ultimately use a short exposure time), but was minimized by enclosing the entire set-up in a wooden frame with black cloth sides and top.

It is worth remarking at this point that on many occasions we noticed the susceptibility of mirror mounts to be set into oscillation when the laser flashlamp was fired; if a laser

111

rod is to be optically corrected to within a wavelength or
so, it is obviously necessary to make sure that the laser
cavity mirrors are aligned and stationary to within a comparable
tolerance.

As indicated in figure 36, the lengths of the optical paths
in the two arms of the interferometer were made equal; i.e.
there was compensation for the length of high index ruby in
one arm. In this way the interferogram fringe visibility
was constant in spite of changes in the detailed spectrum of
the helium-neon laser. A linear polarizer, aligned with the
polarization of the ruby laser output, was used in front of
the camera to assure the selection of the proper polarization
from the helium-neon laser.

After initial exposure calibration using black and white
film in a 35 mm camera, one roll (100 feet) of Ektachrome
16 mm film was exposed at two different light levels (color
film was used because it can be more quickly and conveniently
processed commercially). A variety of sequences were photo-
graphed using different pulse rep rates and flashlamp voltages.
While the quality of the movie film was not as high as we had
anticipated, the development of the optical distortion could
be clearly seen. Due to the relatively slow shutter speed
(1/150 sec) at 64 fps, the fringe patterns were washed out
in the first few frames following each flash of the lamps.
Figure 37 shows a number of frames obtained in these sequences.
Fig. 37a, b and c show the interferograms obtained before the
first flashlamp pulse, shortly after the first pulse, and
just prior to the second pulse, respectively. Figure 37d,e
and f show the interferograms obtained just prior to flashlamp
pulses after the interferograms have reached a more or less
steady-state cycle. The distortions in these interferograms
are not very severe, but serve to illustrate the technique. In

112

(A) PRIOR TO FIRST PULSE

(B) 150 MILLISEC. AFTER
FIRST PULSE

(C) 100 MILLISEC. PRIOR TO
SECOND PULSE

INTERFEROGRAMS SHOWING
DISTORTION OF RUBY LASER
ROD DURING REPETATIVE PULSING
AT 1 PULSE PER SECOND

FIG. 37 -- Continued

(D) 100 MILLISEC. PRIOR TO THIRD PULSE

(E) 30 MILLISEC PRIOR TO FOURTH PULSE

(F) 50 MILLISEC. PRIOR TO FIFTH PULSE
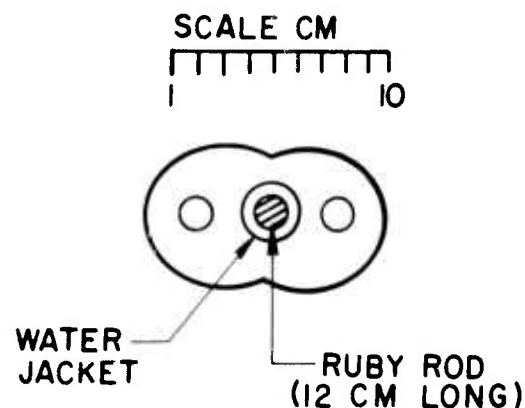
(G) PUMPING GEOMETRY
ENERGY TO LAMPS : 2400 JOULES/PULSE

SCALE CM

WATER JACKET

RUBY ROD (12 CM LONG)

INTERFEROGRAMS SHOWING DISTORTION OF RUBY LASER ROD DURING REPETIVE PULSING AT 1 PULSE PER SECOND

FIG. 37 -- Concluded

routine use a Polaroid camera with standard black and white film would be entirely adequate for obtaining the interferograms from which correction plates were to be designed.

3. PRODUCTION OF OPTICAL CORRECTION PLATES

A specific ruby laser rod, used in a specific optical pumping geometry, and operated at a specific flashlamp voltage and rep rate, will give rise to a specific optical distortion which can be corrected with a simple correction plate. One method of correction is to figure the end of the laser rod to compensate for the measured distortion. This is a painstaking procedure and is useful only under one set of operating conditions. An alternative method would be to figure a glass correction plate, to be used in series with the laser rod. This too is painstaking, but somewhat more versatile. We have chosen to concentrate on a third method which involves a desensitized correction plate which can be made automatically on a tape-controlled milling machine equipped with a small-radius diamond tool ($r = 1$ or 2 mm).

This type of correction plate consists of a ground glass plate which has been coarsely figured to provide a scaled-up correction. This plate is then immersed in an index matching solution to scale down the correction and eliminate the scattering at the ground surface. If n is the index of the glass and Δn is the index mismatch between the glass and liquid, then the scaling factor is $(n/\Delta n)$ and the coarseness of the ground surface which is equivalant to a quarter-wave figure on a polished corrector plate will be $(\lambda/4\Delta n)$. For example, if the interferogram shows that 15 wavelengths of optical correction are required, this can be scaled up to 1 mm so that a glass plate can be conveniently ground to the

115

proper contour, and then scaled down again by immersion in a liquid whose index differs from that of the glass by just 0.015. The reflection at the interface will be less than 0.003% and the surface figure on the ground glass must be good to only about 10 microns.

While the grinding of the correction plate should ultimately be done by a tape-controlled computer, we foresee no difficulty in doing this by hand with an optical milling machine in order to demonstrate the feasibility of this type of correction.

We plan first to "optically correct" a random piece of glass -- such as a poor quality microscope slide -- and then optically correct a ruby laser rod and demonstrate its improved beam divergence and threshold.

Although we feel that this type of interferometric assessment and subsequent optical correction provides a viable means for obtaining low beam divergence from high power solid lasers and/or amplifiers, one should certainly not rule out other techniques. For example, the use of disc-segmented laser rods avoids the problem of radial thermal gradients entirely. Alternately, by going to a liquid laser system (either a Nd^{+++} solution or an organic dye solution) the laser medium itself can be flowed and thus replaced between pulses in a repetitive sequence. We are exploring the feasibility of using a rhodamine 6G laser in this way, with an initial emphasis on getting a good idea of the overall efficiency of such a system operating at an average power of 10 to 100 watts.

REFERENCES

1. University of Rochester, Institute of Optics,
    "Time-Resolved Spectroscopy and Interferometry of
    Laser Rods", Status Report #3, Contract No.
    AF19(628)-2860, April 1964.

2. Hercher, M., "Optical Characteristics of Ruby Laser
    Emission", Ph.D. thesis, University of Rochester,
    1963.

SECTION IV

A STUDY OF LASER BEAM-STEERING TECHNIQUE LEADING TO BEAM-STEERING DEVICES IN THE MULTI.-MHz RANGE

J. M. Forsyth and P. Nebolsine

1. INTRODUCTION

This report describes the study of a system for producing a high frequency (50-100 MHz) scanning laser beam with moderate resolution (approximately 30 resolution elements per line). The system consists in locking the phases of a set of transverse modes having a common longitudinal quantum number. In this way the close resemblance between the wave functions of a curved-mirror optical cavity and the wave functions of a quantum mechanical harmonic oscillator is applied to produce an oscillating wave packet in a plane transverse to the laser cavity axis.

Such a system was first studied theoretically and experimentally by Auston.[1,2] His experiments were performed on a He-Ne laser having limited bandwidth and capable of supporting only a few low-order transverse modes. His theoretical analysis showed, however, that the number of resolution elements in the scanning beam should be proportional to the number of modes locked in the above way. He also showed that the scanning frequency would be equal to the difference frequency of adjacent-order transverse mode resonances. The construction of a high-speed scanning system with even moderate resolution would, therefore, require the use of a laser medium with a considerably wider bandwidth than that possessed by the He-Ne system. We have begun an investigation of transverse mode-locking phenomena in the argon ion laser, a system whose bandwidth is an order of magnitude greater than the He-Ne laser.

2. LASER CONSTRUCTION

Increasing the number of resolvable spots in the scanning output of a transverse mode-locked laser requires the oscillation of a large number of transverse modes. In order to achieve oscillation of very high-order transverse modes the optical cavity must have high relative aperture; this requires a large-bore laser. Since large-bore argon ion lasers are not available commercially we undertook to construct such a laser.

Helical-coil radio-frequency excitation first reported by Goldsborough and Hodges is especially well-suited for exciting short, large diameter ion lasers.[3] Since we had considerable experience with radio-frequency toroidal field excitation of ion lasers we chose helical-coil excitation for our present experiments. We were able to use exisitng power supply equipment since the power and frequency requirements of the toroidal and helical-coil systems are similar.

The first discharge tubes were constructed out of quartz. Concentric tubes were fabricated with ring seals; the space between the inner and outer tubes served as the water jacket. The ends of the tube were ground at Brewster's angle and UV-grade optical quartz windows were epoxied in place. The laser tube was connected to a vacuum system and gas reservoir which permitted adjusting the filling pressure and control of gas purity.

Quartz plasma tubes with bore diameters of 6 mm and 10 mm were constructed. The 10 mm structure experienced catastrophic failure before satisfactory laser operation was achieved. Laser action was achieved in the 6 mm bore tube at 4880Å. A maximum of 50 milliwatts output was achieved at this wavelength. No useful output could be

120

achieved at other wavelengths. A cavity loss of 5% would extinguish laser action.

Failure of the quartz discharge tube envelope is caused by the limited heat transfer capacity of thin, water-cooled quartz shells. Since an excitation density of at least one kilowatt per cubic cm is desirable for efficient laser operation, severe demands are placed on the discharge vessel walls. It is easy to see that the surface power dissipation requirements of the discharge vessel are greatly increased as the bore diameter is increased. If we supply an excitation power, P, to the discharge over a length of tube, L , then the excitation density will be

$$E = \frac{P}{\pi r^2 L} \quad .$$

Since only a small fraction (approximately 10^{-4}) of this energy is removed as laser output, the walls of the vessel must transport an amount of energy given by $P/2\pi rL$ per unit area. The specific power dissipation requirement, S, on the vessel walls is thus seen to be

$$S = E\ r/2 \quad .$$

For a value of E of 1 Kw/cc and a tube radius of 3 mm we find that S is 150 w/cm^2. While this study was in progress a report was published giving a figure of 140 w/cm^2 as an upperdissipation limit for water-cooled quartz structures of this kind.[4] This was in good agreement with our findings. The 10 mm bore tube failed with an excitation density of 800 w/cc, ie. a value of 200 w/cm^2 for S. The same excitation density allowed continuous operation of the 6 mm bore tube; this represents a value of approximately 100 w/cm^2 for S.

Although laser operation at modest excitation density could be maintained in the smaller quartz tube, as the excitation level approached the limit mentioned above the concentration of impurities in the discharge would increase to an intolerable level, severely reducing the output power. This effect is evidently due to the sputtering of material from the vessel walls in contact with the discharge. However, even regions of the tube not in direct contact with the discharge were affected. For example, the optical quality of the Brewster windows was severely degraded after only 25 hours of actual laser operation.

It was obvious that a more sophisticated discharge vessel design was essential to enable meaningful experiments to be performed. Accordingly, while preliminary experiments were being performed on the small quartz tube a discharge vessel was designed and constructed out of beryllium oxide, a ceramic with high power dissipation capability which has seen success in small-bore commercial ion laser designs. The use of beryllia walls in our laser has solved or minimized the major problems encountered in operation with the quartz tubes. We are currently operating a 10 mm bore beryllia tube. The excitation density which can be supplied to this tube is presently limited by our power supply capacity.

We will briefly describe the constructional features of the beryllia laser tube. This construction is illustrated in figure 38. The ceramic tube was made from a solid bar of beryllium oxide drilled out to a bore diameter of 0.400 inches and an average wall thickness of 0.078 inches. The overall length of the ceramic tube was 12.5 inches. Beryllia rings were glassed onto the ceramic tube approximately one inch from each end. Brass assemblies were then epoxied to these

122
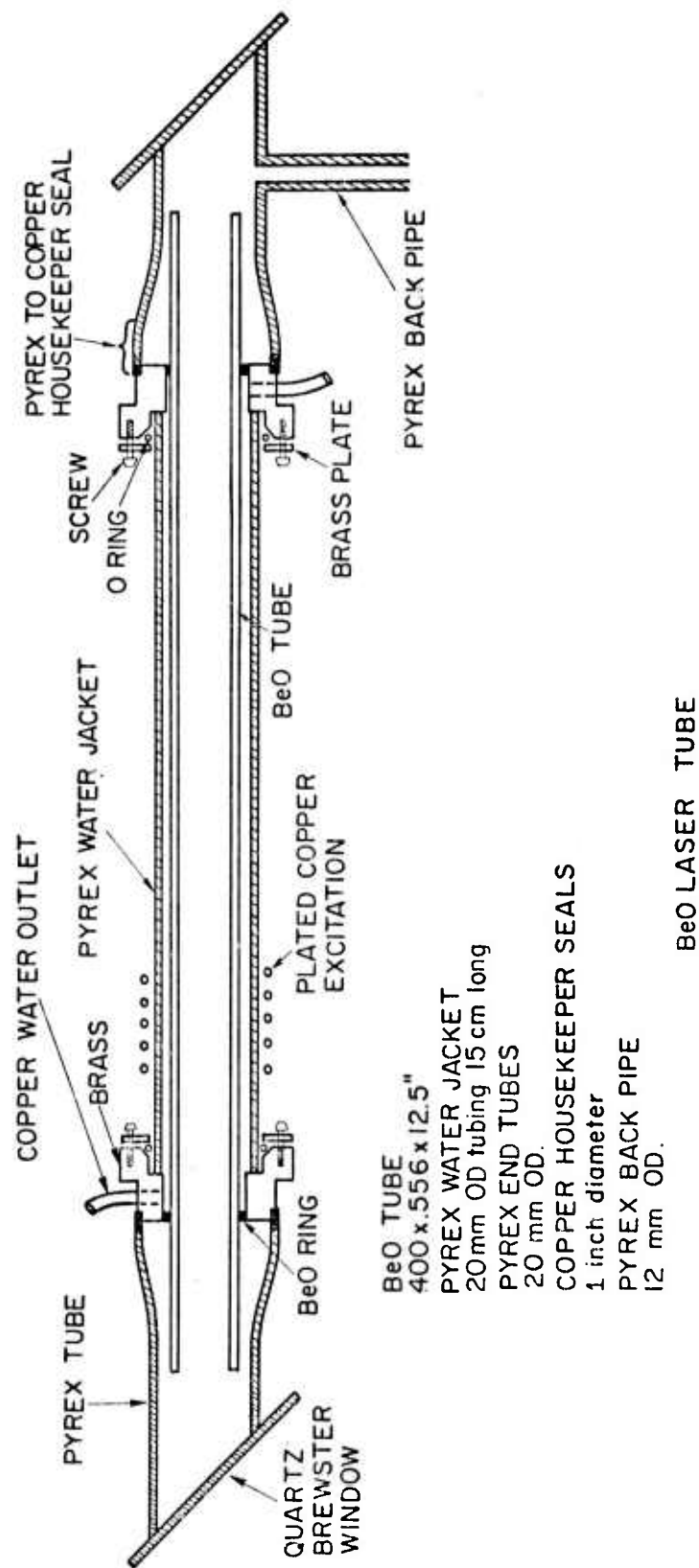
Figure 38. Details of the beryllia laser tube.

COPPER WATER OUTLET

PYREX TO COPPER
HOUSEKEEPER SEAL

PYREX WATER JACKET

BRASS

SCREW

O RING

BeO TUBE

PLATED COPPER
EXCITATION

BRASS PLATE

PYREX TUBE

PYREX BACK PIPE

BeO RING

QUARTZ
BREWSTER
WINDOW

BeO TUBE
400 x .556 x 12.5"

PYREX WATER JACKET
20mm OD tubing 15 cm long

PYREX END TUBES
20 mm OD.

COPPER HOUSEKEEPER SEALS
1 inch diameter

PYREX BACK PIPE
12 mm OD.

BeO LASER TUBE

123

rings. These assemblies carried water inlets while providing seals to the pyrex water jacket and the glass-to-metal housekeeper seals enclosing the ends of the stucture. The housekeeper seals were soldered to the brass assemblies. Brewster windows of UV-grade optical quartz were epoxied to the 20 mm pyrex tubing extensions from the housekeeper seals. The ceramic tube was extended beyond the brass assemblies in this design to insure against direct discharge contact with the epoxy and solder joints in that region. A 12 mm pyrex tube is joined near one of the Brewster windows for a connection to the gas handling system. "Man-o-lok" connectors were used between the back pipe and the vacuum system to enable rapid changes to be effected in the system. These connectors have proved useful and capable of holding vacuum in the 10^{-7} Torr range.

Operation of the beryllia-bore tube has been entirely satisfactory up to now. RF power is supplied through a thirteen turn coil closely wrapped around the pyrex water jacket. It was found that corrosion of the excitation coil would lead to electrical breakdown, thus requiring special precautions in assembly and operation. The coil is cadmium plated refrigeration tubing and is water-cooled in operation. The laser is driven by a single-stage Hartley-type power oscillator through an impedance matching network. A maximum DC plate input to the oscillator of 11 Kw can be achieved. Under these conditions we measure a power of 4.6 Kw in the bore, determined by measuring the temperature rise in the cooling water. This provides an excitation density of only 500 w/cc in this structure. The gain and output power are thus rather low at present;

124

an output power of 0.1 watt at 4880Å is obtained with
an output mirror transmission of 1%. Operation at 5145Å
can only be achieved with high reflectance mirrors at
present. Nevertheless, such performance is adequate for
preliminary studies of the type to be described.

A desirable (though not essential) feature of the
beryllia tube is its apparent freedom from accumulation
of impurities in the discharge. This is similar to
its performance in small-bore designs , and is undoubtedly
due to the excellent resistance of beryllia to corrosion
from the discharge.

More importantly, the beryllia tube has shown a
pronounced improvement in the preservation of the optical
quality of the Brewster windows. In figure 39 we show a
comparison of the optical quality of Brewster windows
removed from quartz and beryllia discharge tubes. In
each case the windows were illuminated by slightly divergent
light from a He-Ne laser. A shearing interference pattern
was formed by light reflected from the two window surfaces.
The surface which remained external to the discharge was
determined to be flat by comparison with a reference flat.
Therefore, the fringe structure shown is due to the de-
formations of the surface which was adjacent to the discharge.
The upper interferogram is from the window used on the
quartz tube; this window had been located approximately
11 cm from the visible end of the discharge column. It
was exposed for 25 operating hours. The elliptical region
in the center of the interferogram shows the degradation
of the inner window surface clearly; the outer area shows
the original window quality.

The lower interferogram was made from a window used
on the beryllia-bore laser for 70 hours. It was located
approximately 13 cm from the discharge column during opera-
tion. The deterioration is nowhere greater than a half-
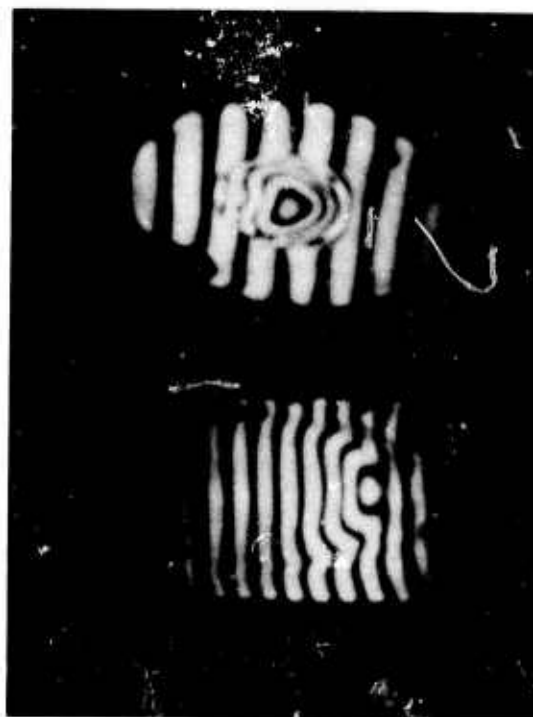
(a)

(b)

(a) Quartz tube window

(b) Beryllia tube window

Figure 39.   Shearing interfer‹ ;rams
of Brewster windows.

126

wavelength and is considerably less over most of the
aperture. Taking into account the duration of the window
exposures, an eight-fold improvement in the stability of
the optical quality can readily be claimed.

The maintainance of high optical quality in the
cavity is necessary for the study of high-order trans-
verse mode phenomena. In figure 40 we show some of the
output field distributions which are readily observed from
our large-bore lasers. The cavity configuration used in
these experiments utilized a high-reflectance curved
mirror and a partially transmitting plane mirror separated
by approximately 60 cm. The outputs shown were observed
with the laser operating just above threshold. The single-
axis modes were observed with the use of a single straight-
edge inserted into the cavity or, sometimes, with a
slight misalignment of the mirrors. No other intracavity
stops or wires were used. The highest order single trans-
verse mode observed has been a $TEM_{0,98}$ mode. When the laser
is operated well above threshold many transverse modes
oscillate simultaneously, producing extremely complex
far-field patterns.

A very interesting observation is made when the cavity
geometry is adjusted so that the geometrical ray paths
within the cavity become re-entrant.[5] (This will occur
when the longitudinal mode separation is an integral multiple
of the frequency of separation of adjacent-order transverse
modes.) Figure 41 shows two examples of the outputs which
can be obtained. Instead of a complex field distribution
we observe Lissajous patterns. Under these conditions
the output fields are very sensitive to slight adjust-
ments in the cavity length. In one experiment we observed
that the Lissajous pattern would rotate suddenly through

127
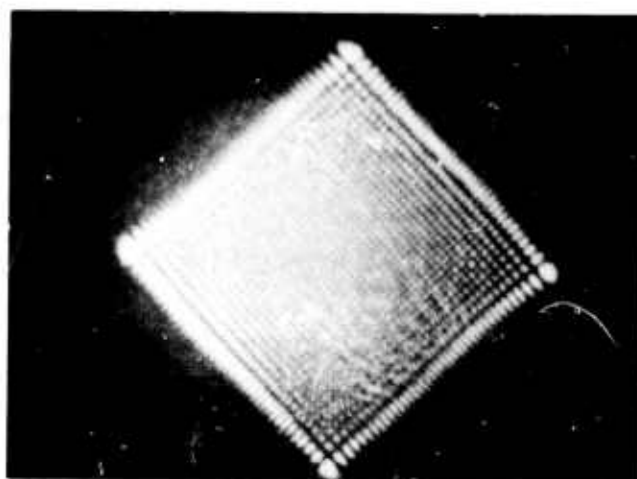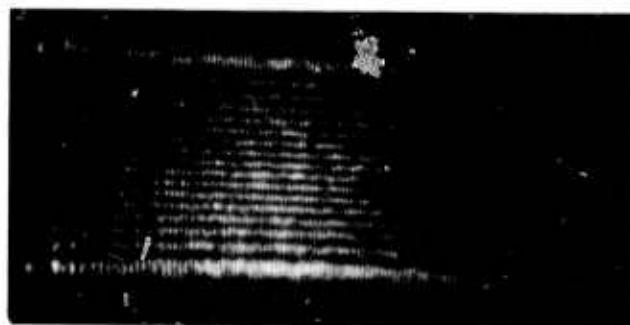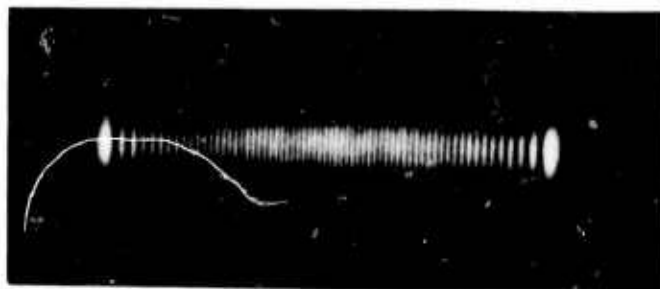
Figure 40. Single transverse modes.

128

Figure 41. Near re-entrant cavity modes.

90 degrees when a mirror displacement of 0.105 inches was made. This is consistent with the expectation that the phase shifts for fields distributed along the tangential and sagittal planes of tilted Brewster windows will be different. Larger displacements will, of course, produce a return to the conventionally observed mode patterns. It is interesting to note that the reentrant mode patterns are observed over all ranges of excitation that we were able to achieve. Their stability seems to be governed by the optical and mechanical stability of the cavity.

The spectral bandwidth of the large-bore lasers is somewhat larger than that observed for conventional small-bore tubes. Using a scanning confocal Fabry-Perot interferometer we measured a free-running spectral bandwidth of approximately 12 GHz at 4880Å. By inserting an intracavity etalon into the laser, a single mode could be tuned over a 16 GHz range. This indicates that the ion temperature of lasers excited in this fashion may be somewhat higher than that of conventional, small-bore, wall-stabilized discharges. This bandwidth was larger than we had anticipated in our study and indicates a possibly greater information handling capability for the ion lasers than previously estimated.

3. BEAM DEFLECTOR

Previous experiments on transverse mode-locking in He-Ne lasers utilized acoustic vibration of one of the cavity mirrors to induce locking. Such a technique is inherently limited in amplitude and tunability. We elected to investigate the use of electro-optic beam deflectors as intracavity modulators. Several modulator configurations were studied; the simplest and cheapest design was picked

for the initial experiments. Ammonium dihydrogen phosphate (ADP) was chosen as the electro-optic material. When used in a 45-degree Y-cut configuration, the transverse electro-optic coefficient of ADP is equal to that for potassium deuterium phosphate (KD*P) in the 0-degree Z-cut configuration. The unit cost of ADP is approximately 1/4 that of KD*P for crystals of good optical quality. Unfinished crystals were purchased and fabricated to shape and polished in our own shop. The crystals were cut in the form of Brewster-angle wavelength-selecting prisms and polished.

The crystals were placed in the laser cavity in a cell which contained triangular electrodes in contact with the top and bottom surfaces of the crystal. Since the transverse electro-optic effect produces a change in the index of refraction for an extraordinary ray traveling along the optic axis, such an electrode configuration creates a prismatic region within the crystal. This action causes a deflection of the beam which is proportional to the applied electrode voltage.

The use of Brewster-angle faces on the crystal is not related to the beam deflection function; it serves only to minimize insertion losses. The high dispersion configuration for the prism was chosen because of the desirability of isolating oscillation on one wavelength for preliminary experiments. The effect of operating the laser on simultaneous competing transitions in a transverse mode-locked configuration will be deferred until the present studies are completed.

Our deflectors were cut from crystals 1.3 cm x 1.3 cm x 3.8 cm. The base of the prism is approximately 3 cm when fabrication is completed. We calculate a deflection

131

sensitivity of the order 1.2×10^{-8} radian/volt in our configuration. In experiments with He-Ne a mirror deflection amplitude of 10^{-6} radians was reported to give rise to mode-locking. Thus we expect to require some few hundred volts of drive for the modulator in our case. Modulation frequencies in the range 40 - 70 MHz were used in our experiments. To obtain the required drive voltage communications-type power amplifiers (with 50 ohm outputs) were coupled to the crystal electrodes through a reactive impedance matching network. Many of the experiments were conducted with an RF Communications type RF-805 broadband power amplifier capable of delivering 10 watts into 50 ohms over a frequency range of 100 KHz to 80 MHz and beyond. Using a high frequency probe we measure up to 200 volts (rms) of drive across the cell with this exciter. An additional power amplifier stage was constructed using a type 4-65A power tube. To date we have not found the extra excitation capability necessary, however.

Because of the low gain exhibited by the short argon ion laser discharge, successful use of the beam deflector in the cavity demands careful attention to minimization of insertion loss. Moreover the transmission quality of the finished crystal should meet high standards to avoid suppression of the delicate high-order transverse-mode structures. Since the surface quality of materials such as ADP deteriorates upon prolonged exposure to a normal atmosphere it was anticipated that our crystals would require refinishing periodically. For this reason it was decided to do all fabrication in our own optical shop.

Numerous polishing techniques were investigated, including procedures generously described to us by some commercial shops. In the end we have departed from previously described and suggested procedures in our own work. Most of the techniques tried are capable of producing good to excellent surface figure. However, production of a very

132

low scatter surface remains a challenge. Our best efforts
to date involve polishing on a pitch lap using fluorocarbons
instead of water to carry the polishing powder. Our investi-
gations in this sphere are continuing. Very-low-scatter
surfaces appear to be achievable with water-soluble mat-
erials. Maintaining surface quality after production appears
to require storage in a dry environment or the development
of a satisfactory coating technique. The production of
durable coatings is presently limited by the inability
to heat the crystalline material during vacuum evaporations
due to its low temperature of decomposition.

To protect the polished faces of the crystal we
performed a majority of our experiments in a configuration
using polished quartz plates separated from the crystal
faces by a thin film of index-matching fluid. Various
fluids were tried; the best index match was achieved
with silicone fluids although these tend to scatter light
significantly. The performance of the index-matching
fluids will be discussed further in the descriptions
of experimental results.

4. PRELIMINARY SCANNING STUDIES

With both the discharge tube and the modulator
operational, experiments were begun to induce transverse
mode-locking. The optical cavity arrangement used is
shown in figure 42. A partially transmitting plane mirror
and a high-reflectance curved mirror were used. The beam
waist for modes in such a cavity occurs at the plane mirror;
therefore, the discharge tube will represent the effective
aperture stop in the system. To maximize the number of
transverse modes which will have low diffraction loss
requires that the aperture stop be located as close to the
beam waist as possible. It was also desired to locate
the modulator close to the plane wave region, so it was

133

MIRROR 2

ELECTROOPTIC
MODULATOR

60 cm

45 cm

MIRROR 1
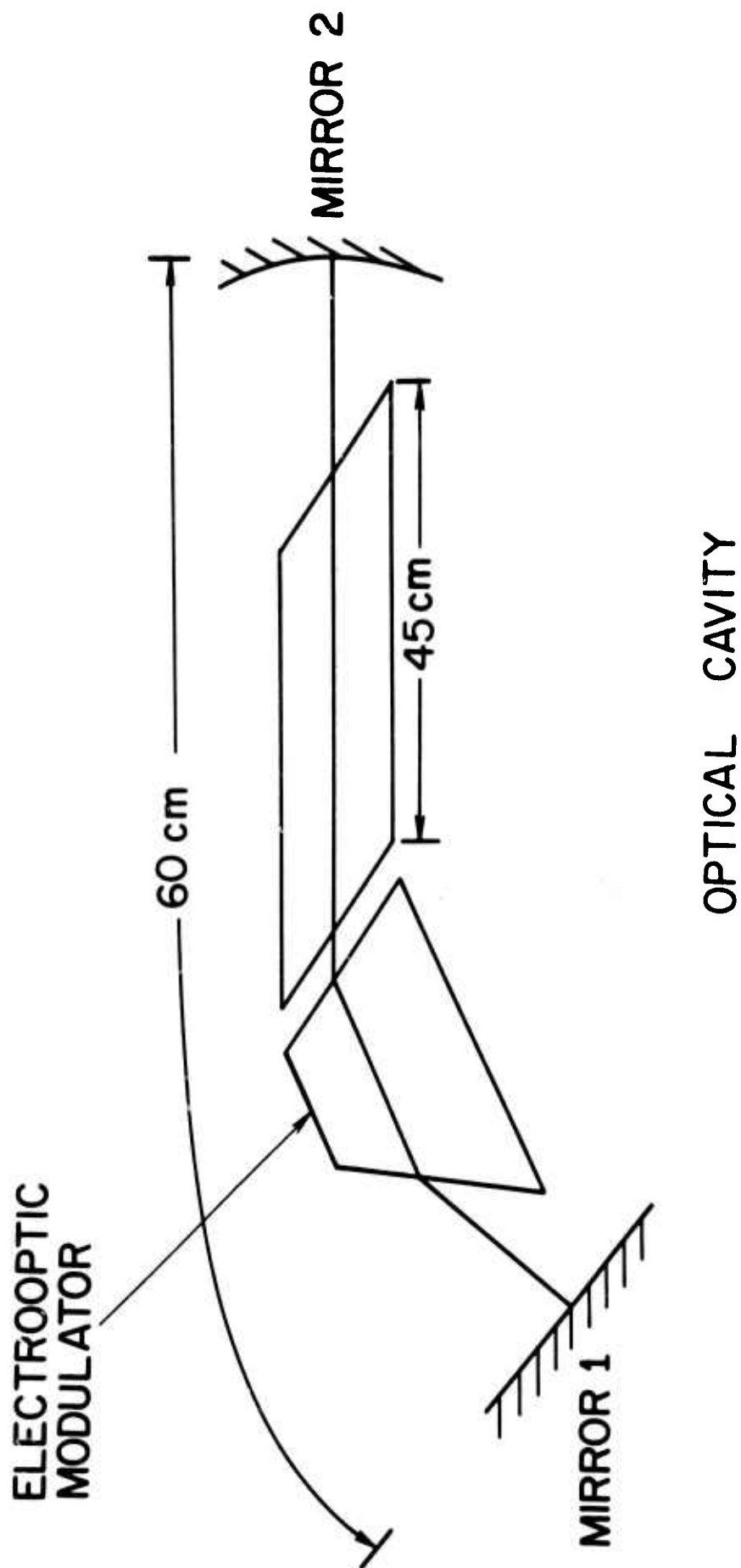
OPTICAL CAVITY

Figure 42. Optical cavity arrangement used in experiments to induce transverse mode-locking.

not possible to satisfy the previous criterion to the highest degree. Since the modulator cell had a length of approximately 5 cm, however, the loss in performance should be entirely negligible.

Once the aperture stop is fixed with respect to the plane mirror, only the mirror separation and the curved-mirror radius remain to be chosen. For a given separation in frequency between adjacent-order transverse modes any number of combinations of separation and radius are possible. For our purpose it is necessary to chose a combination which will produce the smallest value of beam waist in the aperture stop. Since we had a limited selection of high-reflectance curved mirrors available, it was a great advantage to be able to adjust the modulation frequency and thus the mirror separation to obtain the highest possible number of transverse modes. This flexibility would not have been possible with piezoelectric intracavity modulation.

Numerous transverse mode-locking effects were observed in our experiments. The simplest observation was a visual one. With no voltage applied to the modulator a complex but stationary field distribution is observed in the output. When modulation is applied the spatial structure in the output disappears on the transverse axis parallel to the deflection axis. (This is observed for both single-axis and rectangular mode patterns.) The disappearance of transverse structure on the output is observed to be critically dependent on the modulation frequency throughout the range of modulator excitation that we could achieve.

To determine whether our visual observations were correlated with mode-locking effects we performed measurements on both the optical and RF spectrum content of the output. In addition we observed the temporal-spatial distribution of the output to determine that beam scanning was taking place.

135

The results of the RF spectrum analysis are shown in figure 43. In these experiments a Hewlett-Packard HP-4220 PIN photodiode with a baseband response in excess of 1 GHz was used to detect the optical signal. Using a Tektronix 1L20 Spectrum Analyzer the signal was displayed on a Tektronix 555A oscilloscope. Observations were made at frequencies corresponding to the separation of adjacent longitudinal cavity modes and to the harmonics of adjacent transverse modes. (The fundamental transverse mode interval could not be monitored because of pickup from the modulator excitation circuitry.) As shown in figure 43, when the modulation is applied at the proper frequency, the output fluctuations at the longitudinal-mode interval are suppressed while the fluctuations at harmonics of the transverse-mode interval are greatly enhanced. The measurements are shown for a longitudinal-mode interval of 240 MHz and the second harmonic (138 MHz) of the transverse mode interval. Higher-order transverse-mode harmonics show similar behavior.

It is worth noting that theoretically a transverse mode-locked laser is very similar to the FM laser--the total time-averaged intensity should be constant. Because we were using a detector with a small active area in the above measurements we were not performing a time average unless the structure of the field distribution were actually uniform in space and time. As a check, then, we examined the beat frequency spectrum using a Electro-Nuclear Laboratories detector having an active area of 20 mm^2 and a baseband response of greater than 200 MHz. Using this detector we observed a greatly reduced output at transverse-mode harmonics when the modulator excitation was applied. The results obtained with the small area detector are, of course, explainable in terms of a localized distribution

Modulator

"off"
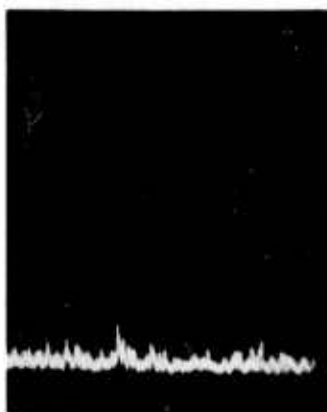
(a)
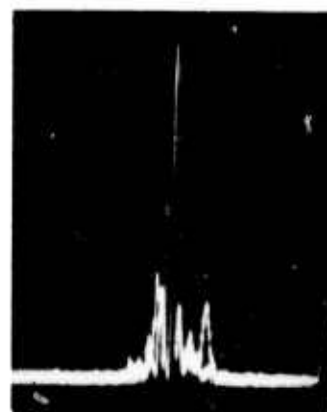
(c)

Modulator

"on"
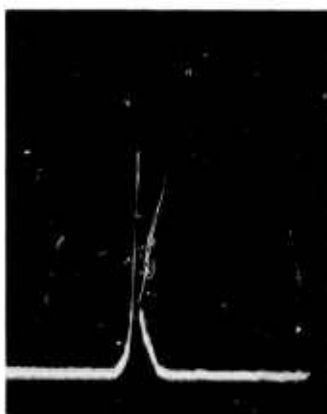
(b)

(d)

(a), (b)   Display centered at 138 MHz
           (Transverse-mode separation = 69 MHz)

(c), (d)   Display centered at longitudinal-mode
           separation, 212 MHz

Figure 43.   RF spectrum displays (100 KHz/div.).

137

of energy sweeping past the detector aperture periodically.

The reduction in the beat frequency content at the longitudinal-mode interval is an indication that a single set of transverse modes is effectively saturating the laser gain profile. Additional evidence for this was obtained from measurements of the optical spectrum with a scanning Fabry-Perot interferometer. The results are shown in figure 44. These measurements were made with a Coherent Optics Model 470 Optical Spectrum Analyzer. The spectrum analyzer had a free spectral range of 8 GHz using confocal geometry. Figure 44a shows a typical oscilloscope display of the signal from the spectrum analyzer when no excitation is applied to the modulator. The spectrum is observed to fluctuate rapidly with an irregular amplitude distribution. Figure 44a is an integration of several sweeps; single sweeps show only a few modes oscillating at any instant. In figure 44b we see the spectrum obtained with excitation applied to the modulator. The spectrum is now relatively stable with a large number of modes in simultaneous oscillation.

The results of the previous measurements suggest that transverse mode-locking has been achieved. To determine if this kind of operation corresponds to the theoretical model of a scanning beam we performed the following measurement. A fast photodiode with very small active area was placed in the beam and the time-resolved output examined with a sampling oscilloscope. The output was recorded for various positions of the detector relative to the axis of the beam. The results of one series of measurements is shown in figure 45.

The time-resolved measurements were made using a Texas Instruments TIXL-55 avalanche photodiode having an

(a)

(b)
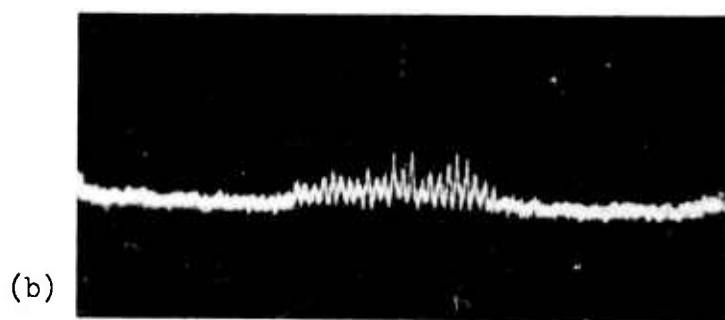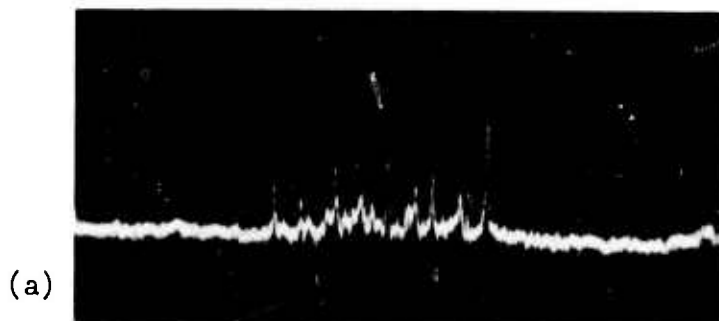
    (a)   Modulator "off"

    (b)   Modulator "on"

Figure 44. Scanning Fabry-Perot oscillograms.

(a)
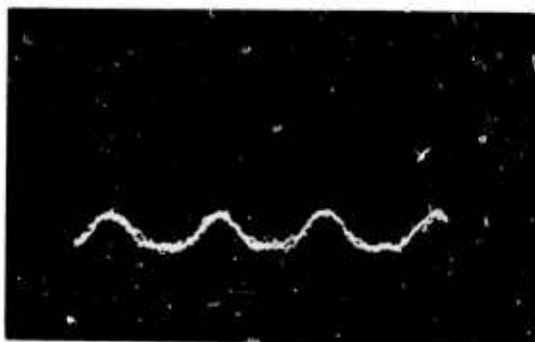
(b)
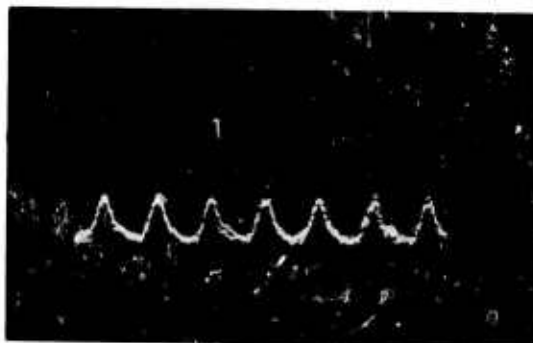
5 nsec/div

(a) Detector at edge of beam

(b) Detector at middle of beam

Figure 45. Time-resolved output in transverse
mode-locked configuration.

active area of 2×10^{-2} mm^2. The risetime was estimated
independently to be less than 200 psec., using a fast laser
diode source. The detector output was displayed using a
Tektronix 3S2-S2 sampling oscilloscope having a nominal
equivalent risetime of 50 psec.

Figure 45a shows the time-resolved output when the
detector was located near the edge of the beam while
figure 45b shows the output when the detector was located
near the axis of the beam. The time scale in each case is
5 nsec/div. In this instance it appears that the pulse
repetition rate is twice as great when the detector is
located on axis as when it is located near the edge of the
beam. We can account for this by noting that a sinusoidally
scanning beam would cross the detector twice each scanning
cycle when the detector was located on axis while it
would fall on the detector only once each cycle at the
very edge.

In order to get adequate signal from the detector for
the time-resolved measurements it was necessary to focus
the beam onto the detector surface. Under the focused
conditions the total width of the output beam was approximately
5 mm in the detector plane. Since the detector has an active
area of 2×10^{-2} mm^2 it is clear that the detector could
spatially resolve to 10^{-2} of the scanning width or better.
Moreover, since at a frequency of 69 MHz a scanning spot
will transverse a line in approximately 8 nsec, the time
resolution of the detection and display equipment would
convert to an unambiguous spatial resolution capability
of approximately 3×10^{-2}. It is clear from the photographs
that we are not beginning to approach that kind of resolution
during this measurement. Moreover, these time-resolved
measurements have been made on several laser/modulator
systems over a period of a few months and the results
often are more complex and less readily interpreted in
terms of a simple scanning beam. A comparison of the

141

experimental conditions for these measurements showed
that results of the type shown in figure 45 were generally
achieved after a fresh change of some intracavity optical
component, especially the modulator crystal. As a result,
we have begun to investigate the influence of the intracavity
optical quality on the performance of   ransverse mode-
locked scanning beam.

The most important discovery we have made concerns the
influence of the rapid degradation of the overall optical
quality of the modulator system and the apparent cause of
the degradation. As noted previously, we have not yet
been able to produce very low-scatter surfaces on the ADP
crystals used for the modulator. To reduce the insertion
loss we have resorted to contacting quartz windows against
the crystal faces with index-matching fluids.   Twyman-Green
interferograms of such a modulator cell are shown in figure 46.
Approximately 200 volts (rms) excitation was applied to
the modulator for several minutes. Immediately after turning
off the excitation the interferogram in figure 46a was ob-
tained. Thirty seconds after removing the excitation the
interferogram was obtained in figure 46b. The interferometer
was then realigned to give figure 46c. This shows the
optical quality of the modulator without the effects of
excitation. The same experiment was repeated with a mod-
ulator cell having no windows and no index-matching fluid.
In this case no change could be detected in the optical
quality of the prism under application of excitation.
It is clear that there is severe degradation of the
optical quality of the index-matching fluid in the presence
of a high-frequency RF field. This degradation has been
observed in several silicone fluids used for this purpose.
We have not found a satisfactory index-matching fluid from
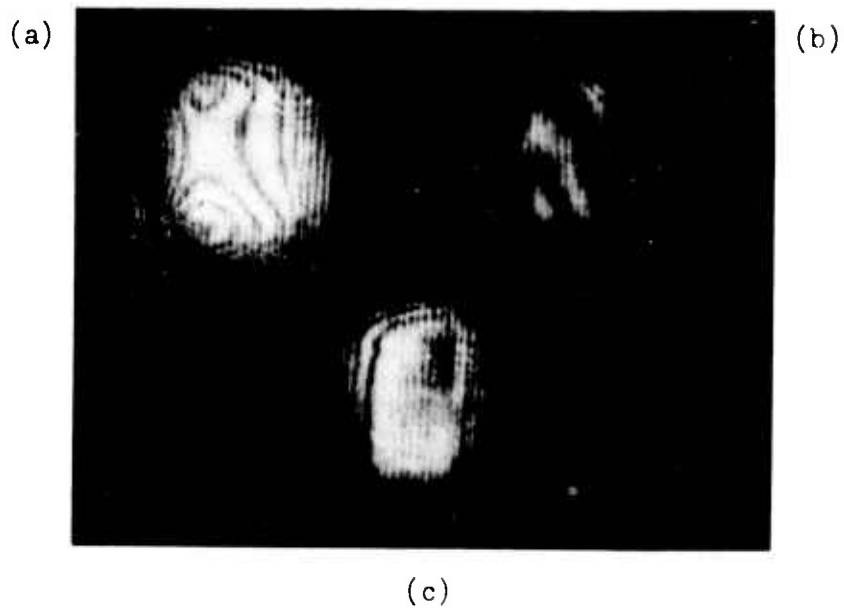
(a) Voltage applied

(b) Voltage off

(c) Voltage off with realignment

Figure 46. Twyman-Green interferograms
of electro-optic modulator.

143

this standpoint as yet.

The degradation of the index-matching fluid appears to have both a reversible and an irreversible component. Shortly after a fresh cell is prepared scanning performance of the type shown in figure 45 can be obtained. After an hour or more of operation no meaningful results can be obtained. Overnight recovery of performance is observed but after a few days a fresh cell must be prepared by cleaning off the fluid from the window and crystal surfaces and starting fresh. The interferograms in figure 46 are taken with a freshly prepared cell. It is clear that even here the optical quality leaves something to be desired since we use virtually the whole aperture of the beam deflector. Further work on this problem appears inevitable.

5. SUMMARY

During this initial contract period we have carried out a preliminary study of the conditions for achieving a high frequency scanning beam by locking a set of transverse modes in an argon ion laser. During this phase we have made the following important achievements:

1. We have constructed a reliable, large-aperture argon ion laser well-suited to the production of high-order transverse modes.

2. We have used electro-optic beam deflectors as intracavity modulators to produce transverse mode-locking in the large-bore laser.

3. We have determined that high intracavity optical quality is essential to the achievement of a simple scanning beam in a mode-locked configuration.

The most immediate problem requiring attention is that

144

suggested by item 3 above. Improvements in the optical quality of our intracavity optics should materially improve the performance of our present system. Secondly, it is important to be able to operate the present system at higher excitation levels so the system will be less sensitive to small, sometimes selective insertion losses and to achieve more power output. The importance of mode competition effects at higher levels of excitation must be ascertained. We intend to pursue these topics of investigation in the immediate future.

REFERENCES

1. D. H. Auston, "Transverse Mode Locking", IEEE, J. Quantum Electronics, QE-4, 420 (1968).

2. D. H. Auston, "Forced and Spontaneous Phase Locking of the Transverse Modes of a He-Ne Laser",IEEE, J. Quantum Electronics, QE-4, 471 (1968).

3. J. P. Goldsborough & E. B. Hodges, "Helical Coil cw rf Excitation of Ion Laser Discharges", Paper presented at 13th International Electron Devices Meeting, Washington, D.C., Oct. 19, 1967.

4. W. H. Seelig & K.V. Banse, "Argon Laser Emits 150 Watts c-w", Laser Focus 6 , 33 (1970).

5. D. Herriott, H. Kogelnik, & R. Kompfner, "Off-Axis Paths in Spherical Mirror Interferometers", Appl. Opt. 3, 523 (1964).

SECTION V

STUDY OF O.T.F. MEASUREMENTS AND APPLICATIONS

A. A PROCEDURE FOR OVERALL LENS EVALUATION USING O.T.F. DATA

David Dutton

The literature of image evaluation is rich in concepts such as spread function, aperture function, optical transfer function, resolving power, photographic resolution, encircled energy, Strehl definition, etc. Of these the former are extensive functions : OTF, for example, complex and two-dimensional. The latter are single merit parameters which abstract, in various ways, from the copious information of a complete function; which of them is "best" , and its numerical value, depends on the application and the receiver. All refer to a single point in image space, and will vary with focus and with position in the field; and each refers to a single wavelength, or one particular spectral blend of the imaging light.

Thus an attempt to characterize overall imaging performance in complete detail leads to a merit function of 5, or 8, or 10 dimensions, hard to cope with in human decision terms. The art of lens design has developed to handle this complexity, and relies very heavily nowadays on highly sophisticated design programs and very large computers. Testing a complicated lens once it is built, however, tends to be a much more cursory process. A lens designed to work to the diffraction limit can be relatively easy to test, since it is fairly easy to tell, even by visual inspection, whether the spread function is an Airy disc. Designs which compromise this limit to achieve wider field, fewer elements, or the like, require a more quantitative and objective testing procedure, if one wants to verify the designer's predictions

or the success of the fabrication procedure; and the test, of a completed prototype, can in principle become as complex a problem as the design. Whatever the test method, a lot of measurements seem to be needed, and these traditionally are tedious to make, and once made too voluminous to digest easily. A frequently used procedure for photographic objectives is to determine, as an overall merit parameter, an over-the-field weighted average photographic resolution, normally by a series of photographs of standard targets covering the desired field and range of focus, interpreted by detailed microscopic examination of the plates by a trained reader, in critical experiments by several readers when better statistics are needed. "Objective" tests, of which a modulation-transfer function measurement is among the most currently popular, tend to be limited to one to three field points or a small set of other parameters and can be considered satisfactory if the answers resemble the designer's estimates to some degree. Because of the massiveness of the potential problem, exhaustively thorough tests, even of expensive prototypes of complicated lenses, are probably rarely made.

Our aim in this work is to explore the practicality of taking a great many measurements, but in some automated way, and then using a large computer to digest them; so that a more thorough evaluation, and one adapted to human decision making, can be done with no more trouble, or perhaps with much less trouble, than traditional methods require. We wish to base the evaluation on some objective physical measurement, and to abstract from many raw numbers a kind of pyramidal display of derived merit numbers, matching where appropriate some of the traditional quality parameters and perhaps adding to the variety of choice, of quality parameters, in new ways which

experience will show to be useful. We would like to be able to vary freely the location and orientation of the image plane being tested, to find for the actual lens, or have the computer find, an image plane which is optimum for one or more merit parameters; and to establish empirical tolerances about the optimum.

For raw data we have chosen photoelectric measurements of the point spread function, throughout the image space. To manipulate and display the information contained such data, it is convenient to transform them to the spatial frequency domain via the O.T.F., but the emphasis is not on the use of O.T.F. per se. Neither is there an emphasis on our particular way of measuring OTF : we chose an edge-scanning technique with digital processing into OTF curves, because the instrumentation needed is simple and lends itself to automation, and the results naturally adapted to massive use of a computer in the evaluation step.

The procedure calls for first making an "OTF map" by scanning point images, in radial and tangential sections and racking through focus, for a chosen grid of points covering the field. Intensity in each edge trace is recorded digitally on magnetic tape. The tape is read by a computer, each scan is reduced to an OTF curve and filed in permanent memory. When the map is complete, perhaps with several hundred such curves, the evaluation program uses these files to prepare merit figures, e.g. the weighted-average MTF, or the predicted photographic resolution ("AWAR"), along with numbers that measure particular aberrations such as astigmatism or coma, or abstracts such as the Strehl criterion. The computer can

then prepare a report in as much detail as wanted, for instance a statment of the AWAR value for a particular film, or the average MTF, with a note of what is the minimum value of resolution, or MTF, anywhere in the field, and where; or a detailed report of how these vary over the field; up to finally a full regurgitation of OTF curves, in any desired image plane. The program finds an optimum image plane, if desired.

We have tested the procedure on a standard lens, the same 3-inch f/4.5 wide angle reconnaissance lens used in a previous MTF study[1], by mapping 17 field points. We have extensive OTF-measurement data on the lens from several laboratories, we know design predictions of MTF on axis and at 2/3 full field, and we have some actual photographic resolution data obtained by the Air Force Avionics Laboratory with standard tribar targets. The evaluation results, to be given in the text, are in satisfactory agreement with these cross-checks. (The lens not surprisingly shows defects not predicted by its design, notably azimuthal variations in image quality).

To assess the practicality of the procedure, in terms of time and trouble, we summarize here some numbers rationalized in the text. The full map in our example required 554 image scans to cover a 500 μm focus range for 17 field points, in one color. Our own apparatus is so far only partly automated; actual acquisition time was about 50 seconds per scan, about the same time needed by most commercial MTF machines to draw one MTF curve on graph paper. The same equipment with minor changes could be pushed to about six times higher speed, and have automatic focusing; one can make a conservative extrapolated estimate of about 2 to 3 hours total running time for a full map. This is certainly commensurate with set-up time for such a test under the very

150

best conditions. (In the MTF study, mounting this large heavy lens in any new bench took a day or two at best). Each scan takes about 1 second of central processor time on an IBM 360/model 65 computer, with tabular OTF output and disk entry of all results. The evaluation program takes about 2.5 seconds of CPU time to find and evaluate one image plane, a little less when doing a series of planes. Computing costs appear to be modest, certainly for prototype evaluations. For many applications, half as many field points would suffice for the OTF map.

1. MAKING THE O.T.F. MAP

For the evaluation we will wish to have on file a series of OTF curves describing the image behavior through the whole focus range of interest, and over the entire field. This set will be called the "OTF file" . During original processing of the raw image-scan data, some numbers are abstracted from these curves, namely the MTF at certain chosen frequencies tabulated against focus, to be displayed as "focal-shift curves" and kept in another disk file, the "focal-shift file" .

To make the map, a point image is formed at the desired field point and is scanned repeatedly (in our case by a knife-edge scanner attached to an observing microscope), racking through focus, in the tangential section; and another focus series is taken in the radial section. Each scan is recorded digitally on an incremental magnetic tape recorder, and carries an identifying record giving the focus, the field point, and other relevant apparatus parameters. The edge-trace data are processed using formulae due to Tatian[2] and yield both real and imaginary parts of the OTF. Centration of the scan, which affects the linear-with-frequency part of the spatial phase shift, is done in the computing stage by locating the intensity sample nearest to half full intensity. The phase function that results will be zero if the spread function is symmetrical about its centroid of intensity. The phase shift obtained thus will measure effects of asymmetrical aberrations such as coma, but will not include absolute distortion.

152

The whole procedure is as described in Reference 1.

To cope with the physical metrology problem we have again used the procedure of Ref. 1, to establish field point location and the focus scale. A flat "Reference Plate", made for the test, is rigidly attached to the lens mount near the image plane. Holes bored in the plate locate the standard field positions, and the surface of the plate is the fiducial reference for focusing at each field point. With this expedient, accurate slides and scales are not required of the optical bench. The collimator swings to put the image at the center of the desired locating hole. The focus scale is a dial indicator attached to the observing microscope which is referenced to the plate (by visual focus on the plate surface) as each field point is set up. We must rely on the linearity of the dial indicator over the focus range of interest, e.g. 0.5 mm. Visual focusing has a reproducibility of about 5 μm; for the example lens an appropriate spacing for successive scans is 20 to 40 μm. The surface of the Reference Plate becomes the X-Y plane, the basis of the coordinate system for image location throughout the evaluation procedure.

This approach to metrology appears to work well. For the kind of testing of a sophisticated lens which warrants the whole OTF procedure, the fabrication and mounting of a suitable reference plate does not seem incommensurate with the rest of the procedure, unless the field format is unduly large. Extremely good slides would be needed to do as well.

During original processing, the focal-shift curves are fit by polynomials (usually a cubic). The fitting coefficients are used to locate the maximum

of the focal-shift curve (which will be used later in finding the best image plane), and can be used to interpolate the MTF into particular image planes. Fitting also serves to weed out occasional records where something went wrong during data recording : if a point deviates from the fit by more than a certain tolerance, e.g. 0.2 MTF units, that OTF curve is labeled unreliable and crossed off the data index.

Each field point is labeled by a number (the format is described later in section 3), and the location, in the focal-shift file, of the data for that point is indexed, by point number, in the first record of the file. Within the focal-shift file are pointers to the original curves in the OTF file.

When this kind of mapping has been completed, for as many field points as are wanted for a particular test, the OTF file and the focal-shift file are made available to the evaluation program.

2. THE EVALUATION PROGRAM

The program has been designed on the assumption that a complete
set of OTF and focal-shift data is accessible in random-access files.
Sequential access would probably be adequate, if the original data
were ordered in respect to focus sequence, and if the field points
called for in evaluation are mentioned in the correct order.

There is a short built-in routine for generating appropriate x-y
coordinates, and assigning zone area weights, upon mention of the field
point number. Use of varied formats would require only variation of
this routine.

a. *Optimum Image-Plane Location*

One segment of the program finds an image plane which is "optimum"
in the sense of coming closest to the best-focus positions (meaning
the focus setting at which MTF for a specified frequency is a maximum)
for the various field points. This plane may be allowed to tilt as
necessary to find the most general plane $z = Ax + By + C$; or it
may be constrained to no-tilt, $z = C$. The latter may be more appropriate
if the reference plate plane corresponds to a flange or some analogous
fixed orientation, as the lens is intended to be used. In our notation,
the X-Y plane is the plane of the reference plate and focusing is in the
Z direction, positive values away from the lens.

This segment is invoked by data cards which specify a list of field
points, by their numbers, to be used in establishing the image plane. The

155

computer looks up the focal-shift data in its index and finds the recorded

best-focus positions for the radial and tangential images for that field

point. For the focal-shift curves, three frequencies specified at the time

of the original OTF mapping are used, and cubic coefficients describing the

MTF-versus-focus curves are available in the focal-shift file for each of

those frequencies, one of which is specified at evaluation time for image

plane location, e.g. 60 c/mm. A focus for maximum MTF at the chosen

frequency is taken from the fitting polynomial, for the tangential and for

the radial sections of each field point. The tangential and radial values

are treated as separate field points, and each is assigned a zone area

weight. The zones are segments of annular areas, whose boundaries pass

halfway between field points, and each annulus is divided into as many

segments as there were points (of the same field angle) mentioned in the

list. (The weighting rules are essentially those prescribed in Standard

Mil-150A for defining area-weighted-average resolution.) X and Y coordinates

are assigned to each field point by the built-in routine mentioned earlier.

The plane of best least-squares fit to the observed Z values is found by a

subroutine, either a general tilted plane or one constrained not to tilt,

specified by a control parameter at run time. This will be called the

"optimum" image plane from now on; it is optimized with respect to "best-

focus" and in the example to be described later this criterion, which is

very simple and easy to apply, appears to maximize all the merit parameters

yet examined, nearly enough.

Alternatively, a particular plane may be specified by supplying the

A,B, and C coefficients; or the program may be asked to analyze a series of

156

untilted planes, racking through focus automatically.

b. *Analysis for Merit Parameters*

   (1) **The O.T.F.**

Once image plane coefficients A,B,C are established, the focus
z is computed for each field point and an interpolated value for OTF at
this focus is sought. Two interpolation schemes have been used. One
uses the fitting polynomials for the focal-shift curves to compute an
interpolated MTF at each of the three available frequencies. Experience
to date has shown that cubic fits for the focal-shift curves are probably
adequate to locate maxima, but that often the actual curves have secondary
maxima and the fitting cubic departs more than one would like from the
true MTF, 0.1 MTF units perhaps in extreme cases. We will call this the
"cubic-fit" interpolation, for short, in the following.

A more satisfactory scheme uses the original OTF data directly; the
original curves whose focus settings bracket the desired focus are located
in the OTF file, and a complete new curve constructed by linear interpolation
between them. We will call this interpolated curve a "TINT" curve, for
short, in the following.

The two interpolated numbers normally agree; when they are different
it may mean that the focal-shift curve had too many inflections for a cubic
or that the original data are lacking in that part of the focus range. In
the latter case both numbers are apt to be nonsense, since neither inter-
polation scheme extrapolates reliably. No problem arises if care is taken
in the original map to cover the whole focus range with adequately spaced
scans.

157

This operation is performed for each field point specified in an "evaluation list" which need not be the same as the list of points which were used to find an optimum plane. For each point, there is one interpolated OTF curve (with real and imaginary parts) for the tangential section, and another for the radial section. The tangential and radial values of the MTF are combined in a geometric mean, at each frequency for which original OTF calculations had been made, in the case of "TINT" curves. Each point is assigned an area weight, in the same fashion as for plane-fitting, and an area-weighted average over the field is made. While covering the field, the computer notes the minimum value of the MTF at any point, and for which image section it occurs (this applies to one frequency).

A particular frequency, from a choice of three, was specified for plane-fitting, and the evaluation report includes the "area-weighted average MTF" for that frequency. Numbers from both interpolation schemes are carried through the program and may be compared at the end, but the cubic-fit numbers will probably be dropped in future. The average MTF is also available at all frequencies,in a table, if asked for.

Besides the geometric mean MTF, the program keeps track of the fractional differences of the tangential and radial values (at one frequency) and averages this as a general measure of astigmatism. The absolute value of the imaginary part of the OTF is also averaged, as a measure of asymmetrical aberration due to coma or vignetting.

158

To guard against nonsense numbers, warning flags are set if negative values, or values greater than 1., occur in the MTF estimates. (This happens when the interpolation procedures are forced to do an extrapolation.) In the detailed output report, which tabulates all the relevant numbers for each field point, the seriousness of such an event can be evaluated. Normally some such events can be tolerated.

(2) *Predicted Photographic Resolution*

These estimates are predicated on the use of film threshold modulation curves[3]. According to Lauroesch et al.[3] the threshold image modulation required for resolution of standard tribar targets of unit contrast can in most cases be well represented by a quadratic formula,

$$TM = a_o + a_1 f^2 .$$

In our program we read in the a_o and a_1 coefficients, and once the processing has reached the stage of reading back one of the original OTF curves, thereby establishing the frequency range and increment for the original data, a threshold modulation table is constructed and its intersection with the interpolated MTF curve (the "TINT" curve) is found, yielding a predicted resolution for that point, radial or tangential section, for that particular film. The radial and tangential values are combined in a geometric mean (again this is based on the prescription of the standard Mil-150A). The fractional difference of the two values is again retained as an astigmatism indicator. If the TM curve does not intersect the TINT curve within the frequency range of the original data, the predicted resolution is set by

default to the original maximum frequency plus one increment, and a warning flag is set.

The program keeps track of the minimum resolution that occurs anywhere in the field, for which field point and which image section.

Area-weighted averages are made of the geometric mean (this corresponds to the familiar AWAR) and also of the astigmatism parameter, and the radial and tangential resolutions separately.

(3)   The O.T.F. Integral

Several image quality criteria derived from the OTF have been proposed[4-6]. Of these we have chosen, for the present, the integral with respect to frequency. Using a one-dimensional representation, if L(x) is the line spread function and T(f) its (complex) Fourier transform, then

$$\int_{-\infty}^{\infty} T(f) \, df \quad = \quad L(0) \quad ,$$

the value of the spread function at its origin, or the gradient of intensity in the edge function at its most steeply rising point. The ratio of this number for the test lens, to its value for an ideal, diffraction-limited lens of the same aperture, is the "Strehl definition", also closely related to Linfoot's "correlation quality" .[5,6]

In the evaluation program, each "TINT" curve is integrated from the origin out to the highest frequency f_{max} for which the original calculations were made (using Simpson's rule and treating OTF as a complex function). The real and imaginary parts are each normalized by the corresponding integral for a diffraction-limited lens of the same aperture. The result is called S, or "OTF integral" in the following.

Averages are made of the real part, and of the absolute value of the imaginary part. The former number is a measure of how well the lens approximates the ideal diffraction behavior over the field, the norm being a value of 1.0 ; and the latter is another kind of measure of spatial phase distortion, the norm being a value of 0. (The imaginary part does not normally enter into the Strehl criterion, except in that the real part, which does enter, is diminished; because it is an odd function and vanishes when the integration includes the negative half of the frequency axis).

A warning flag is set if the real part of S exceeds 1. after normalization, indicating an unreliable OTF curve has occurred.

Other derived functions of the OTF could easily be introduced in the same fashion, since the complete interpolated OTF curves are available at every field point.

(4) Miscellaneous Parameters

The r.m.s. value of the difference between "best-focus" , and the image plane being evaluated, is obtained treating radial and tangential sections as separate points. The r.m.s. difference in best focus between the radial and tangential images is also calculated. This number is independent of the image plane.

161

c. Display

Computer displays are very much a matter of the taste and needs of an individual user, but we will describe our own choices briefly, with a final glossary of the merit parameters which will be illustrated in the next section. The problem in attempting to abstract from several hundred OTF curves is to keep the abstract in reasonable bounds without suppressing useful information. We have chosen to make the evaluation report in several message levels.

If Level 1, the simplest, is chosen, the report consists of some numbers which refer to a single chosen frequency : the area-weighted average MTF, the minimum MTF and its location in the field, and a total count of warning flags; plus the predicted photographic resolution, for each film requested, as an average ≠ "AWAR" ; the minimum resolution, for which field point and which image section it occurs. Coefficients of the image plane used are also reported.

At Level 2, there is added

(a) A table listing by field point all the individual numbers that enter the averages (see Glossary), and the number of warning flags that were set for that point (the reasons for the warnings are apparent upon inspection of the numbers).

(b) Averages of the predicted tangential and radial resolutions, computed separately; and averages of the astigmatism parameters.

(c) The averages of the real part, and the absolute imaginary part, of the OTF integral S.

(d) A complete weighted-average OTF table, listing for each frequency in the original computations (e.g. 0 to 160 c/mm at 10 c/mm increments) the average MTF, and the average absolute imaginary part of the OTF.

At Level 3, intended mainly for diagnostic uses, there is added

(e) A table of best-focus positions from the focal-shift file, that were used in finding the optimum plane, the resulting deviations from the best-fitting plane, and the locations in the disk files of the pertinent focal-shift data.

(f) Some intermediate numbers generated in the plane-fitting process

(g) Complete tables of the TINT curves for all field points, both image sections, all frequencies; and the locations in the OTF file of the original data records, used to make the interpolated curves.

(1) Wavelength as a Parameter

All the above refers to a single color, in the example monochromatic green light. To use the procedure for a realistic spectrum, probably the most practical procedure is to make the original OTF map using the desired spectral blend, by tailoring the light source and detector response spectra. If OTF-mapping is so well automated and fast as to permit repetition of the map for several monochromatic wavelengths, all the quality parameters could become arrays which were combined at the end with suitable weights, additively. Monochromatic mapping has great advantages if one wishes to compare answers with design, or with measurements made in someone else's laboratory. We have not really tackled the spectrum problem in the present stage of the program.

163

What is desirable in more pictorial form again depends on the
user and cumulative experience with such a procedure. The illustrations
in the next section were all prepared manually from printed output;
any of them could have been drawn by the computer, of course, during the
evaluation run, at a cost (in our case) of a few seconds of CPU time
per picture.

d. Glossary of Merit Parameters and Terms

1. *Modulation Transfer Function* , MTF.

May be an interpolated value referring to a particular frequency,
e.g. MTF_{60} ; or a table. It is dimensionless. We refer to its value,
for example 0.307, as so many "MTF units" to avoid the ambiguities of
saying "per cent" . There are MTF values for two image sections:
tangential, referring to target bars or a scanning edge which are tangential
to a circle centered on the optical axis and passing through the field point
in question. (A term "tangential resolution" is sometimes used to mean the
opposite,orthogonal section; our usage seems to conform to most practice.)
For a radial section, the target bars or scanning edge would be parallel
to the radius of the circle mentioned. (Also called the "sagittal" section).

2. *Area-weighted Average MTF*, $\overline{M}$. Average over the field of the geometric
means of the tan, rad MTF values, with each field point weighted by the
area of an annular segment whose bounds are halfway to adjacent field points.
May refer to a particular frequency; or a table.

3. *Minimum MTF* , M_{min} . Refers to the lowest MTF at frequency f_1 (see below) that occurs anywhere in the field. e.g. $M_{min} = 0.12$ at Point 8, Radial.

4. *Absolute value of the imaginary part of the OTF,* $|ImagT|$.

ImagT = MTF sin ϕ where $\phi(f)$ is the phase transfer function. We use it as a measure of the amount of spread function asymmetry, due to coma or perhaps vignetting effects. It can be considered a "penalizing" merit parameter. It seems a more appropriate choice than ϕ since, as the MTF falls toward higher frequencies, random noise in the answers tends to dominate the ratio of real and imaginary parts of the spread function transform, and ϕ values there tend to fluctuate randomly between $\pm 180^{\circ}$. When taking an over-the-field average, the radial and tangential values appear as an arithmetic mean.

5. *Predicted Photographic Resolution* R.

An estimate of the resolution that would be obtained by photographing standard tribar targets of unit contrast, in the image plane being evaluated. It is an intersection of an MTF curve with a "threshold modulation" (TM) curve, the latter approximated here by a quadratic formula whose coefficients are assumed to be known for the film of interest. R is defined for radial and tangential sections. The area-weighted average of the geometric means of the rad, tan values has a well-known acronym "AWAR" . R_{min} is the lowest value that occurs anywhere in the field and refers to either a tangential or a radial section. Units are cycles/millimeter or c/mm.

6. *Astigmatism parameters* , APM, APR. Refer to fractional difference between radial, tangential values of MTF or resolution respectively, e.g.

APM $= \dfrac{MTF(tan) - MTF(rad)}{geometric\ mean}$. APR is analogous, for R.

Averages are taken with the usual area weights.

165

7. *O.T.F. Integral* , S.

As used here it means a normalized, partial integral :

$$S \quad = \quad \frac{1}{S_0} \int_0^{f_{max}} OTF(f) \; df$$

where S_0 is the corresponding integral (same limits) using OTF for a diffraction-limited lens of the same aperture. The real part of S approximates the Strehl criterion, and tends to correlate with the sharpness of edges. The (absolute) imaginary part of S is used as a measure of spread-function asymmetry, and can be considered a penalizing merit parameter. * The units of S_0 are mm^{-1} ; S is dimensionless.

8. *Focus Deviation* , Δ . The root-mean-square value, over the field, of the (unweighted) differences in focus between the image plane being evaluated, and the "best-focus" images for the various field points. Radial and tangential values are treated as independent points. Units are μm.

9. *Image Plane Parameters* .

The plane may be defined by the equation $z = Ax + By + C$ where x,y are coordinates of the field point in units equal to full-field image height; and z is the focus distance normal to the reference plate, positive away from the plate, in μm.

For display, convenient parameters are the axial intersection distance C, the <u>tilt</u> with respect to the reference plate $\tau = (A^2 + B^2)^{\frac{1}{2}} / R_4$ where R_4 is the full field image height in μm ; and the <u>Azimuth</u> of the intersection of the image plane with the reference plate, $\theta_0 = tan^{-1}(A/B)$.

10. *Optimizing Frequency* f_1 . A chosen one of the three previously fixed frequencies used in abstracting original data. "Best-focus" settings used to fit the image plane are those which maximize MTF at this frequency.

---

* (In the example data quoted in the next section the modulus of S is sometimes used, because the program version used at the time computed it rather than the real part which is probably a preferable parameter. In the example there is no significant difference in the values.)

166

The choice of f_1 will influence the answers if the shape of the MTF curves varies with focus such that higher frequencies are best transmitted in one plane and lower frequencies in another plane. (In our example lens, this property is not especially evident).

3. EXAMPLES OF RESULTS

This procedure was tried out on a wide-angle reconnaissance lens, field angle $\pm 40^{\circ}$, f/4.5, focal length 3 inches or 76 mm. It is the same lens used in a previous MTF study[1] and had been extensively measured for MTF in a number of laboratories. For the study it had been equipped with a Reference Plate locating 17 standard field points, arranged in the circular format shown in Fig. 47. To test the evaluation program we made a complete OTF map for all 17 points, in tangential and radial sections, over a focus range of about 0.5 mm. The map contained 554 OTF curves in all. The spectrum was interference-filtered green light at $\lambda 5460 \pm 50$ A. Of particular use in this evaluation was the fact that direct photographic resolution measurements had been carried out for some field points, at the Air Force Avionics Laboratory, (See Ref 1), so that computerized resolution predictions could be compared to some overlapping measurements made in the traditional way. From the lens design data, we had available predicted MTF curves at some focus settings, which agreed well with observation on axis, but which did not agree well with observation, or among competing design programs, at field angles as large as 29°. We hope to obtain in future new calculations, from the original design, of numbers which will be directly comparable with the merit figures that the empirical evaluation procedure yields. For the present we can test the procedure itself by looking for internal
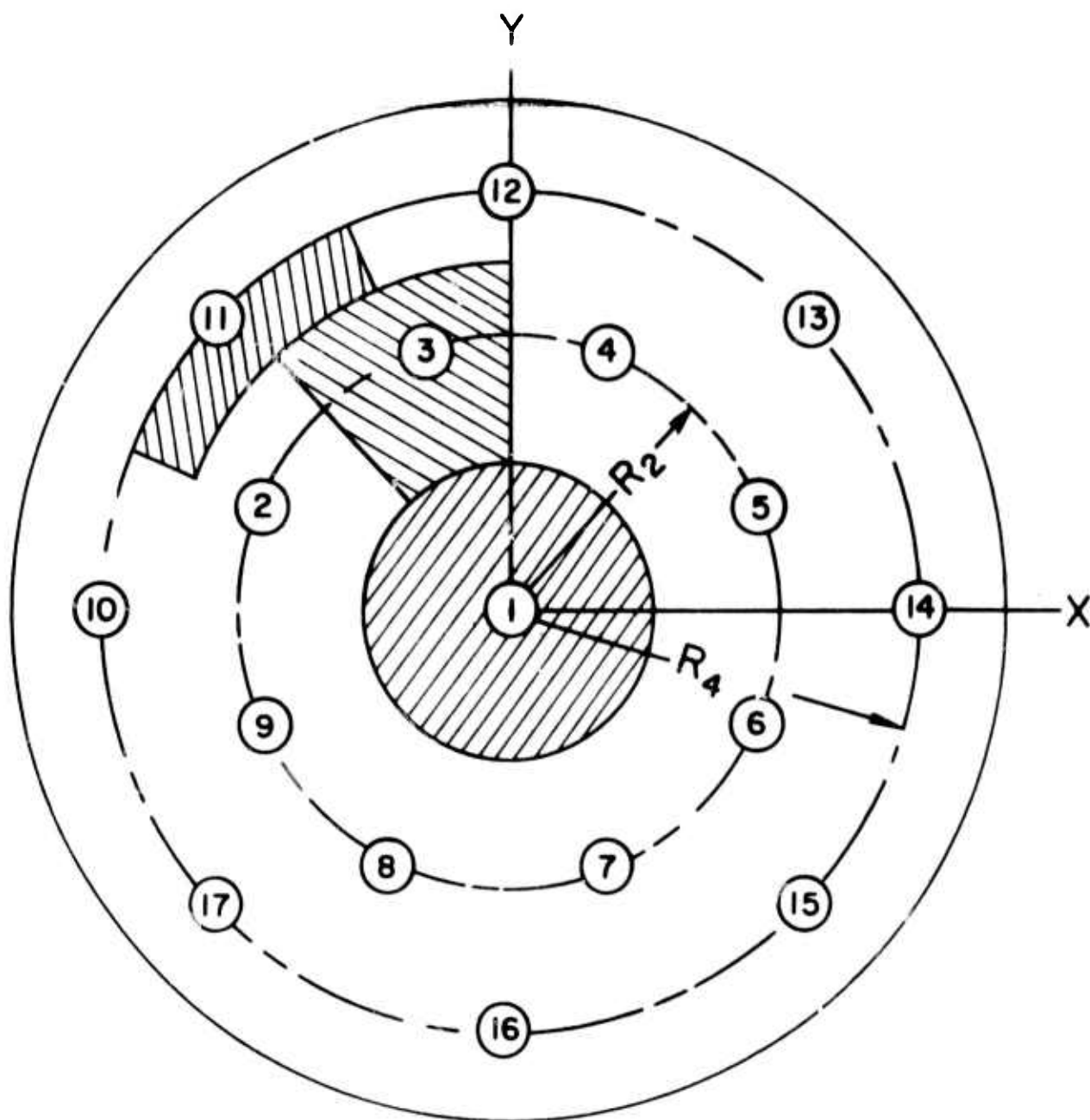
REFERENCE PLATE

Fig. 47. Diagram of the Reference Plate illustrating the labeling scheme for standard field points, and the weighting zones, for the circular format used in the example. For the 3-inch f/4.5 lens, R_4 = 63.5 mm corresponding to 40^0 field angle; R_2 = 42.5mm, at 29^0.

consistency, and begin to acquire experience in interpreting the varieties of information which we hope the evaluation procedure can furnish. There are also interesting departures in behavior from the designer's intentions, most notably variations in image quality around the field at a given field angle.

Our test for internal consistency of the scheme consisted of applying the evaluation program to the complete set of 17 field points and to two interlocking subsets of 9 points each. If azimuthal variations were purely random all three sets of answers should be roughly the same, with their differences measuring the scatter that might be expected in a practical sense. Making this comparison (the numbers are included in Table 1) we note an area-weighted-average MTF (at 60 c/mm) of 0. 22 ± .02, an average predicted photographic resolution (AWAR) of 59 ± 2 c/mm for medium-resolution film A, of 126 ± 8 c/mm for high resolution aerial film B. We would conclude that the procedure is consistent enough to be useful.

When comparing the computer-predicted photographic resolution, the results appear to agree with measurement within limits that are somewhat better than the scatter of the photographic measurements generally, behavior which would seem to make the photoelectric method useful; it has the advantage that once the map is made, the image plane can be moved around and new AWAR numbers obtained quite painlessly. Fig. 51 shows the comparison.

171

TABLE 1.   BEHAVIOR OF SOME MERIT PARAMETERS UNDER VARIATION OF
OPTIMIZING AND EVALUATION OPTIONS, FOR THE 3-INCH f/4.5 LENS

Line A shows the results when a general plane $Z=Ax + By + C$ is fit
to best-focus settings of all 17 field points, and the imagery is evaluated
over the whole field using the same 17 points.

Lines B, C refer to two subsets, interlocking with the full set, of 9
points each. The merit numbers are not substantially different from those of
the full set, indicating the degree of internal consistency in the process.

D - F show effects of preferential focusing for the axial region, for
29° field, and for 40° field respectively. The latter two criteria yield
virtually the same image plane and the same image quality overall.

G shows the slight improvement when an optimally tilted image plane
replaces the best-fitting plane constrained to lie parallel to the reference.
The most significant effect of adding optimum tilt is to improve the worst-
case resolution, for high-resolution film, from 36 to 56 c/mm; this is because
the individual field points show a much higher sensitivity to focus than is
reflected in the overall averages. For further increases in tilt, keeping the
same axial intercept and azimuth, overall quality is seen to drop eventually.
From this kind of comparison one could infer practical tolerances on the tilt
parameter.

H shows the effects of selective focusing for different spatial frequencies.
In the example lens, there is little difference in the best image plane or
in image quality, for a fourfold change in f_1 .

172

TABLE 1

Opt. Freq f_1	Image Plane Axial dist. C	Image Plane Tilt Azimuth τ	Image Plane θ_0	Foc dev RMS Δ	MTF (f_1) $\overline{M}$ Wtd-avg	MTF (f_1) M_{min} Min(Pt)	Pred.Photo. Resol. Film A AWAR	Pred.Photo. Resol. Film A R_{min} Avg Min(Pt)	Pred.Photo. Resol. Film B AWAR	Pred.Photo. Resol. Film B R_{min} Avg Min(Pt)	OTF Integral $\overline{RealS}$ / $\overline{RealP}$	OTF Integral $\overline{ImS}$ / $|\overline{ImagP}|$	Astigmatism MTF $\overline{APM}$	Astigmatism FilmA $\overline{APR}$
c/mm	μm	min	deg	μm	"MTF units"		c/mm				relative to diffr-limit		relative to geom.mean	

A. Using all 17 field points for optimum-plane location and evaluation

| 60 | 228 | 4.8' | -54° | 85 | .224 | .07(16T) | 59 | 38(16T) | 126 | 56(16T) | 0.331 | .038 | -.46 | -.13 |

B. Using the subset, axis + odd-numbered points, for both steps

| 60 | 235 | 5.3' | -54° | 90 | .212 | .09(11T) | 58 | 42(17T) | 122 | 68(17T) | .318 | .032 | -.44 | -.08 |

C. Using the subset, axis + even-numbered points, for both steps

| 60 | 222 | 4.4' | -54° | 85 | .242 | .06(16T) | 61 | 37(16T) | 134 | 54(16T) | .351 | .039 | -.45 | -.17 |

D. Optimizing for the axis only, and evaluating for all 17 points

| 60 | 78 | 0 | none | 189 | .142 | --- | 45 | 18(17T) | --- | 19(17T) | .206 | .023 | | |

E. Optimizing for points 2-9 at 29° field angle, evaluating all 17 points

| 60 | 256 | 4.1' | -59° | 87 | .238 | .08(16T) | 59 | 40(16T) | --- | 64(16T) | .340 | .043 | | |

F. Optimizing for points 10-17 at 40° field, evaluating all 17 points

| 60 | 229 | 5.5' | -51° | 85 | .222 | .08(16T) | 59 | 40(16T) | --- | 61(16T) | .329 | .039 | | |

G. Varying image plane tilt; evaluating all 17 points

60	228	0	---	101	.208	.03(16T)	58	29(17T)	123	36(17T)	.327	.036	-.65	-.19
60	"	4.8'	-54°	85	.224	.07(16T)	59	38(16T)	126	56(16T)	.331	.038	-.46	-.13
60	"	9.6'	"	99	.184	.03(8T)	57	36(17R)	114	39(17R)	.314	.033	-.40	-.07
60	"	14.4'	"	135	.142	---(8T)	51	26(17R)	98	27(17R)	.263	.033	---	-.02

H. Varying the optimizing frequency; using all 17 points

30	240	4.9'	-55°	76	.436	.21(16T)	60	40(16T)	127	60(16T)	.334	.043	-.22	-.16
60	228	4.8'	-54°	85	.224	.07	59	38	126	56	.331	.038	-.46	-.13
120	222	3.6'	-26°	88	.083	.02	59	36(10T)	126	52(17T)	.330	.039	-.82	-.15

173

Apart from testing the reliability of the answers, we would like to illustrate some of the possibilities of such a procedure, in the other examples quoted. The captions of Table 1 and the figures contain most of the discussion of the points we wish to make, but here we may summarize. We can test for field flatness by running the evaluation program with different field-point lists, such as the axis only, the 29° field points only, or the 40° points only. (Table 1). We can explore tolerances on image plane location by asking the program to rack through focus, or to vary the tilt of the image plane. (Table 1, and Fig. 49. We can see what a multiplicity of OTF curves means in terms of the whole field by displaying the weighted-averages of the modulus and the imaginary part (Fig. 48). Behavior of some individual field points with focus is illustrated by Fig. 50. Azimuthal variations of image quality, reflecting centration problems of the ten elements, or glass inhomogeneities, appear in Figs. 52 and 53. Focus shift with spatial frequency can be examined by changing the optimizing frequency (Table 1) although this is of course apparent in the focal-shift curves that come out when the OTF map is being generated.

The practicality of such a procedure depends entirely on the ease with which the OTF map can be made. Anyone who makes MTF measurements regularly with any of a variety of instruments can appreciate the labor of recording five or six hundred OTF curves; however this can become a less crushing burden if the emphasis of the instrument design is put on communication with a computer rather than communication with the

174
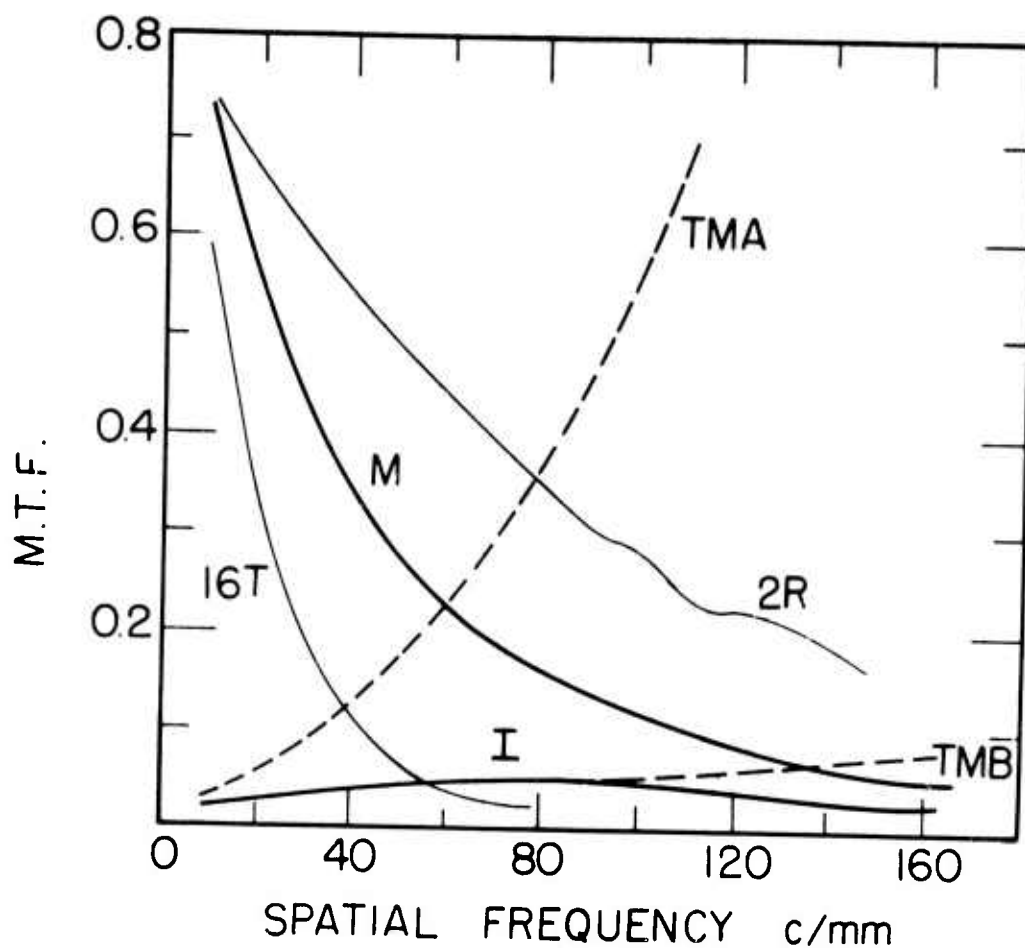
Fig. 48. Overall OTF performance of the 3-inch f/4.5 lens, in the tilted plane optimized for 60 c/mm. Heavy curves show the area-weighted averages of the modulus (curve M) and the absolute imaginary part (curve I). Light curves show the extremes of image quality over the field, with the highest MTF occurring at point 2, radial section; and the lowest at point 16, tangential section. The dashed curves TMA and TMB are the two quadratic threshold modulation curves used in the analysis for predicted photographic resolution.
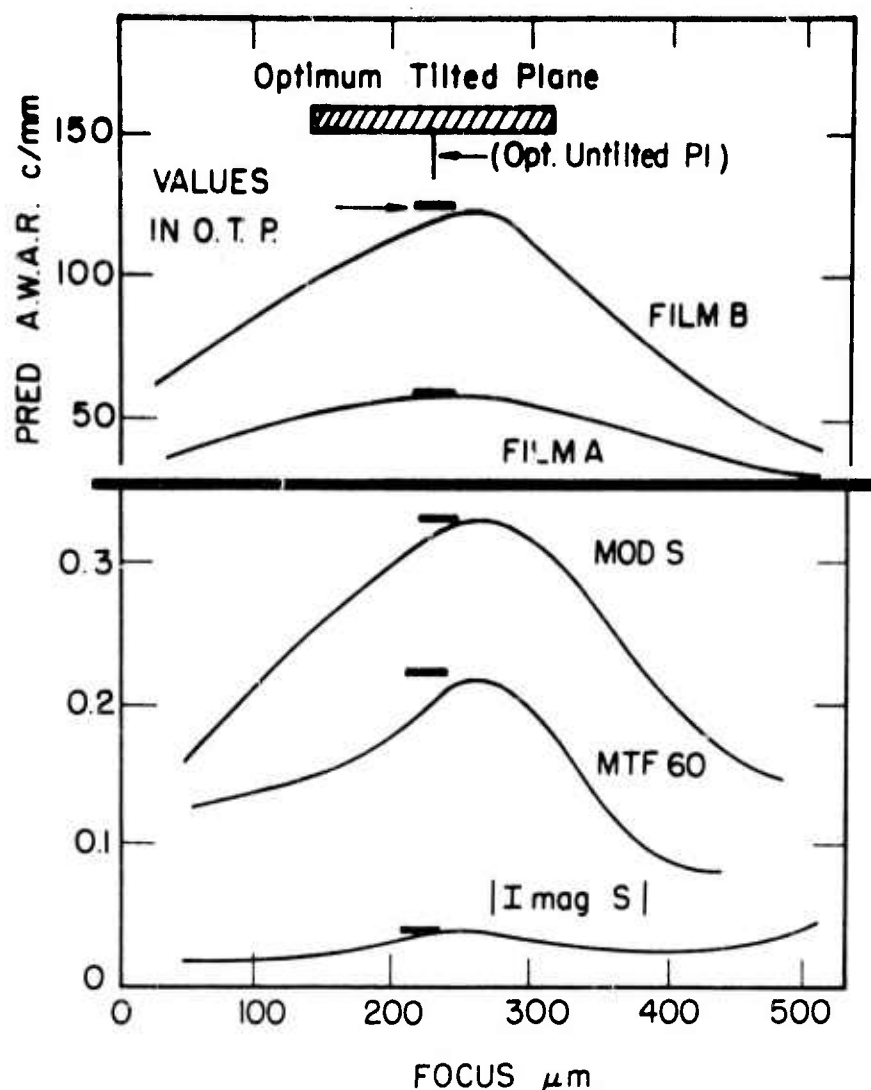
Fig. 49. Behavior of some overall merit parameters as a function of focus. Computations were made for a series of untilted image planes. The values achieved in the plane of optimum tilt (4.8') are shown as horizontal bars. Plane optimization is based on a least-squares fit to positions of best focus, i.e. maximum MTF at 60 c/mm. Note that in this example this criterion yields values of all the merit parameters which are actual maxima, even though there is a slight apparent shift in the focus for maximum and the "optimum untilted-plane" focus. The MTF_{60} curve shown here is derived from direct linear interpolation of original OTF data (see text). The analogous curve derived from polynomial-fit focal-shift curves is not shown here, but it does peak at the "optimum" focus.

At top, the predicted area-weighted average photographic resolution (AWAR) for two films. Film A is Kodak 3401 (PlusX), film B is Kodak 3404 high-resolution aerial film.

Below, the area-weighted average MTF at 60 c/mm, and the average modulus and average absolute imaginary part of the OTF integral S. For this example the modulus and the real part are essentially the same. The real part approximates the Strehl criterion. Compare focus dependence of the area-weighted averages here, with the behavior of individual field points in Fig. 50.

176
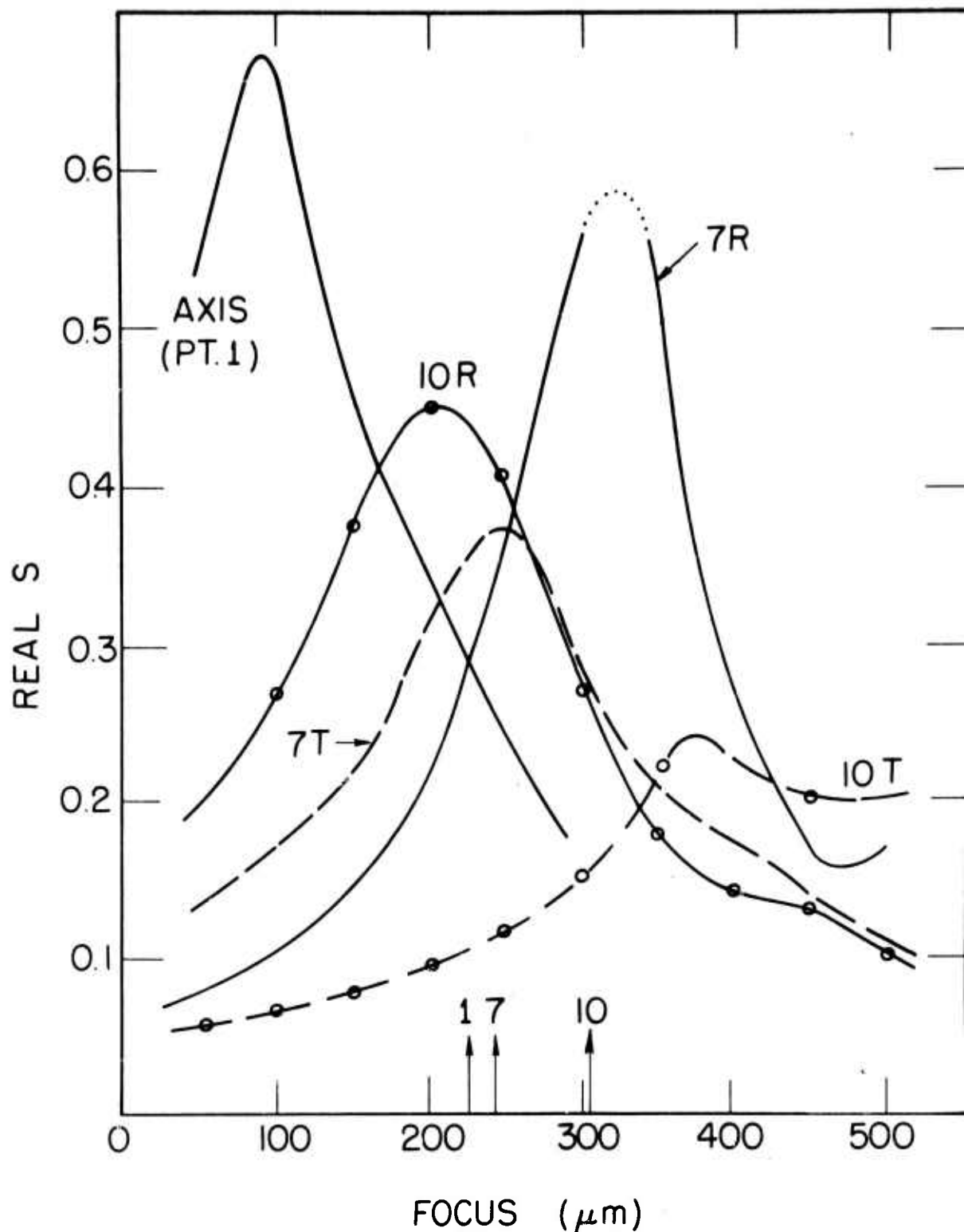
Fig. 50. Behavior of some individual field points as a function of focus. The real part of the OTF integral S is displayed for radial and tangential sections at point 7 (29° field) and point 10 (40°), and for the axis. Location of the optimum tilted image plane, at each point, is shown by vertical bars.
    Plots of the MTF at 60 c/mm would be qualitatively similar to these.

177
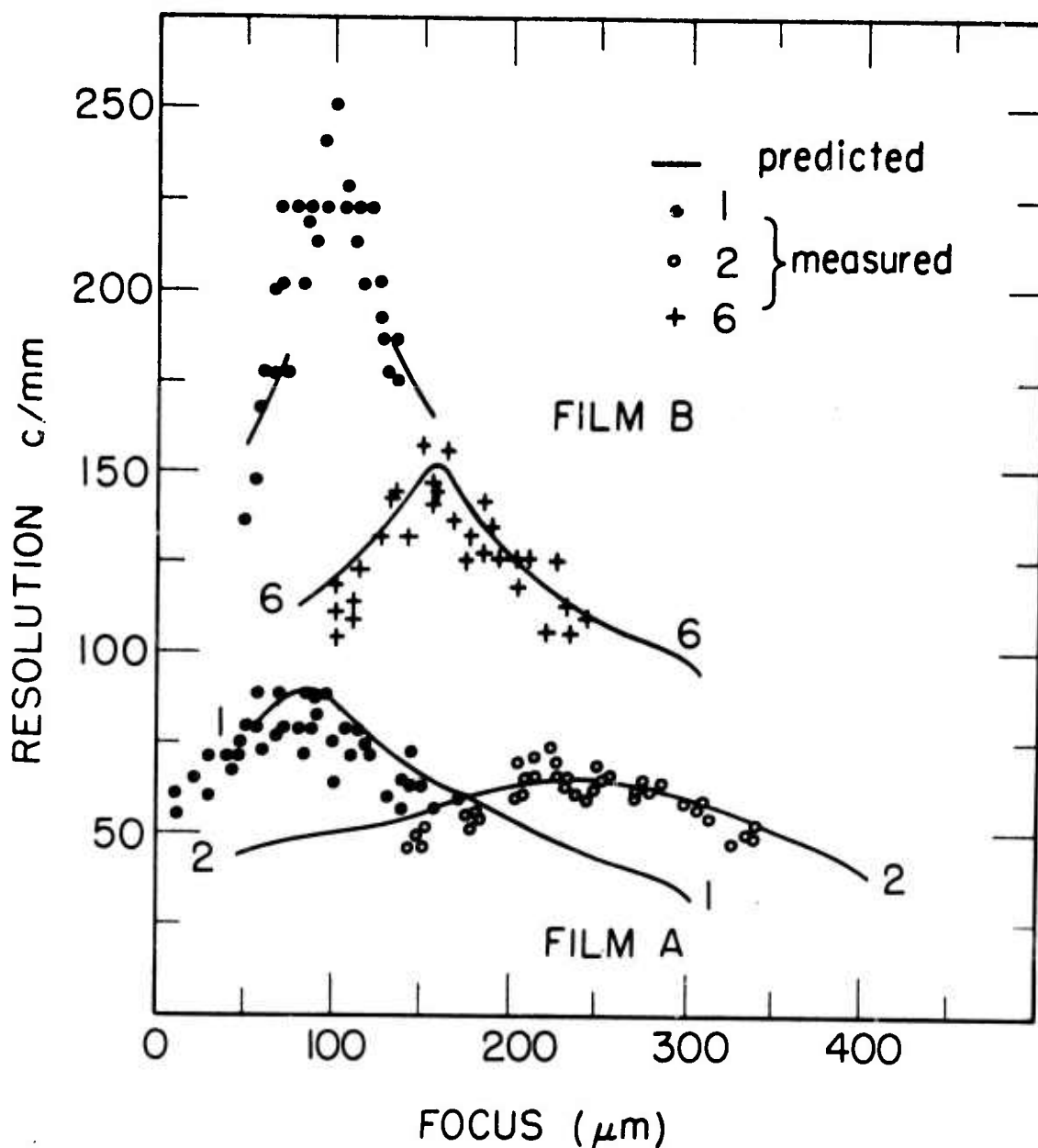
Fig. 51. Comparison of predicted photographic resolution with direct measurements using tribar targets. The measured data were furnished courtesy of Capt. J. van Workum of the Air Force Avionics Laboratory, WPAFB. There is an apparent discrepancy in the absolute focus scales which was compensated in this display by shifting the experimental data for points 2 and 6 by + 50 μm with respect to the axis; the two sets of curves were then registered by aligning the maxima at point 1 (axis). Apart from this metrology problem there is good agreement in the absolute resolution values, and the focus dependence, between prediction and measurement. The prediction analysis used the threshold curves shown in Fig. 48. Predictions could not be made beyond 160 c/mm because the original OTF-map calculations had been carried only to that frequency ; there is no fundamental limitation, except that the random noise in the measured MTF values be not large compared to the threshold value.

Film A is Kodak 3401(PlusX), Film B is Kodak 3404.

178
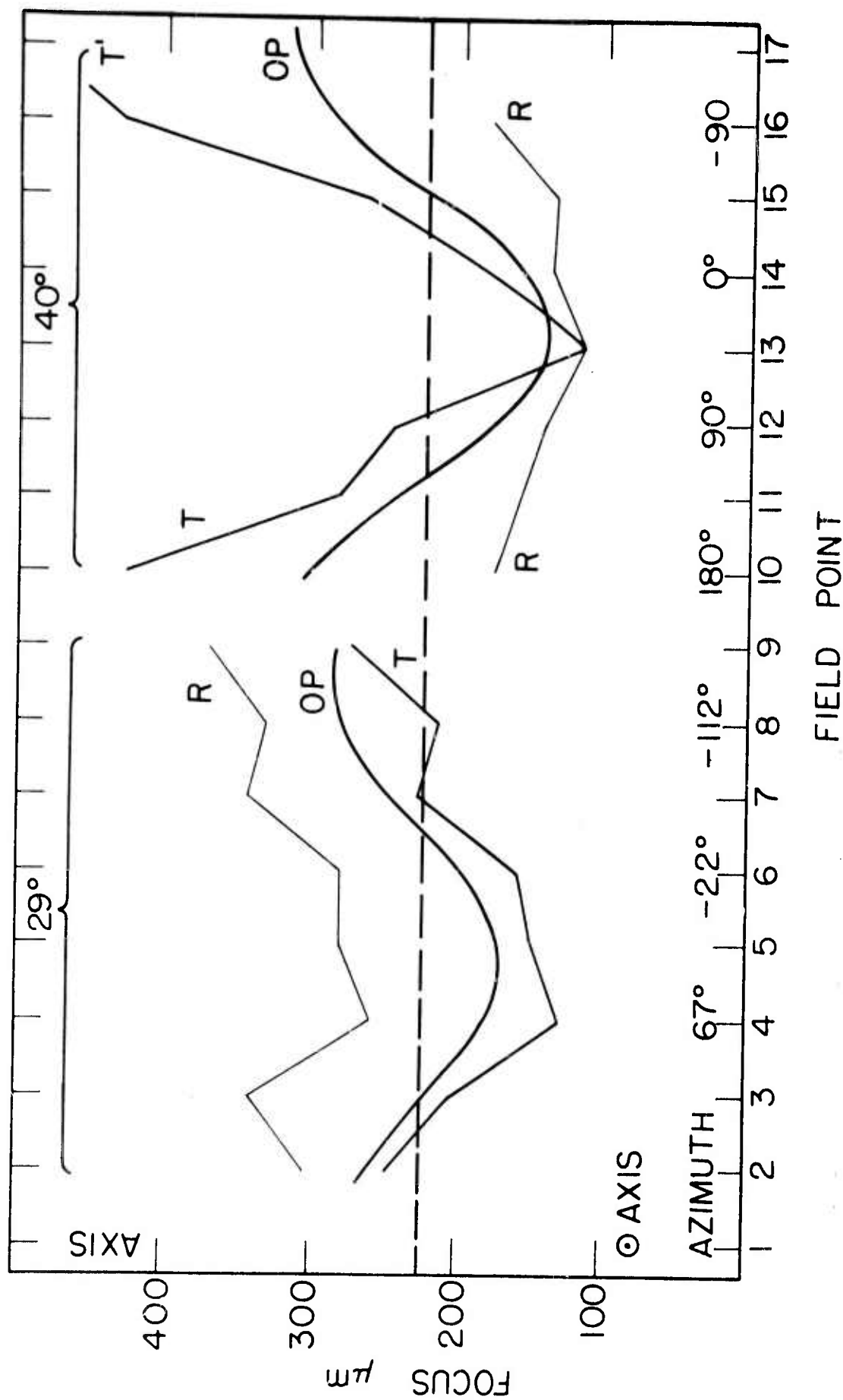
Fig. 52. Azimuthal variations of "best-focus" = focus for maximum MTF at 60 c/mm. The origin of the focus scale is defined as the plane of the reference plate. The untilted plane which is the best fit to all the best-focus positions (each area-weighted) is shown by the horizontal dashed line, and the plane of optimum tilt (4.8') by the smooth curves OP. Note the azimuthal variation of the astigmatic focal shift for the 400 field points. This would not be predicted by the lens design since it indicates a departure from ideal radial symmetry in the actual prototype.

179
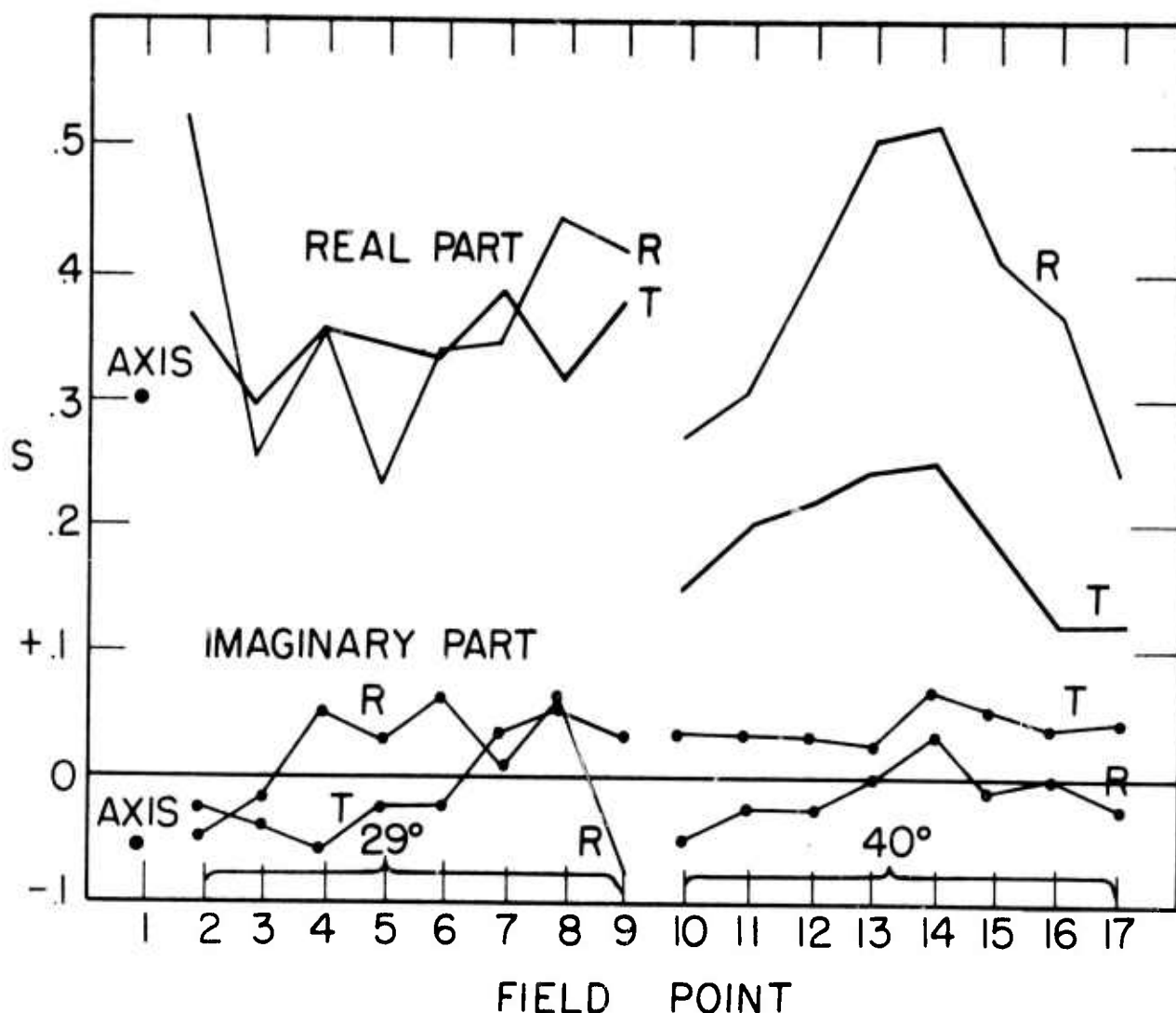
Fig. 53. Azimuthal dependence of the real and imaginary parts of the OTF integral S, evaluated in the optimum tilted image plane. Plots of the OTF at 60 c/mm would be qualitatively similar to these. Note that image quality (what is shown is essentially the Strehl criterion) can vary by a factor of 2 at constant field angle, in this example 3-inch f/4.5 lens; and there are also variations in the amount of astigmatism. A prediction from the lens design would not indicate this kind of variation since the ideal lens is radially symmetric; design values would appear on this diagram as two sets of horizontal lines (for the R and T sections). The configuration of this lens is such that at 40° field the usable beam passes through completely non-overlapping portions of the outer elements, for each azimuthal shift of 45°. Visual inspection of the images shows that when the spread function shrinks, with focus, to an approximate astigmatic line, the line is not usually oriented along either the radial or tangential direction expected from the overall lens, but may be inclined as much as 5 or 10°. This behavior changes with azimuth in no simply describable way, and presumably indicates that there is not a unique optical axis because of residual decentering of the elements.

human operator or consumer of the MTF curve. Operation of any kind of OTF-measuring instrument is basically a repetitious process except for mounting the lens to be tested and (usually) moving from field point to field point. Most such instruments are already elaborate pieces of machinery, in which design refinements to make them more automatic would be only small perturbations to the amount of instrumentation needed. In our own laboratory, for more or less mundane reasons, the automation of the equipment is only partial and its speed has been held down to a human or chart-recorder pace largely for convenience in developing, and debugging the way it works. The map in our example was made at an acquisition rate of about 50 seconds running time per image scan. The digital recording apparatus could easily run six times faster (incremental magnetic tape); the scanning speed could probably be made commensurate with this without encountering new problems with the mechanical design of the scanner mechanism, and the electrical bandwidth used for the present data, 10 Hz, would allow much faster scanning of that particular lens's images without deterioration of the signal/noise ratio set by shot noise of the observing photomultiplier which leads to random errors of the OTF answers. The operator need not intervene for focusing if the observing stage is provided with some stepping mechanism under automatic control. Making coverage of the whole field automatic would open a new set of precision mechanical design problems -- long accurate slides, etc -- so that in our own case we expect to retain operator intervention to change the field point.

If we attempt a conservative extrapolation of the running time

181

that might be needed by our own system, given the minor changes needed to increase its speed to a limit not requiring a new overall instrumentation strategy, we arrive at an estimate of perhaps 10 seconds per scan or two to three hours running time for a full 17-point, one-color map. To this must be added time overhead of mounting the lens and changing the field point, in a fashion comparable to any traditional kind of testing. Existing building-block technology could of course reduce acquisition time much further if the demand for such tests warranted the expense.

In developing this particular procedure we have been conditioned by the ready availability of a large computer (IBM 360/Model 65) although programming ingenuity might well make the use of smaller machines, or some other kind of map storage than random-access disk, feasible. Our original tapes are batch-processed and normally generate complete OTF tables for every scan, plots of the focal-shift curves, and a plot of the "best-focus" OTF curve in each series. The central processor time taken is just under 1 second per scan. We have been using very copious sampling, for convenience in reducing noise effects, and a large core-stored sine,cosine table, rather than a fast-Fourier-transform algorithm, for convenience in interpreting the output; so that faster processing could be done if that were an issue. The evaluation routine typically takes 2 to 2.5 seconds to find and evaluate one image plane, generating printed output only. We do not consider that computer time is an important factor in determining if the procedure is indeed practical.

Conclusion

When contemplating the ease with which an interesting variety of evaluation tasks may be done, once an OTF map exists, and the *extrapolated* estimates of the time and trouble the map might take with proper engineering of the data acquisition system, the procedure appears now to have possibilities for real practical use. We think it is a promising approach to the actual consumption, as opposed to formal display, of OTF-type test data. We would like to suggest that lens-testers consider embracing the idea of taking what seem at first sight staggering amounts of data, with a computer to pre-digest them before an attempt at human assimilation.

REFERENCES

1. R.E.Hopkins and David Dutton, "Lens Test Standardization Study", AFAL TR-70-93 (1970). Also summarized by the same authors in *Optica Acta* 18, 105-121 (1971) and Proc. New York Electro-Optical Design Conf. 1970.

2. Berge Tatian, "Method for Obtaining the Transfer Function from the Edge Response Function", *J.Opt.Soc.Am.* 55, 1014-1019 (1965)

3. Lauroesch,Fulmer,Edinger,Keene,and Kerwick, "Threshold Modulation Curves for Photographic Films", *Applied Optics* 9, 875-887 (1970).

4. K.G.Birch, "A survey of OTF-based criteria used in the specification of image quality", N. P. L., Teddington, England, Report Op.Met. 5, (1969).

5. E.L.O'Neill, *Introduction to Statistical Optics*, Addison Wesley, Reading Mass 1963. pp. 105-109

6. E.H.Linfoot, "Transmission Factors and Optical Design", *J.Opt.Soc.Am.* 46, 740 (1956) .

P R O G R A M   N O T E S

" EVALUE"

A program for evaluating image quality over the field,
using comprehensive stored Optical Transfer Function data.

David Dutton

Introduction

EVALUE is a program written in Fortran IV which processes O.T.F. data presumed accessible in two direct-access files, which were created by another program ("MTFMOD").   Features of the kinds of data and formats, in those files, needed by EVALUE, will be described in these Notes.

The files were created by the Fortran statements:

(1)   DEFINE FILE 9 (600,480, L, K9)   the "OTF file "

(2)   DEFINE FILE 10 (50, 1100, L, K10)   the "focal-shift file" .

The function of EVALUE is to prepare, from the filed data, an analysis of overall image quality in a particular image plane or series of planes. It can locate if desired an "optimum" image plane, one which best matches positions of focus which maximize MTF at a particular frequency. It prepares a report, which may be furnished in three different levels of detail, and which includes area-weighted averages of merit parameters such as the OTF, the predicted photographic resolution, and others, and may include tabulations of the variations of the parameters over the field, up to a complete set of OTF curves interpolated into the image plane being evaluated.

The following notes give a detailed description of the data cards used by the program, and the printed output, with summary comments on the analysis procedure and algorithms used.

I. FIELD FORMAT SPECIFICATION

The field is assumed to be covered by a grid of up to 17 field points. These are numbered 1-17 and the program contains a built-in routine for assigning x,y coordinates and appropriate area weights to each point upon mention of its number. Arrays storing individual-point parameters are dimensioned (17, 2) the 2 referring to two scan sections, tangential and radial/sagittal. In our usage, "tangential" refers to an image scan or MTF in which the scanning edge or slit, or the target lines or bars, are tangential to a circle centered on the optical axis and passing through the field point in question. "Radial" refers to orientation of the scanning edge or target bars which is parallel to the radius of such a circle.

The routine contained in the program is based on a circular format. Use of other formats merely requires replacement of this routine. Assumptions are:

Point 1 is the axis.

Points 2-9 are arranged in a circle, spaced 45° in azimuth, on a radius R_2 = approx. 2/3 of full-field image height

Points 10-17 are spaced at 45° around a circle of radius R_4 = full-field image height.

The location of points in the field is given by X, Y coordinates. These are assigned by the program in units of full-field image height R_4. Point 10 is given coordinates (-1.0, 0) and has an azimuth of 180°. Point numbers increase going around the circle clockwise, so point 11 has coordinates (-.71, +.71) and azimuth 135°, for example. Point 2 has coordinates (-0.62, +0.26) and azimuth 157.5^o; and so on. The particular coordinates used are apparent in output only in the most detailed report level. Any of the internally generated (x,y) coordinates may be replaced at run time by new values on data cards.

Weighting zones are separated by circles : for the axial zone, a circle of radius R_1 = ½ R_2 ; between R_2 and R_4 a circle of radius R_3 = ½ (R_2 + R_4). At run time, the field points to be used are specified in a list. The program counts the number of off-axis points in each ring

(lying on R_2, or on R_4) that actually appear in the list and divides the appropriate annular zone into as many equal segments. The weight assigned is the ratio of the area of the annular segment to the unit circle area (radius R_4). Weighting is optional when finding a best image plane, and automatic when performing the evaluation. There is no provision for changing the weighting scheme via data cards. (The weighting rules are based on the prescription for making area-weighted averages in standard Mil-150A).

When finding an optimum image plane, tangential and radial sections are treated as independent points. Data from the two sections are usually combined by some rule in the evaluation phase; details are given in the following.

II. DATA CARDS

Card 1.   (NTOT, JF, IFIT, IWT, IA, IB, UNIT, NAMEU, IFR(3), IAXIM,
          LAMBDA, FNUM, FOLEN)

Format   (6I3, 1x, F10.3, A4, 1X, 3I3, 2I4, 2F8.3)

NTOT   specifies the number of field points in a list to follow,
       which will be used in finding an optimum image plane;   or
       alternative options :
          If NTOT = + n (n = 1 ... 17) the following n cards will
       each specify one point in the list.
          If NTOT = -1, the following data card will specify three
       coefficients defining an image plane to be used in the evaluation.
          If NTOT = -2, the following data card will specify initial
       and final values, and an increment, for C and the evaluation will
       be repeated for a series of planes z = C .

JF   specifies which one of three previously chosen frequencies
       (JF = 1 ... 3) will be used for optimum-plane location and
       evaluation. If JF = 4, the process will be repeated for all
       three frequencies in succession. Default if blank is JF = 2 .

IFIT   specifies constraints on the optimum plane.
       If IFIT = 1 , the plane will be constrained to zero tilt with
       respect to the reference coordinate system, i.e. the plane z= C.
       If IFIT = 2, the fitting plane will be z = Ax + By + C.
       If IFIT = 3, both choices will be used in succession.
          Default if blank is IFIT = 2.

IWT   specifies whether weights are to be used in the plane-fitting.
       IWT = 1 or blank, no weights
       IWT = 2, weights assigned by zone areas.

189

IA   specifies the level of output information. IA = 1 ... 3
         gives message level 1 .. . 3 (see Output description).

IB
__   spare parameter not used in this version. Normally blank.

UNIT   A floating-point number giving the value, in inches, millimeters,
         or microns, of full-field image height, the normal unit of the
         x,y coordinate system. Must be included.

NAMEU   The name of the unit in which UNIT is expressed, 4 characters
         which must be one of the following : "____" (4 blanks); "INCH" ;
         "MM__" ; or "MUM_" . If blank, millimeters is assumed. If any
         other spelling is used, the normal unit will be given a default
         value of 1.0 mm.

IFR(3)   Integers specifying initial values for the three frequencies
         on which focal-shift curves are based, one of which is opted by
         parameter JF. Values read from the card are replaced by filed
         values as soon as one record from the files has been read. Blanks
         are set to default values 30, 60, and 120 c/mm.

IAXIM   The integer number in microns at which best focus occurs on
         axis. The number is used only in the output display, and then
         only if the axial point was not included in either field-point
         list, in which case it is replaced by the filed value. Blank
         treated as 0.

LAMBDA   Integer wavelength in Angstroms which will be used in computing
         cut-off frequency etc. associated with an ideal lens. Must be
         included.

FNUM   The f/number of the test lens. Must be included.

FOLEN   The focal length of the test lens, as measured in the same units
         in which UNIT was expressed, i.e. inches, mm, or μm . Must be included.

Card 2. /a/ if NTOT > 0 : (NPTT(I), NDD(J,I),J=1,2; CRR(J,I),J=1,2 ;

                                     CC(J,I),J=1,2)   all for I = 1 .

    <u>Format</u> : (3I3, 4F10.3)

<u>NPTT(I)</u>   The number of the field point, 1 ... 17 .

<u>NDD(1,I)</u> A replacement of the index value for the record number in
the focal-shift file which carries data for the tangential scan
of point NPTT. If blank, the original indexed value is used.
If = 999, focus data to follow in the card will be used instead
of filed data. The NDD value given on the card, if not blank,
0, or 999, will permanently replace the original value in the
filed index (located in record 1 of the focal-shift file).

<u>NDD(2,I)</u> The corresponding index correction for the radial scan.

<u>CRR(1,I)</u> Floating-point number which will be used as an additive
correction to the filed value of best-focus setting for the
tangential scan of point NPTT. If NDD was 999, the value
will be used instead of the filed number. Blank taken as 0.

<u>CRR(2,I)</u> Corresponding focus correction for the radial image section.

<u>CC(1,I)</u>   If not blank or 0, replaces the pre-assumed value for the <u>X</u>
coordinate of field point NPTT.

<u>CC(2,I)</u>   Replaces the pre-assumed value for the <u>Y</u> coordinate.

<u>NOTE</u>   Normally all the above parameters are blank except NPTT.

    This card is followed by analogous cards specifying the entire
list (up to n cards, 17 maximum) of field points to be used in
optimum-plane location.

Card 2. /b/ if NTOT=-1 :   (PC(J), J=1,3)

Format :   (3F10.3)

PC(1)   Floating-point number, in microns per normal unit, to be
used as coefficient A in the image plane z = Ax + By + C.

PC(2)   B, above; microns per normal unit.

PC(3)   C, above, microns.

Card 2. /c/ if NTOT=-2 :   (ZSTART,ZSTOP,ZINC)

ZSTART   Initial value of C

ZSTOP   Final value of C

ZINC   Increment of C

Evaluation will be carried out successively in the series of
untilted image planes z = C.

This completes the data card set for the image-plane-fitting phase.

Card j.   (JPT(I), I= 1, m)

Format   (17I3)

JPT   the list of field points, up to 17, to be used in the evaluation
step, for the image plane specified by previous cards. This list
need not be the same as the NPTT list.

This card must be included, but may be blank if a plane location
only, and not an evaluation, is desired.

Card j + 1.   (NAFILM(I), CT(I), AT(I), I = 1,3)

Format :   (3(1X, A4, F6.3, E10.3))

NAFILM   4 characters denoting name or type of film, to be used in
output display. Data for up to 3 films may be given on this card.

CT   Coefficient C in the formula $TM = C + A f^2$ to be used
in computing a threshold modulation curve for film NAFILM.
CT is in "MTF units" .

AT   Coefficient A for the formula above.   MTF-units per (mm^{-2}).

NOTE: The card must be included if previous card is not blank. If
this card is blank, no photo. resolution computations will be made.

192

III. FINDING THE OPTIMUM PLANE

This segment of the program constructs a table of best-focus
settings versus x and y coordinates of the field point and fits a least-
squares plane.   If the CRR entry on the point-specifying data card was
blank, the focus value taken is the maximum of the cubic which best fits
the focal-shift curve for frequency JF. (The cubic fit was performed
during original processing of the filed data, and the z-value for the
maximum is filed in array CF(8, JF)). The focal-shift file record
consulted will be the one indexed by that point number in record 1 of
that file, unless overridden by the NDD parameter at run time. IF
CRR was not blank, CRR will be added to the filed value; or if NDD was 999,
will replace the filed value for purposes of the fit (not permanently).

Tangential and radial image sections are treated as separate points,
each with an appropriate zone-area weight, when IWT=2.

A least-squares fit to the plane z = C is merely a weighted average
of the focus numbers and is done within the main program. The tilted-
plane fit z = Ax + By + C is done in a subroutine, "PLFIT" , which in
turn calls a library subroutine MATEQ to solve the set of 3 normal equations.
Which fit, and how weighted, is controlled by IFIT and IWT on Data Card 1.
The C coefficient is the same for both planes, but if only untilted planes
are of interest PLFIT and MATEQ may be dispensed with (use dummy PLFIT).
PLFIT has one argument which controls printing of one line displaying the
plane coefficients and the residual rms error. (IOUT=1, print; other values,
no print). PLFIT also prints the matrix of the normal equations when output
level parameter IA = 3.

Focus - coordinates tables and plane coefficients are transmitted in
the common block /PFIT/ .

The main program outputs the coefficients A, B, C, and also the "Tilt"
of the plane $\tau = \tan^{-1}\{ A^2 + B^2 \}^{\frac{1}{2}}$ / (UNIT in μm) , and the azimuth of its
intersection with the XY plane, $\theta_o = \tan^{-1} (A/B)$.

For the NTOT= -1, or -2 options, this segment is bypassed and the image
plane to be evaluated taken from data cards.

193

IV. EVALUATION OF IMAGE QUALITY IN A PLANE

For plane-finding, a particular frequency "JF" was chosen, also called f_1. When a frequency argument is implied below, it is frequency f_1.

Evaluation is done for a list of field points as given in data card _j_. This list need not be the same as the plane-fitting list. Data are recovered from the files in the order that points are mentioned in the list; weights are assigned according to point number only and may not be altered at run time.

First, x,y coordinates are assigned from the built-in table and a z value computed for the point from the plane coefficients A,B,C.

MTF values are obtained for that focus value by interpolation, by two different schemes. (1) The cubic-fit coefficients for the focal shift curve at frequency f_1 are obtained from the focal-shift file by consulting the index for that field point number, and MTF at frequency f_1 computed from them. (2) The focus-shift file tabulates record numbers of original OTF records vs. focus; this table is scanned to find the original records which bracket the desired z value, and a new OTF curve constructed by linear interpolation between them. This is done for MTF and for phase angle. If the z value falls outside the range of the original focus series, an extrapolation is made using the last pair of original OTF curves.

Both schemes tend to produce nonsense numbers when forced to extrapolate, hence each MTF estimate is tested and warning flags set if the number is greater than 1. or if it is negative. Actual focal-shift curves sometimes have secondary maxima; in such cases the cubic fit does not approximate the whole curve well (errors of order 0.1 MTF units) although the maximum of the cubic seems to be an adequate representation of the location of the actual principal maximum. "Minimum MTF' analysis is based on the cubic-fit interpolation at frequency f_1. Both interpolated numbers are carried through the program. From present experience it is felt that the linear interpolation is preferable and in future versions the cubic-fit number may be dropped. The linear-interpolation MTF is computed at all frequencies

194

in the original tables, namely at a frequency spacing FINT out to a maximum frequency FMAX. The interpolated MTF is called "TINT" and from it and the interpolated phase angle a complex function OTF is constructed. (Real is MTF cos ϕ, imaginary MTF sinϕ).

The first record consulted in the OTF file supplies FINT and FMAX. It is essential that the entire OTF map be made using the same values of these parameters as the Evalue program does not test them at each OTF file record. If this is not true for the map, special routines must be written and added to EVALUE.

For each point there results an interpolated OTF (value at f_1, or table)for the tangential section, and for the radial section. If data for neither section was locatable, values remain at a large default setting which will cause the point to be skipped in averages; if data for one section only were found, MTF for the other section is set equal to the one found. Negative estimates are replaced by 0.001 for averaging.

For averaging, the geometric mean of the tan,rad values is taken. Each tan and rad value is compared with an absolute minimum value and the point number and scan section noted for lowest MTF over the field.

Prediction of photographic resolution.

When FINT and FMAX are known, a threshold modulation table is constructed for each film (1 to 3 films) for which the quadratic coefficients were supplied on a data card. Intersection of this table with the TINT curve is found (with a linear interpolation formula used between frequency points, for both curves). If there is no intersection out to FMAX, the predicted resolution is set by default to FMAX + FINT and a warning flag set. Note that if the original measurements do not extend far enough in frequency (until MTF has dropped below the level of "C_{film}" MTF units), the net result will be an underestimate of resolution.

OTF Integral.

The complex OTF derived from TINT is integrated from zero frequency to FMAX using Simpson's rule with increment FINT, and the result called

$$\text{(complex)} \quad \text{CSUM} = \int_0^{fmax} \text{OTF}(f) \, df$$

A normalized value is CNORM(JD) = CSUM/SPART where JD=1,2 refers to tangential, radial sections, and SPART is the analogous integral when OTF is replaced by $T_o(f)$, the OTF of a diffraction-limited lens of the same

195

f/number. This integration is done from the analytic form :

$$\text{SPART} = \int_0^{fmax} T_0(f) \, df = \frac{4}{3\pi}f_c - \frac{2}{\pi}f_c \left(\sin\beta - \beta\cos\beta - \frac{\sin^3\beta}{3} \right)$$

where f_c = cutoff frequency = $\frac{1}{\lambda F\#}$

$\beta = \cos^{-1}(f_{max}/f_c)$.

The units of SPART are mm^{-1} . The real and imaginary parts of CNORM, the normalized (partial) integral, are displayed under the names SREAL and SIMAG. Overall area-weighted averages are made of the real part (in version 3, the modulus); and the absolute value of the imaginary part. A warning flag is set if the computed value of SREAL exceeds 1.0, indicating an unreliable OTF curve, and the point is skipped in the averages. Averaging uses the arithmetic mean, in effect, of the tan, rad sections.

Miscellaneous

As measures of astigmatism, the program takes note of the following: best-focus positions (focus which maximizes MTF at frequency f_1) for the tangential, and for the radial image sections, are compared to get the root-mean-square value (over the field) of their difference. This number is independent of the image plane. The rad, tan values tor MTF, and for predicted photographic resolution, appear in the parameters :

$$\text{APM} = \frac{\text{tangential MTF} - \text{radial MTF}}{\text{geometric mean MTF}}$$ and APR = analogue for Resolution.

APM has the name TAST in an output table.

TEST = difference (geometric mean MTF derived via linear interpolation)
- (geom. mean MTF derived via cubic-fit interpolation).

If TEST is "large" it means that the focal-shift curve displayed too many inflections to be fit well by a cubic; or that one or both numbers result from an extrapolation and hence may be nonsense.

Spatial phase shift indicates that the spread function is not symmetric about its origin. An origin may be chosen anywhere and if not located at the center of an otherwise symmetric function the resulting phase angle will vary linearly with frequency, a physically trivial case. The MTF program MTFMOD chooses an origin at the centroid of intensity of the spread

196

function and hence eliminates any linear-with-frequency phase shift that does not arise from actual asymmetry of the spread function. The phase angle is experimentally determined from the ratio of real and imaginary parts of the computed OTF. Noise in the input data (for example shot noise of the photocurrent which denotes intensity in the spread function, perhaps vibrations in the measuring apparatus also) is reflected in random noise in the answers, and as the MTF becomes small, of the same order as the random noise, the computed phase angle becomes a random number perhaps of order $\pm \pi$. In this program we wished to have some merit parameter which reflected spread-function asymmetry, and have chosen the imaginary part of the OTF, or its integral, because such a measure weights the spatial phase shift by the MTF and hence damps out wild noisy fluctuations shown by the phase angle alone.

Some further details of the computing strategy will be mentioned in the glossary of printed output which follows.

V. GUIDE TO PRINTED OUTPUT

The evaluation report is given at three message levels under control of parameter IA as read in at run time. This version does not produce plotted or other graphic output.

1. (Level 1) NDEX. Contents of the array NDEX as read from record 1 of File 10, the focal-shift file, at the beginning of the run. NDEX(I,JD) = record number for point I, tangential in JD=1, radial in JD=2.

2. (Level 1) DATA CHECK. Parameters from Data Card 1 as read, plus computed values of the cut-off frequency for a diffraction-limited lens (circular aperture) of the same f/number. $f_c = 1/\lambda F\#$; and field angles corresponding to image height $R_2 = 2/3$ UNIT $= H$, and $R_4 =$ UNIT. Angle $= \tan^{-1}$ (H/FOLEN) .

3. (Level 1) FREQUENCY. On its first appearance, the value on card 1 in IFR for the choice of JF on card 1; afterwards, the value obtained from the pre-stored data files. This is the frequency for which an optimum plane will be chosen, and is the frequency argument of the average MTF quoted later.

4. (Level 3) A listing, for each scan section of each point on the plane-fitting list, of : (a) the record number in the focal-shift file being used for data; (b) the original filed best-focus setting, and the correction if any supplied on the data card for that point; suppressed at levels 1,2 except for the message "No data filed for point ... , ... scan" .

5. (Level 3) CHECK ZONE AREAS. Normalized areas of the three annular zones that will be used for weighting, and counts of the number of points in each zone. (The two scan sections counted as 2 points).

6. (Level 3) Matrix of the normal equations used in PLFIT and transmitted to MATEQ.

7. (Level 1) PLFIT. total count of fitting points, fitting plane coefficients, rms deviation from the resulting plane, and sum of the weighting factors used. Printed by PLFIT when called by CALL PLFIT(1).

8. (Level 1) Summary of plane-fit results : coefficients, tilt angle, azimuth angle. A,B coefficients expressed in microns of focal shift per normal x,y unit; C in microns. "AXIM=" the best-focus setting for the axial point 1, as obtained from the files, if point 1 was included in the plane-fitting list; from data card 1 if it was not included.

9. (Level 3) Listing, by field point and scan section, of the x,y coordinates being used for the points; the weight of each; the observed best focus (as filed, or corrected); the focus value computed from the optimum plane; and the difference of the last two numbers.

(End of plane-finding segment)
----

10. (Level 1) Coefficients for the plane being used in the evaluation to follow.

11. (Level 2) Table listing by field point the following :

Point number
WT = zone-area weight being used in the averages
FOCUS = location of the image plane at that point
GMMTF = geometric mean ⎫
TTAN = tangential   ⎬ MTF   as derived from cubic-fit interpolation.
TRAD = radial   ⎭
TEST = (geom.mean MTF from TINT curves) - (geom.mean MTF from cubic fit)
SREAL = real part   ⎫ of the normalized OTF integral, for
SIMAG = imaginary part ⎭   tangential and radial sections.
TAST = fractional difference of TTAN and TRAD above (rel. to geom mean.)
FD = focus difference, in microns, between the best tangential image
     and the best radial image. If positive, the tan image occurs further
     from the lens.
RTN = predicted photographic resolution for tangential target bars, c/mm
RRD = same for radial bars
GMR = geometric mean of these
RAST = astigmatism paramater analogous to TAST = (RTN-RRD)/GMR.
 ... all the above for film "Name" as in NAFILM array.

WARN n. Count for this point of warnings, incremented by 1 when :
    (a) TTAN or TRAD is negative (set to 0.001 in avgs.)
    (b) TTAN. GE. 1.
    (c) TRAD. GE . 1.
    (d) SREAL. GT. 1.
    (e) RTN exceeds FMAX, hence set to FMAX + FINT
    (f) RRD exceeds FMAX, hence set to FMAX + FINT

199

12. AREA WEIGHTED AVERAGES. " m " WARNINGS.

    m is the total count of warnings issued as above.

(a) (Level 1) AVG. MTF. NOTE 1. = area-weighted average of GMMTF, above.

(b) (Level 1) MINIMUM MTF = ... at POINT ..., ...SECTION. Absolute
    minimum of TTAN or TRAD, and where it occurs.

(c) (Level 2) AVG. MTF. NOTE 3. area-weighted average of the MTF at
    frequency f_1, as derived from TINT curves. (In case of discrepancy
    this number is probably to be preferred over MTF NOTE 1).

(d) (Level 1) PREDICTED PHOTOGRAPHIC RESOLUTION FOR FILM name =
    area-weighted average of GMR above.

(e) (Level 1) MINIMUM RESOLUTION AT POINT ... , ... SCAN

(f) (Level 2) AVG TAN RESOL = weighted average of RTN above;
    AVG RAD RESOL = average of RRD, ASTIG.PARAMETER = weighted average
    of RAST.

13. (Level 2) RMS deviation of the best-focus images from the plane
    being evaluated; and the RMS value of the astigmatic focal difference.

14. (Level 2) Weighted-average real part of the normalized OTF integral
    S; the value of FMAX; and the value in mm^{-1} of the normalizing
    integral for an ideal lens, SPART.

15. (Level 2) Average of the absolute value of the imaginary part of
    the OTF integral; the maximum (absolute) value of the imaginary
    part, over the field; and where the maximum occurs.

16. (Level 2) Complete table, at frequency intervals FINT out to FMAX,
    of the area-weighted averages of (a) the MTF as derived from TINT
    curves; (b) the absolute imaginary part of the OTF derived from
    TINT curves and similarly interpolated phase shift data.

17. NOTES.   Displayed at Level 3 only.

18. (Level 3) Complete display of all TINT and interpolated-phase-shift
    data, at intervals FINT out to FMAX, for both tangential and radial
    sections, in the image plane being evaluated. The line labeled
    "FILE9" gives the record numbers, in the OTF file, of the pairs of
    original OTF curves from which the interpolations were made.

19. (Level 1) Film threshold data, as read in from data card j+1 ;
and tables of the threshold modulation curves as used to
predict the photographic resolution.

20. NDEX.   Contents of this array as it will be re-written on record 1
of File 10, including any permanent modifications that have been
introduced on data cards during this run. Also IST10, the starting
record number for future new records to be inserted on File 10,
rewritten from its original value.

End of output. Items 2 - 19 repeated upon iteration with new plane coeffs.

VI. SOME PARAMETERS RELEVANT TO USE ON IBM 360/ Model 65 COMPUTER

(a) REGION : 90K bytes (hex)
(b) Execution time for load module stored on disk : CPU, 2 to 3 sec
    I/O, 4 to 6 sec. (Full map of 17 points, level 3 output).
(c) Compile time for Fortran source program, level G : about 25 sec.

(d) The program calls one library subroutine (MATEQ) from the U. of
    Rochester Computing Center library. It solves the set of 3
    normal equations developed in PLFIT and may be replaced by an
    equivalent library routine upon modification of the subroutine
    PLFIT, which is part of the EVALUE source package. There are
    no other subroutines except the standard Fortran library as
    supplied by the computer manufacturer.

FINAL NOTE. This version treats one color, that for which the original
map was made. For use with multicolor maps, it is suggested that all
the merit-parameter arrays be given one more dimension = the number
of colors, and combined at the end additively with appropriate weights.

B. THE USE OF SMALL COMPUTERS IN THE OPTICAL TESTING LABORATORY

Douglas C. Sinclair

We have begun studying the potential uses of small computers in the optical testing laboratory. The purpose of the investigation has been to determine ways in which small computers can be used to improve optical testing technology.

The original motivation for the study arose from the realization that the complete OTF testing of completed objectives involved accumulating large amounts of data, and that to obtain reliable measurements, it was desirable to eliminate, or at least reduce, the amount of human interaction with the experimental apparatus (the tedium of repetitive measurements increases the probability of human error). Our initial conception was thus to automate the data-taking parts of the knife-edge scanning equipment developed by Dutton. The system which we envisioned is illustrated in Figure 54. The computer would be used to control the starting and stopping of the knife-edge, the turning on and off of the tape recorder and detectors, and the focusing of the relay optics.

As time progressed, however, it became apparent that our estimates of the usefulness of small computers in the testing laboratory were too modest, and that the possible uses of small computers are much more extensive than we
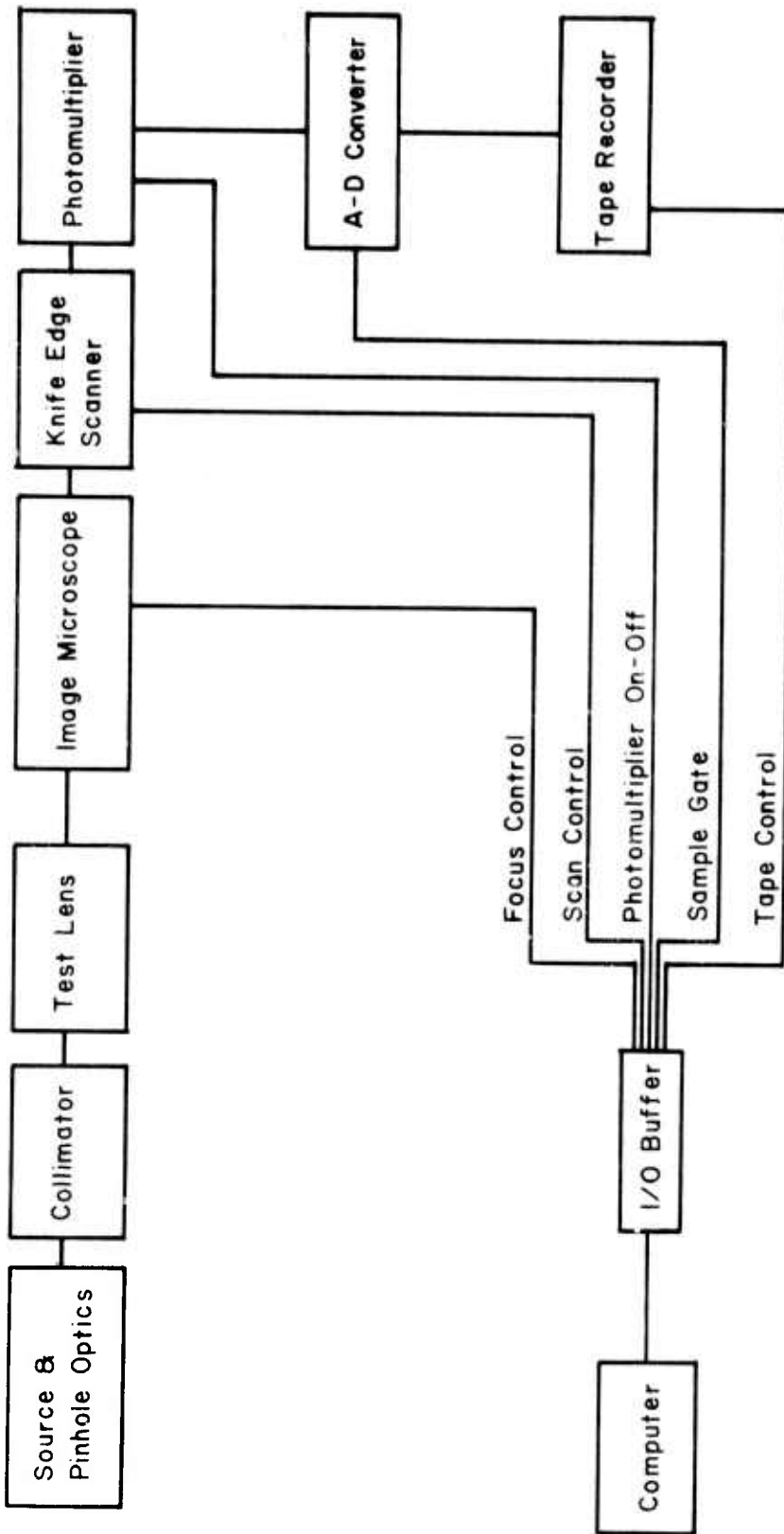
Figure 54 Computer System for Control
Of Knife-Edge Scanner

had originally anticipated. (In fact, many of the objectives of our initially-conceived system have since been implemented by a commercial supplier of optical testing equipment).

It appears, at this point, that small computers will be used to perform four essential tasks in the optical testing laboratory:

1) Control of data acquisition equipment, such as the knife-edge scanning apparatus described above.

2) Signal processing of photoelectric data acquired from optical testing equipment; for example, the conversion of edge trace data to spread functions and OTF data.

3) Manipulation of processed data for optimum presentation; for example, the combination of a number of OTF data to compute area-weighted average MTF. It is in this area that the small computer appears to have its greatest potential.

4) Storage of reference material. For example, the nominal performance data for a given system could be stored on magnetic tape for comparison with measured data in the computer.

During our study of the uses of computers in the
testing laboratory, we have considered a variety of
apparatus in addition to the knife-edge scanner. One
device which we are currently investigating and which
looks particularly interesting combines a small computer
with a rotating Ronchi ruling to produce an "ac grating
interferometer."

The optical apparatus is shown in Figure 55. A
radial grating is mounted on a motor shaft, which rotates
at a fairly slow speed, so that approximately 1000 grooves
per second pass by a stationary point near the rim. The
grating is illuminated from behind, through a diffusing
screen, in the usual manner for a Ronchi ruling. The
apparatus is mounted on a stage that permits motion in
the z-direction. Directly behind the grating is a lens
that projects an image of a concave surface under test
on an array of photodetectors.

To understand the operation of the interferometer,
it is helpful to consider the ordinary Ronchi test with
a stationary grating. Suppose that the motor is stopped.
Then one will observe, on the plane of the array of photo-
detectors, a conventional Ronchi test pattern. If the
surface suffers from coma, for example, then the pattern
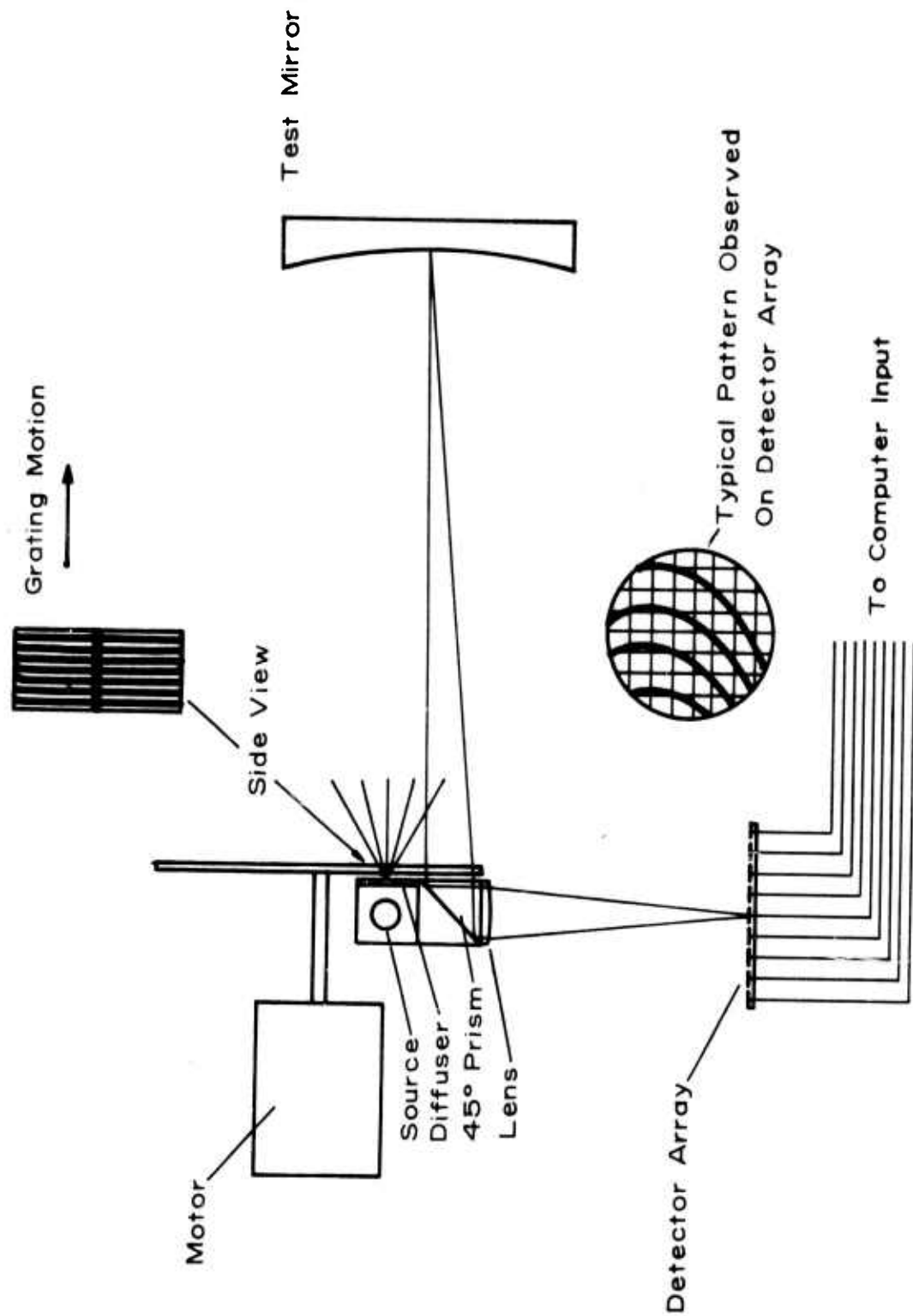
206

Figure 55. AC Grating Interferometer

may appear as shown in Figure 55. (It is supposed that

a coarse grating is used). As the motor is rotated,

the pattern will appear to move across the field (such

a small portion of the Ronchi ruling is used that the

lines appear to be straight, instead of radial, and

rotating the motor appears to translate them in the

perpendicular direction). The fringes thus move across

any point in the pattern with a frequency of about

1000 Hz, and each photodetector produces an 1000 Hz

signal.

By determining the relative phase of the 1000 Hz

signals from the various photodetectors, one can map

the fringe pattern. The accuracy with which one can do

this depends on the number of photodetectors, and the

accuracy of the phase measurement.

Although there are a number of methods for making

such a measurement, it appears that the best is to

utilize the real-time clock of a small computer to make

the measurement by interval timing. The reason for

this is that the data from the interferometer must be

processed for display purposes, and it is cheaper and

easier to use the computer for the entire process.

The computer thus receives an array of numbers which represent the phase of a sinusoidal signal at various points of the aperture. This data can then be processed in a variety of ways for presentation. For example, the pattern can be altered to eliminate the coma component, or presented as an effective (Twyman-Green) interferogram*, or the MTF computed, or the spread function, or almost anything desired.

One of the principal merits of the testing interferometer described above is its simplicity. It requires no reference optics of high quality, unlike a conventional interferometer. Such a feature is of considerable importance when testing large optics.

There are several variations of the above grating interferometer which may prove useful. One obvious variation is to locate the Ronchi ruling exactly at the center of curvature of the mirror. The test then becomes equivalent to the Foucault knife-edge test and one then has an "ac knife-edge test." Another variation is to use a point source, instead of the diffusely illuminated

- - - - - - -

*It would be necessary to take both tangential and sagittal scans for such a presentation, since the grating interferograms are effectively the derivatives of the Twyman-Green interferograms.

Ronchi ruling. It is then possible to test lenses by putting the rotating grating in the focus, in the same manner as the classical knife-edge test.

At the time of this writing, the study of different ways to use small computers in the testing lab has reached the point where we are ready to procure specific hardware and begin the experimental phase of the program. We hope to do this as soon as funding becomes available.

DOCUMENT CONTROL DATA - R&D

(Security classification of title, body of abstract and indexing annotation must be entered when the overall report is classified)

1. ORIGINATING ACTIVITY (Corporate author)	2a. REPORT SECURITY CLASSIFICATION
The Institute of Optics The University of Rochester Rochester, New York 14627	unclassified
	2b. GROUP

3. REPORT TITLE

STUDIES IN OPTICS

4. DESCRIPTIVE NOTES *(Type of report and inclusive dates)*

Technical. 13 February 1970 to 14 December 1971.

5. AUTHOR(S) *(Last name, first name, initial)*

Thompson, Brian J.; Hercher, Michael; Forsyth, James M.; Dutton, David B.;
Sinclair, Douglas C., et al

6. REPORT DATE	7a. TOTAL NO. OF PAGES	7b. NO. OF REFS
March 1972	xiv + 210 pages	62

8a. CONTRACT OR GRANT NO.	9a. ORIGINATOR'S REPORT NUMBER(S)
F 33615-70-C-1451	
b. PROJECT NO. 745	none
c.	9b. OTHER REPORT NO(S) *(Any other numbers that may be assigned this report)*
d.	AFAL-TR-71-346

10. AVAILABILITY/LIMITATION NOTICES

This document is subject to special export controls and each transmittal to
foreign governments or foreign nationals may be made only with prior approval of
the Air Force Avionics Laboratory.

11. SUPPLEMENTARY NOTES	12. SPONSORING MILITARY ACTIVITY
	Advanced Research Projects Agency, Air Force Avionics Laboratory, Air Force Systems Command, Wright-Patterson AFB, Ohio

13. ABSTRACT   The "Studies in Optics" described are directed towards the assessment and improvement of laser output characteristics and to problems in the use of the coherent output of a laser in optical systems. The various aspects of this work are clearly interrelated but for clarity are grouped into four parts, Sections II - V. Section II consists of a study of techniques for assessing and improving laser beam propagation characteristics including apodization of coherent imaging systems and holographic methods of measuring the amplitude and phase of pulsed laser beams. The design of efficient solid state lasers is addressed in Section III with particular reference to methods of enlarging the TEM_{oo} mode size and the correction of thermally induced optical distortion in repetitively pumped ruby laser rods. Section IV is a study of laser beam steering techniques leading to devices in the multi-MHz range using a new large bore argon-ion laser design with intra-cavity modulation. The final portion (Section V) is concerned with procedures for overall lens evaluation using optical transfer function data exemplified by the specific data on a 3 inch f/4.5 wide angle lens.

DD _{FORM} **1473**
1 JAN 64

14. KEY WORDS	LINK A		LINK B		LINK C	
	ROLE	WT	ROLE	WT	ROLE	WT
Apodization						
Coherence						
Holography						
Optics						
Lasers						
Lens evaluation						
Systems, optical						

INSTRUCTIONS

1. ORIGINATING ACTIVITY: Enter the name and address of the contractor, subcontractor, grantee, Department of Defense activity or other organization (corporate author) issuing the report.

2a. REPORT SECURITY CLASSIFICATION: Enter the overall security classification of the report. Indicate whether "Restricted Data" is included. Marking is to be in accordance with appropriate security regulations.

2b. GROUP: Automatic downgrading is specified in DoD Directive 5200.10 and Armed Forces Industrial Manual. Enter the group number. Also, when applicable, show that optional markings have been used for Group 3 and Group 4 as authorized.

3. REPORT TITLE: Enter the complete report title in all capital letters. Titles in all cases should be unclassified. If a meaningful title cannot be selected without classification, show title classification in all capitals in parenthesis immediately following the title.

4. DESCRIPTIVE NOTES: If appropriate, enter the type of report, e.g., interim, progress, summary, annual, or final. Give the inclusive dates when a specific reporting period is covered.

5. AUTHOR(S): Enter the name(s) of author(s) as shown on or in the report. Enter last name, first name, middle initial. If military, show rank and branch of service. The name of the principal author is an absolute minimum requirement.

6. REPORT DATE: Enter the date of the report as day, month, year; or month, year. If more than one date appears on the report, use date of publication.

7a. TOTAL NUMBER OF PAGES: The total page count should follow normal pagination procedures, i.e., enter the number of pages containing information.

7b. NUMBER OF REFERENCES: Enter the total number of references cited in the report.

8a. CONTRACT OR GRANT NUMBER: If appropriate, enter the applicable number of the contract or grant under which the report was written.

8b, 8c, & 8d. PROJECT NUMBER: Enter the appropriate military department identification, such as project number, subproject number, system numbers, task number, etc.

9a. ORIGINATOR'S REPORT NUMBER(S): Enter the official report number by which the document will be identified and controlled by the originating activity. This number must be unique to this report.

9b. OTHER REPORT NUMBER(S): If the report has been assigned any other report numbers (either by the originator or by the sponsor), also enter this number(s).

10. AVAILABILITY/LIMITATION NOTICES: Enter any limitations on further dissemination of the report, other than those

imposed by security classification, using standard statements such as:

(1) "Qualified requesters may obtain copies of this report from DDC."

(2) "Foreign announcement and dissemination of this report by DDC is not authorized."

(3) "U. S. Government agencies may obtain copies of this report directly from DDC. Other qualified DDC users shall request through

_____."

(4) "U. S. military agencies may obtain copies of this report directly from DDC. Other qualified users shall request through

_____."

(5) "All distribution of this report is controlled. Qualified DDC users shall request through

_____."

If the report has been furnished to the Office of Technical Services, Department of Commerce, for sale to the public, indicate this fact and enter the price, if known.

11. SUPPLEMENTARY NOTES: Use for additional explanatory notes.

12. SPONSORING MILITARY ACTIVITY: Enter the name of the departmental project office or laboratory sponsoring (paying for) the research and development. Include address.

13. ABSTRACT: Enter an abstract giving a brief and factual summary of the document indicative of the report, even though it may also appear elsewhere in the body of the technical report. If additional space is required, a continuation sheet shall be attached.

It is highly desirable that the abstract of classified reports be unclassified. Each paragraph of the abstract shall end with an indication of the military security classification of the information in the paragraph, represented as (TS), (S), (C), or (U).

There is no limitation on the length of the abstract. However, the suggested length is from 150 to 225 words.

14. KEY WORDS: Key words are technically meaningful terms or short phrases that characterize a report and may be used as index entries for cataloging the report. Key words must be selected so that no security classification is required. Identifiers, such as equipment model designation, trade name, military project code name, geographic location, may be used as key words but will be followed by an indication of technical context. The assignment of links, rules, and weights is optional.

GPO 886-551